Diagnostic line profiles and modelling of the accretion and outflow regions around YSOs

Raquel Maria Galhofa de Albuquerque
Mestrado em Astronomia
Departamento de Física e Astronomia
2015

Orientadores
João José de Faria Graça Afonso Lima,
Professor auxiliar, Faculdade de Ciências da Universidade do Porto

Jorge Filipe da Silva Gameiro,
Professor auxiliar, Faculdade de Ciências da Universidade do Porto

U.PORTO

FACULDADE DE CIÊNCIAS
UNIVERSIDADE DO PORTO

Todas as correções determinadas pelo júri, e só essas, foram efetuadas.

O Presidente do Júri,

Porto, 14 / 12 / 2015

Acknowledgements

First and foremost, I would like to express my sincere gratitude to my supervisors Dr. João Lima and Dr. Jorge Gameiro, whose knowledge, support and guidance enriched further my master's degree. Also, a very special thanks goes out to Dr. Véronique Cayatte and Dr. Christophe Sauty from the Astronomical Observatory of Paris, whose expertise, suggestions and patience taught me how to take my first steps in MHD numerical simulations. Without this incredible team of scientists, this thesis would not be possible.

I am grateful to Centro de Astrofísica da Universidade do Porto for providing an office and technical support, specially from Paulo Peixoto who was tireless and very helpful regarding IT disasters and software details.

I would also like to thank all my friends for our random and singular moments, which helped me in several stressful scenarios. They know who they are (:

It is my privilege to thank Mia, Teresa, Fernando and Manel for their constant encouragement and friendship, which I cherish so much.

A special word of gratitude goes to Telmo, for being who he is and for all the good moments we have shared.

Last but not the least, I am deeply thankful to my family. Specially to my beloved parents, my dearest sister and my little nephew, for all their support, advice and fondness.

Abstract

Classical T Tauri stars (CCTS) are young solar-type stars that have been known by their enigmatic angular momentum evolution. In order for a Young Stellar Object (YSO) grow-up and maintain its equilibrium simultaneously, besides accreting matter, it also needs to eject part of it in the form of outflows (stellar winds, jets, magnetospheric ejections,...). By knowing how these accretion/outflow mechanisms occur and evolve, it will possible to better understand the origins of the Solar System.

CTTS have been studied both observationally and theoretically. Spectral observations allow astronomers to characterize these stars through mass, temperature, radius, accretion/outflow velocities and accretion rates that are encoded in their emission lines. On the other hand, theoretical studies provide analytical models through magnetohydrodynamics (MHD), which is the fundamental structure to develop steady and time-dependent numerical simulations. By figuring out the relevance of some physical quantities involved, it will be possible to replicate the observations made so far.

This dissertation will focus both on observational and theoretical perspectives. Firstly, I will explore some of the spectral features present in a sample of CTTS and infer about mass accretion rates and characterize their outflow dynamics. Secondly, I will discuss the results regarding the structure modelling of magnetospheres made with numerical simulations, in collaboration with Paris Astronomical Observatory researchers.

Keywords

Accretion, CTTS, MHD, Outflows, YSO

Resumo

As estrelas T Tauri clássicas (CTTS) são estrelas jovens do tipo solar conhecidas pela enigmática evolução do seu momento angular. Para um objeto estelar jovem (YSO) crescer e manter o seu equilíbrio em simultâneo, além de acretar matéria, necessita também de ejetar uma parte sob a forma de *outflows* (ventos estelares, jatos, ejeções magnetosféricas,...). Ao saber como estes mecanismos de acreção/ejeção ocorrem e evoluem, será possível compreender melhor as origens do Sistema Solar.

As CTTS têm vindo a ser estudadas tanto observacionalmente como teoricamente. As observações espectrais permitem aos astrónomos caracterizar estas estrelas através da massa, temperatura, raio, velocidades de acreção/ejeção de matéria que estão codificadas nas suas riscas de emissão. Por outro lado, estudos teóricos fornecem modelos analíticos através da magnetohidrodinâmica (MHD), que é a estrutura fundamental para desenvolver simulações estacionárias e dependentes do tempo. Ao descobrir a relevância de algumas quantidades físicas envolvidas, será possível replicar as observações realizadas até hoje.

Esta tese será direcionada numa perspetiva observacional e teórica. Em primeiro lugar, irei explorar algumas das características espectrais presentes numa amostra de CTTS e inferir acerca de taxas de acreção e caracterizar a dinâmica de ejeção de matéria. Em segundo lugar, irei discutir os resultados relativos à modelação de magnetosferas feitas a partir de simulações numéricas, em colaboração com investigadores do Observatório Astronómico de Paris.

Palavras chave

Acreção, CTTS, MHD, Outflows, YSO

Contents

List of Figures

List of Tables

Chapter 1

Introduction

"Astronomy, as nothing else can do, teaches men humility."
— Arthur Clarke

T Tauri stars (TTS) are pre-main sequence objects of low mass ($\leq 2M_{\odot}$[1]) with ages between 1 and 10 million years, when they become optically visible. The classical T Tauri stars (CTTS) are surrounded by a circumstellar accretion disk from which they gain mass near $\sim 10^{-8}M_{\odot}/yr$ and have mass-loss rates around $10^{-9}M_{\odot}/yr$ (see figure 1.1). Also, they exhibit very strong magnetic activity, based on observations of strong X-ray emission and the detection of dark star spots covering large fractions of the stellar surface (Ferreira, 2013; Hartmann, 2009; Petrov et al., 2014).

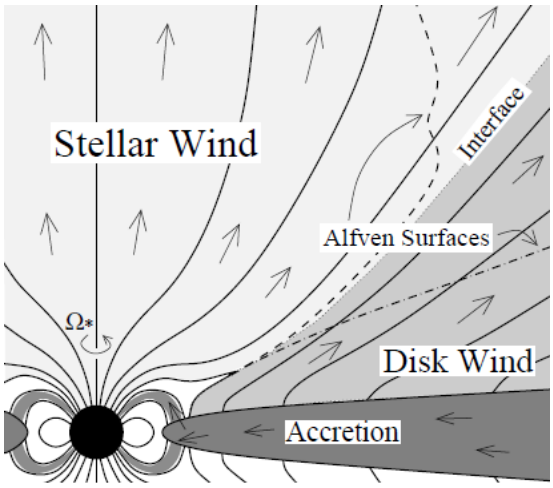

Figure 1.1: Adapted illustration of the star-disk interaction by Matt and Pudritz (2005a). The material migrates from the exterior to the inner region of the circumstellar disk and it is channelled to the polar region of the star through the accretion columns. Disk and stellar winds are outflow processes that are associated with accretion mechanisms in young active stars. The dashed and dash-dotted lines indicate the location of the Alfvén surfaces in the stellar and disk winds, respectively.

According to Bouvier et al. (2007), the intensity-weighted mean magnetic field strength over the surface of most T Tauri stars analysed is ~ 2.5 kG in the photosphere. Therefore, magnetic fields on TTS are much stronger than on the Sun ~ 500 G (Aschwanden, 2005).

[1]Solar mass, where $1M_{\odot} \sim 1.9891 \times 10^{30}kg$

Observational data shows that these young stellar objects (YSOs) are very active during the pre-main sequence stage, due to the presence of strong winds and jets which are thought to be driven by accretion mechanisms. Moreover, the most powerful winds can be observed on FU Orionis stars (FU Ori), which show episodic outbursts of several magnitudes related with dynamical instabilities. These stars are spectrally characterized by a large mass loss rate ($\dot{M} = 10^{-5} M_{\odot}/yr$), broad photospheric lines and luminosity of a supergiant. In addition, angular momentum transfers intensifies as well as accretion and outflow mechanisms (Petrov, 2003; Petrov et al., 2014).

Theoretically, we would expect that YSOs would spin up due to accretion and contraction processes, but that is not observed. Two possible angular momentum removal mechanisms can be considered according to Matt and Pudritz (2005a): winds and jets formed in magnetohydrodynamic (MHD) processes. The angular momentum of the star is regulated by the magnetic star-disk interaction, in which the large scale open magnetic field connects the rotating star-disk system with the circumstellar medium, and the magnetized outflowing gas removes the mass and angular momentum from the system.

Emission line profiles are used to study the dynamics of the circumstellar medium, namely the motion of the gas in a stellar wind or the accretion of gas to a star. Evidence of the outflow of matter (absorption shifted to shorter wavelengths, the so-called P Cygni profiles) can be found in Hα, while indications of accretion (absorption shifted to longer wavelengths, inverse P Cygni profile) are observed in the profiles of He I, for instance (Petrov, 2003). Although forbidden lines, as [OI] and [SII], do not present any P Cygni profiles, their emission is also associated with outflow processes. Emission line profiles encode not only geometrical but also physical information on the accretion/outflow processes and its rate. One of the main challenges is to use those line profiles to understand both mechanisms (Bouvier et al., 2007).

Through mass accretion rates is possible to understand disk structure and evolution, as well as planet formation and migration (Calvet et al., 2004). Furthermore, estimates of the accretion mass can already be provided through the equivalent width and the width measured at 10% peak intensity of the Hα line (Natta et al., 2004), Paschen and Brackett lines (near-infrared) and veiling. For the latest, in CTTS the lines of the photospheric spectra are less deep than in normal stars of the same spectral type and the absorption spectrum appears weak and veiled. This veiling is caused mainly by additional continuum emission of nonphotospheric origin, which increases toward shorter wavelengths (Petrov, 2003).

At the moment, there is no model capable of simulate alone all the physical mechanisms involved in YSOs, due to its complexity and interactivity. Nevertheless, models may be built and constrained according to observations in a first approach.

Sauty and Tsinganos (1994) developed a semi-analytical MHD model to simulate outflow mechanisms observed among YSOs. The mentioned model uses the meridional self-similar approach, which simplifies the set of partial MHD differential equations into nonlinear ordinary ones, through variable separation and function scaling with one of the spatial coordinates, the colatitude θ (Sauty et al., 1998). The latest model was adapted in collaboration with researchers from Paris Astronomical Observatory, by including

magnetospheric accretion processes, which are thought to feed outflow mechanisms. The results obtained throughout the numerical simulations made with PLUTO code will be explored and discussed.

Regarding the thesis structure, in chapter 2 is given a short review regarding T Tauri stars general features, folllowed by section 3 where accretion and outflow mechanisms are described as well as angular momentum extraction processes known. Chapter 4 and 5 show the results regarding observations and simulations, respectively, and chapter 6 makes the linkage between these two last perspectives. Finally, conclusions are drawn in chapter 7.

Chapter 2

T Tauri Stars

2.1 UNVEILING T TAURI STARS

The best approach we have, in order to understand the evolution of the solar system, is to study young solar-like forming stars. These low mass, pre-main sequence (PMS) stars can be found in stellar nurseries, are named T Tauri stars (TTS) and are classified as class II objects.

TTS were named after the discovery of the first star with the same characteristics: T Tauri. The star was discovered in October of 1852 by an asteroid hunter, John Russel Hind, who was scanning the night sky and found out that this star was missing from the charts of stars with magnitude 10. Due to its photometric variability, it was not observed and catalogued earlier[1].

The infrared (IR) excess observed in young stellar objects can be seen as a measure of stellar youth and can be quantified through the infrared spectral index given by

$$\alpha_{\mathrm{IR}} \equiv \frac{d\log(\lambda F_\lambda)}{d\log(\lambda)}, \tag{2.1}$$

where λ is the wavelength and λF_λ is the flux measured per logarithmic wavelength interval, typically between 2.2 and $10\ \mu m$. According to different α_{IR} values, pre-main sequence stars are classified with different classes (Lada and Wilking, 1984; Adams et al., 1987; Stahler and Palla, 2005):

- Class 0: sources deeply buried only detected at far-infrared and millimeter wavelengths;
- Class I: $\alpha_{\mathrm{IR}} > 0$, these objects are associated with dense cores;
- Class II: $-1.5 < \alpha_{\mathrm{IR}} < 0$, are less embedded stars, namely classical T Tauri stars (CTTS);
- Class III: $\alpha_{\mathrm{IR}} < -1.5$, correspond to brighter stars which circumstellar disk has been dispersed and the accretion processes, when observed, are very weak (weak line T Tauri stars - WTTS).

[1] American Association of Variable Star Observers: http://www.aavso.org/vsots_ttau

Regarding variability, T Tauri stars were first identified by Joy (1942) as a group with variable brightness (also know as irregular variables). Ambartsumian (1947) found that TTS occur in groups named T-associations, which have a connection with O-associations (groups of OB stars). He suggested that TTS were the low-mass counterpart of recently formed OB stars. Later, TTS were subdivided in two groups: CTTS still accreting from their circumstellar disks and WTTS without a disk (do not show NIR excess) and with weak Hα emission lines (Herbig, 1962; Herbig and Bell, 1988; Hartmann, 2009). While CTTS seem to be more irregular, WTTS show periodic photometric variations. The weakly variability among CTTS has three possible causes according with Grankin et al. (2007): cold surface spots (resulting from strong magnetic fields), hot surface spots (associated with disk accretion onto the star) and variable obscuration of the star by the circumstellar disk.

Thanks to Ambartsumian (1947), TTS can be seen as a proof that star formation processes still continue in our Galaxy. These stellar objects have their origin in gravitational collapses on molecular clouds. Once hydrostatic equilibrium is reached, accretion mechanisms are still active and the star is wrapped by an opaque cloud, which optically hides the protostar. The star becames visible in the optical when the protostar reaches the T Tauri stage. Here, besides accretion, outflow mechanisms are also observed and are thought to be responsible for slowing down the rotation velocity of these objects. In addition, before the star reaches the main sequence through the Hayashi track, gravitational energy is the main source of energy. In this descending "path", the star is mainly convective and keeps approximately its temperature, while the luminosity decreases. Afterwards, a radiative core begins to form and this time luminosity is kept constant while temperature rises until is sufficient to the helium ignition, starting nuclear reactions and marking the entry in the main sequence. The remains of the accretion disk will be accreted into planetesimals and afterwards a whole new set of orbiting planets is formed. Figure 2.1 shows the distribution of T Tauri stars in the Hertzprung-Russel diagram. It is possible to observe that these stars are located at the right of the main sequence in the regions of convective and radiative tracks (Petrov, 2003).

In the 1990's, observations in the IR accused not only the presence of circumstellar disks around T Tauri stars but also that they are interacting with the central star through accretion mechanisms. The IR luminosity of the disk is caused both by re-radiation of light from the central star and by its own radiation (Lynden-Bell and Pringle, 1974; Petrov, 2003).

While CTTS have a typical rotation period of 6-9 days, WTTS show a value between 2-5 days (Bouvier et al., 1995). CTTS rotate more slowly than WTTS due to the magnetic interaction between the accretion disk and the central star. When the disk begins to dissipate (star goes from CTTS phase to WTTS), the star begins to speed up and dynamo processes can be expected to become even stronger. In other words, WTTS represent the intermediate stage between the accretion phase and the zero-age main sequence (ZAMS). In addition, all the high energy mechanisms involved affect the remaining of the circumstellar disk material (protoplanets and planetesimals included) and may be relevant to understand observable

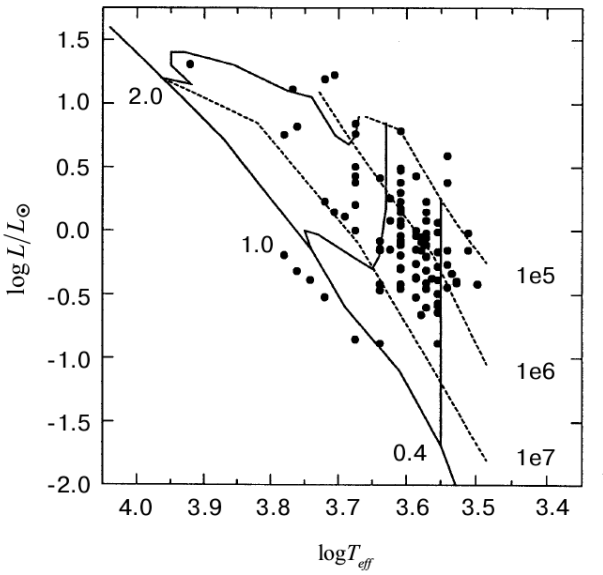

Figure 2.1: Position of T Tauri stars on an Hertzprung-Russel diagram by Petrov (2003). Are represented evolution tracks for stars with $0.4M_\odot$, $1.0M_\odot$ and $2.0M_\odot$ (solid lines) along with three isochrones for ages 10^5, 10^6 and 10^7 years (dashed lines).

properties of asteroids in the solar system (Audard et al., 2005).

2.2 SPECTRAL FEATURES IN CTTS AND WTTS

Accretion and outflow mechanisms govern many spectral features among young stars and are fundamental in the star formation process (Hartigan et al., 2004). Classical T Tauri stars are more active than weak line. While CTTS present accretion disks responsible for the spectra excess in the UV and IR, pronounced stellar winds and rich emission-line spectrum (Hα, H and Ca II, for example); WTTS do not have accretion disks and only magnetic activity occurs (see figure 2.2).

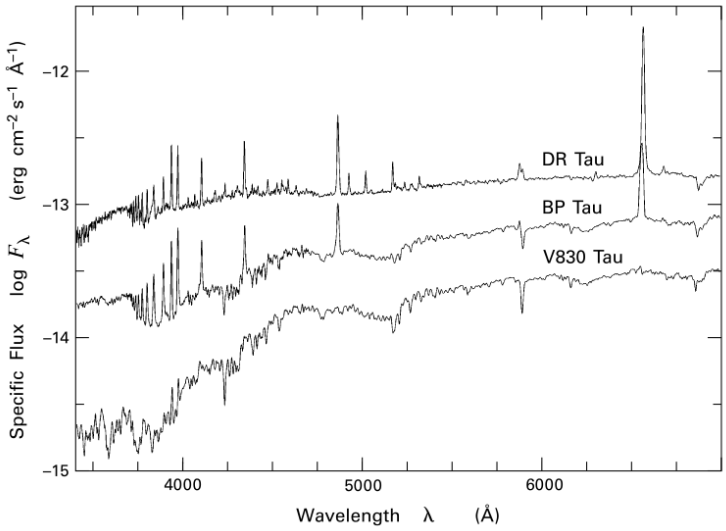

Figure 2.2: Medium-resolution spectra of three T Tauri stars. The received flux is correct only for BP Tau while the remaining spectra were shifted vertically. V830 Tau is a weak line T Tauri star, while BP Tau and DR Tau are classical T Tauri stars. For the most active stars, DR Tau and BP Tau, it is possible to observe some relevant emission lines as Hβ and Hα, at 4861Å and 6563Å respectively (Stahler and Palla, 2005).

TTS are dwarf stars with deep convective zones and their photospheric spectra ranges from late F to M, but their typical spectrum is K7 V (Herbig, 1962; Cohen and Kuhi, 1979). Usually, TTS show a great number of photospheric absorption lines, but they vary according to spectral type and can be diluted by veiling (Reipurth et al., 1996).

What distinguishes TTS from main sequence stars is the ultra-violet and optical continuum excess emission, also known as *veiling*. The intensity of this spectral feature increases towards shorter wavelengths, suggesting its origin from a hot region with gas at 10^4K. When looking to CTTS spectra, the photospheric lines appear to be less deep and weak (therefore, veiled). This excess manifests also in the Balmer jump emission at 3646Å. According to Herczeg and Hillenbrand (2008), the size of the Balmer jump tends to increase with both decreasing stellar mass and accretion rate. Veiling is usually attributed to the presence of an additional continuum emission of nonphotospheric origin. It has been discussed that the observed hot continuum emission could arise from the dissipation of accretion energy of hot spots, where magnetospheric gas shocks rapidly onto the stellar surface. Hence, measurements of this excess can provide estimates for mass accretion rates (Muzerolle et al., 1998b; Stahler and Palla, 2005; Petrov, 2003; Petrov et al., 2014; White and Basri, 2003).

Veiling (r) is also one way to measure stellar youth and its given by

$$r_\lambda = F^\lambda_{\text{veil}}/F^\lambda_{\text{phot}}, \tag{2.2}$$

where F^λ_{veil} is the flux of the veiling continuum (given by $F^\lambda_* - F^\lambda_{\text{phot}}$, where F^λ_* is the measured flux of the star) and F^λ_{phot} is the flux of the undisturbed photosphere (Muzerolle et al., 1998b). Hartigan et al. (1995) showed that the heavily veiled CTTS are on average younger than the remaining stars in the sample studied.

Analysing figure 2.2, is possible to observe that V830 Tau (WTTS) is less veiled than BP Tau and DR Tau (both CTTS), which show shallower lines and less absorption dips. Heavily veiled stars have their spectra dominated by emission produced by accretion, with rare photospheric component and dense emission lines at higher wavelengths (Herczeg and Hillenbrand, 2014).

When looking to a TTS emission spectrum, it is quite similar to the chromosphere of the Sun (Joy, 1945). In the optical band it is possible to detect pronounced emission lines for Hα. In the near IR band, the most intense lines are from the Ca II triplet (8498, 8542 and 8662 Å). In the IR, it is possible to observe Paschen and Brackett series lines. Regarding features in the mid-IR and far-IR bands, those belong to the stellar wind and circumstellar dusty disk. In addition to this set of features, CTTS have also Balmer series lines and lines of neutral and singly ionized metals (Petrov, 2003).

Emission line profiles are key factors regarding the study of circumstellar dynamics, namely gas motion in stellar winds and accretion mechanisms. For instance, when matter is being ejected from a star by jets or winds (outflows), the Hα absorption line is shifted to shorter wavelengths and acquires the so-called P Cygni profile. When matter is being accreted, absorptions are shifted to longer wavelengths, jointly with the formation of inverse P Cygni profiles, among the higher members of Balmer series, He I and Fe II (Stahler and Palla, 2005; Petrov, 2003).

It is worth to mention that intense stellar winds and accretion are only observed in CTTS. Also, forbidden emission lines of [OI] and [SII] are mainly observed in these type of pre-main sequence stars. Although these lines have lower intensities than allowed ones, their emission comes from rarefied gas flows (i.e. jets/winds) at distances higher than 1 AU from the star. When studying forbidden lines, among the majority of TTS is possible to observe double profiles. There is a central emission peak at the radial velocity of the star, that can be slightly shifted to the blue, and an emission peak between -50 to -150 km/s with origin in a stellar wind and/or in a jet (Petrov, 2003).

2.3 MAGNETIC FIELDS IN TTS

T Tauri stars show evidence of strong magnetic activity, due to the presence of X-ray emission (Feigelson et al., 2007), which is higher three orders of magnitude than the solar corona, the presence of large starspots (Herbst and Shevchenko, 1999) and indirect measurements of large photospheric magnetic fields (Johns-

Krull et al., 1999). Magnetic field intensities in these stars can reach values between 1-2 kG, which is sufficient to channel accretion flows (Hartmann, 2009; Petrov et al., 1976).

X-ray emission has been observed both in WTTS and CTTS and depends on the rotation velocity of the stars. Among CTTS, X-ray emission is related to accretion mechanisms, while in WTTS is associated with magnetic activity due to a dynamo mechanism as in main-sequence magnetically active stars (Audard et al., 2005).

Concerning stellar spots, cold spots can be observed in WTTS and CTTS and have areas between $5-10\%$ of the stellar surface and temperatures within the range $200-1200$ K (lower than the photosphere). In contrast, hot spots are only observed in CTTS, cover only $1-2\%$ of the stellar surface, have temperatures between $7000-10000$ K and exist no more than a few revolutions of the star (Herbst et al., 1994; Petrov, 2003). Photometric studies suggest they are the source of additional radiation responsible for the veiling of the photospheric spectrum. Due to the fact that these spots are only observed in CTTS, which have circumstellar disks from which they gain mass, these features may be caused by the gas accretion on the surface of the star (Bouvier and Bertout, 1989). Herbst et al. (1994) confirmed this idea with a correlation between the amplitude of the variability in brightness and the amount of veiling.

Chapter 3

Star-disk interaction

From the accretion neutron star model of Ghosh and Lamb (1979), Uchida and Shibata (1985) and Koenigl (1991) adapted it to explain the low rotation periods observed among active TTS. One of the main ideas in the star-disk interaction is that, in order for T Tauri stars truncate their disk at a radius bigger than the stellar radius (between 3 and $7R_*$), they must have strong dipolar fields (between 1 and 3 kG) and maintain the connection between the accretion disk and the star. In other words, the disk is truncated where the magnetic field pressure balances the ram pressure of the accreting material. In addition, this magnetized interaction would have a fundamental impact regarding the transfer of angular momentum back to the disk. Also, the infalling of material from the disk onto the stellar surface guided by magnetospheric fieldlines (with associated mass accretion rates between 10^{-9} and $10^{-7}M_{\odot}/yr$), could explain the UV excesses found in observations (Bouvier et al., 2007; Ferreira, 2013).

This star-disk interaction results in a balance between accretion and outflow mechanisms. According to Hartigan et al. (1995), the ratio between mass loss and accretion is approximately 1%. More specifically, Cabrit (2007) infer that typical ratios of jet mass flux to accretion rate for low-mass CTTS are near 10%. In both cases, this means that accretion processes are the dominant effect.

3.1 ACCRETION

The evolution of circumstellar disks has become increasingly important since the boom discovery of exoplanets and respective planetary systems. By studying accretion and outflow mechanisms in these set of young accreting stars, in the future it will be possible to derive more clues regarding the evolution of stars and planet formation scenarios (Bouvier et al., 2007).

In agreement with Kepler's laws, the accretion disk material rotates differentially. Due to the fact that rotation energy is converted to thermal energy by the viscosity, the temperature of the disk increases and radiation is emitted. Meanwhile, matter descends to lower orbits, as it loses energy, until being accreted.

Disks usually last for $\sim 2-5$Myr, have sizes about 100 AU and the temperature at 10 AU is around 100 K. They can also be classified as active or passive. Active refers to self luminous accretion disks, while passive refers to disks that re-radiates absorbed starlight in the IR. This distinction can be made through luminosity. When considering passive disks, the observed bolometric luminosity for the star-disk system should be the same as for a star of the same spectral type. In the case of active disks, the luminosity of the disk may be higher than the star (Herczeg and Hillenbrand, 2014; Petrov, 2003).

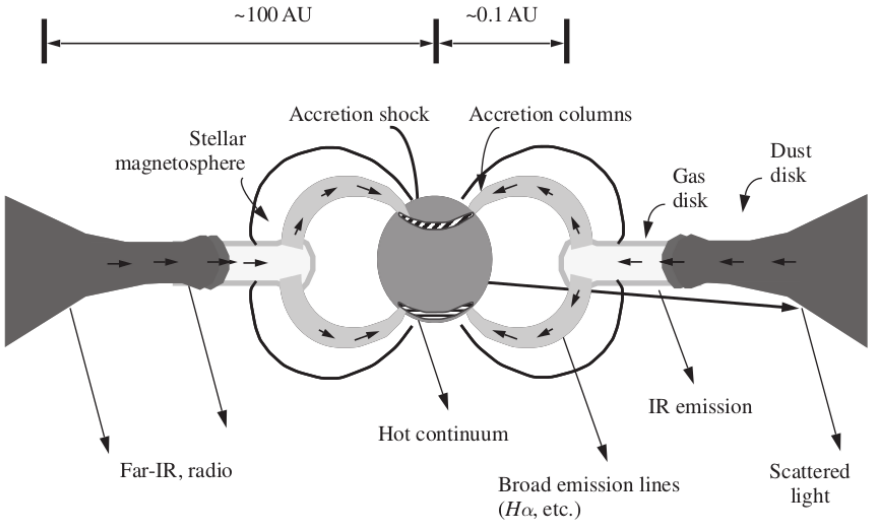

Figure 3.1: Illustration of the accretion phenomenon in T Tauri stars (not to scale) by Stahler and Palla (2005).

In figure 3.1 the magnetospheric accretion mechanism is illustrated. The stellar object is surrounded by an accreting circumstellar disk which emits at several wave bands, namely: infrared, sub-mm and mm. In the inner disk, the stellar magnetic field lead to its disruption by transferring disk material onto the star. This magnetospheric material emits broad emission lines (namely Hα line) along the infalling accretion columns, producing a hot continuum when crashing onto the stellar surface originating the so-called hot spots (represented in figure 3.2). The truncation radius is located inside the radius at which dust is sublimated by radiation from the central star and accretion shock (Stahler and Palla, 2005).

Mass accretion rates can be seen as a disk evolution indicator since it usually decreases with time as mass is accreted onto the star (Hartmann, 2009). According to Calvet et al. (2004), the best determinations of accretion rates for young stars are provided by veiling measurements.

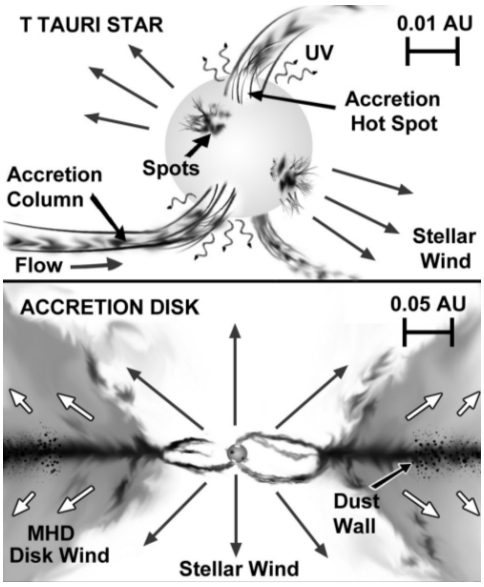

Figure 3.2: Schematic view of accretion/outflow mechanisms in CTTS by Frank et al. (2014).

3.2 OUTFLOWS

Outflows are the reverse process of accretion and can be easily observed in stellar or galactic objects (Petrov, 2003; Tsinganos, 2007). They can be shaped in uncollimated winds and collimated jets, with bipolar flows oriented in two opposite directions and perpendicular to the plane of the disk. When flows are driven by more narrow and compact bipolar streams, they are designated jets and can be supported by Hα, [NII], [OI] and [SII] emission lines (Petrov, 2003).

Besides jets, stellar winds are also an outflow phenomenon (see figure 3.3) with mass flux rates near $10^{-9} M_{\odot}/yr$. This mechanism can be detected in TTS spectra through blueshifted absorptions among Hα and Ca II (for example), in which velocities range from 100 to $400\ km/s$.

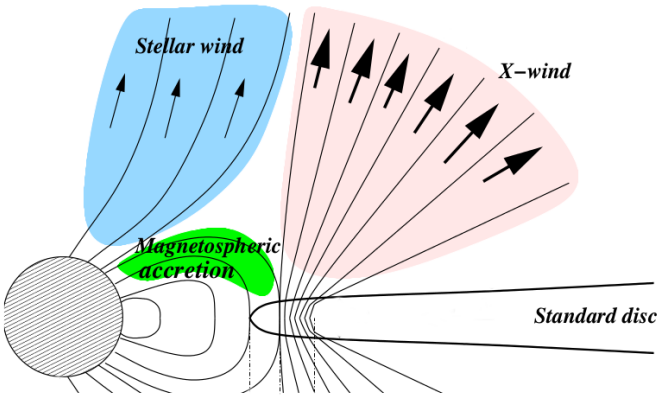

Figure 3.3: Representation of stellar winds (blue), X-winds (pink) and magnetospheric accretion (green) processes location in a YSO. Figure adapted from Ferreira (2013).

Another configuration for outflows is based on the conical wind model proposed by Romanova et al. (2009), were mass is transferred from the inner disk and accelerated by magnetic pressure.

When studying outflow regions, forbidden line profiles provide useful informations regarding its composi-

tion, namely the existence of two velocity components: a fast ($> 100\ km/s$) and a slow one ($< 50\ km/s$). The first case refers to a narrowly directed jet, while the second one is supposed to be related with an outflow of matter from the surface of an accretion disk (Hartigan et al., 1995; Kwan and Tademaru, 1988; Petrov, 2003).

According to Sauty et al. (1998), some of the most intriguing questions concerning outflows are the acceleration mechanisms and their various morphologies. For the latest, it has been suggested that winds and jets expand conically and cylindrically, respectively (see figure 3.4).

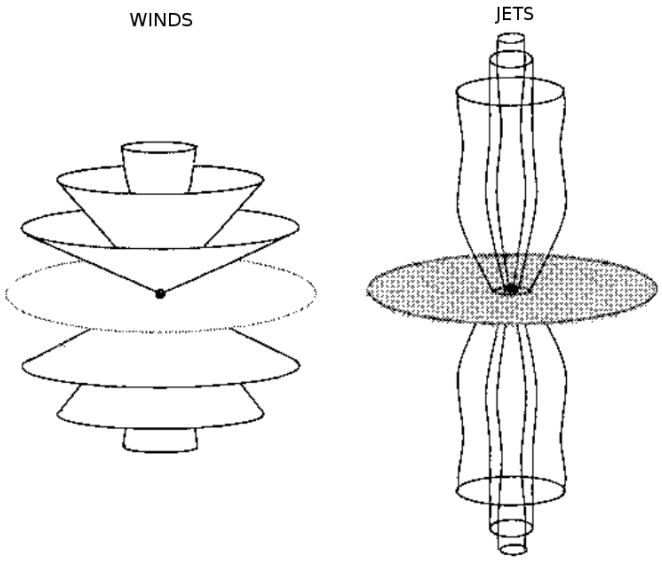

Figure 3.4: Illustration of winds (left) and jets (right) morphologies by Sauty et al. (1998).

Stellar winds

Since the 1980's that stellar winds, similar with the solar case, have been pointed out for their importance regarding angular momentum extraction among young accreting stars (Shu et al., 1988; Hartmann and Stauffer, 1989). The accretion rate is proportional to the amount of angular momentum carried onto the star by the disk. Therefore, stellar winds could be a key factor to slow down the rotation period of the star due to accretion when the outflow rate is approximately 10% of the accretion rate, as expected theoretically by some authors (Hartmann and Stauffer, 1989; Matt and Pudritz, 2005a). Additionally, Cabrit et al. (1990) concluded that stellar winds in TTS are correlated with accretion, due to Hα and IR luminosities, respectively.

According to Matt and Pudritz (2005a), part of the gravitational potential energy released during accretion could be powering stellar winds and boosting mass outflow rates. In addition, the associated torque increases not only with magnetic field strength, but also with the mass loss rate. Furthermore, the authors introduced the Accretion Powered Stellar Winds paradigm (APSW). In the latest, the stellar dipolar field truncates the disk at R_t, imposing the matter to accrete onto the star, through the magnetospheric fieldlines, leading to shock formation near the polar stellar surface, emission of UV radiation as well as

compressive waves in the star photosphere. The turbulent process would be able to convert part of the resultant thermal and kinetic energy to MHD turbulence which could supply kinetic energy to stellar winds formation.

Because the latest model establishes a direct relation between accretion and ejection, Zanni and Ferreira (2011) thought that accretion shock luminosity L_{UV} could be used to constrain the wind characteristics and give upper limits to the spin-down efficiency. The authors found out that luminous sources with $L_{\mathrm{UV}} \geq 0.1 L_{\odot}$ and typical dipolar field components lower than 1 kG do not allow spin equilibrium solutions. In addition, lower luminosity stars ($L_{\mathrm{UV}} < 0.1 L_{\odot}$) are compatible with a zero-torque condition, which contrasts with the high necessity of mass and energy for stellar winds. For such matter, its argued that the APSW is not efficient to explain the spin-down observed among CTTS.

Gregory et al. (2012) and Zanni and Ferreira (2013) have shown that the stellar magnetic field is not sufficient to produce relevant stellar winds. An efficient spin-down torque requires a rather strong dipolar component, which is rarely seen among classical T Tauri stars. The authors suggest that non-axisymmetric and multipolar magnetic components should be considered when studying torques acting on the protostar and they must be consistent with observations.

An important aspect to take into account is that there must be an upper limit for the ratio between the mass loss rate and mass accretion rate, otherwise there will not be sufficient energy to drive stellar winds. Matt and Pudritz (2008) suggested that the ratio should be approximately $\dot{M}_{\mathrm{wind}}/\dot{M}_{\mathrm{acc}} \leqslant 60\%$.

Despite all the progress made so far, how accretion power may transfer to a stellar winds still needs further investigation.

X-winds and disk winds

The purpose of the X-wind model theorized by Shu et al. (1994) was to explain YSO jets as well as the spin-down of the protostar. According to the authors, X-winds have their origin in the inner region of the disk and should be the dominant factor in YSO jets (concerning mass flux, appearance and power) responsible for angular-momentum extraction, such that the star is not spun up by accreting material (Ferreira, 2013).

In order to explain the slow rotation periods of accreting T Tauri stars, the X-wind model takes into account the interaction between the stellar disk and the stellar magnetosphere. Figure 3.5 illustrates the X-wind model for the steady-case scenario. Initially, the stellar magnetic flux that threads the entire disk is captured in the X-region, which is a narrow annulus located at the disk inner edge. In the latest region the magnetic pressure prevails over gas pressure, such that the annulus rotate as a solid body. In addition, it contains the corotation radius R_X ($3-5R_*$ for TTS, e.g. Hartmann (2009)), where the stellar angular velocity is equal to the Keplerian angular velocity: $\Omega_* = \Omega_X = \sqrt{GM_*/R_X^3}$. This implies that disk material near the interior radius R_X rotates at sub-Keplerian velocities, which enables the disk material to flow through the fieldlines (bended inwards) onto the star. On the other hand, disk material near the

exterior radius R_X will rotate at super-Keplerian velocities, such that it will ascend along the fieldlines (bended outwards) and escape in a wind.

Regarding angular velocity, Artemenko et al. (2012) discovered that it remains constant when considering CTTS with 0.3 to $3M_{\odot}$ and ages between 1 and 10 Myr, suggesting the existence of an efficient angular momentum regulation mechanism. Moreover, completely convective (less massive) CTTS rotate slower than CTTS on radiative evolutionary tracks (more massive) and the majority of CTTS have periods no longer than 10 days.

There is an excess of angular momentum transferred from accretion to the disk material in the inner portion of the X-region, which will tend to push the material outwards. In contrast, induced disk winds (launched from the extended disk region) in the outer portion of the X-region will transfer angular momentum to outflowing gas at the expense of the disk material connected by fieldlines with origin in the exterior of the X-region, pushing this material inwards. This outward and inward push on the inside and outside region of the X-region will conduct to the so called *trapped flux* phenomenon and to the disk truncation at the inner edge. Taking all into account, the angular momentum transfer from accretion funnels to the wind lead to a slow rotation of the star (Bouvier et al., 2014; Ostriker and Shu, 1995).

Another interesting feature in figure 3.5 is the helmet streamer structure, which is formed through the interface between open field lines loaded with outflowing matter (connected to the disk) and those not loaded (connected to the star). Along these features, major mass ejection and reconnection events may arise in response to changes in the boundary conditions (Ostriker and Shu, 1995).

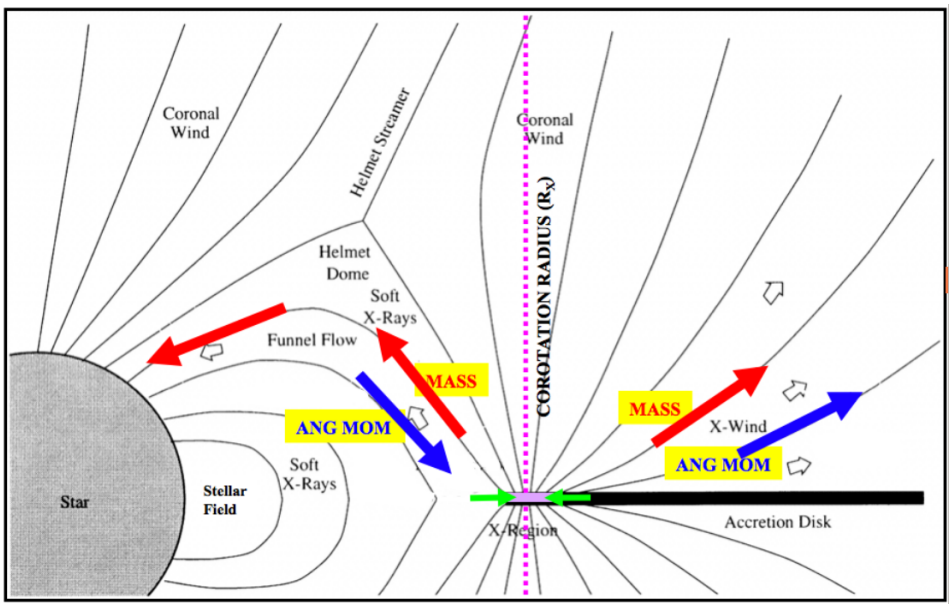

Figure 3.5: Representation of steady-state X-wind model by Bouvier et al. (2014). The black thick line represents the truncated disk and the black solid curves the magnetic fieldlines. The purple dotted line shows the co-rotation radius R_X and the purple thick line represents the X-region. Red and blue arrows show the direction of mass and angular momentum transport, respectively. Green arrows refer to the pinching of gas is the X-region due to angular momentum transport.

Magnetospheric ejections

Magnetospheric ejections (MEs) can exchange mass, energy and angular momentum with the star and the disk. This exchange begins with an expansion followed by reconnection of the closed magnetospheric lines connecting the star to the disk. The inflation process develops through the star-disk differential rotation and resultant build-up of toroidal magnetic field pressure (Zanni and Ferreira, 2013). According to the authors, the angular momentum exchange with the star is mainly controlled by the differential rotation between the star and the MEs. If at the cusp of the fieldline the mass loaded from the disk rotates more slowly (faster) than the star, the MEs exert a spin-down (spin-up) torque.

At more distant regions from the star, MEs disconnect from the central region of the disk-star region in a magnetic reconnection event and propagate ballistically as magnetized plasmoids (much alike coronal mass ejections in the Sun) in a channel delimited by two quasi-steady MHD flows: the inner stellar wind and an outer disk wind (see figure 3.10). Due to magnetic reconnection, the inner magnetic surfaces close again (see figure 3.6) and this *magnetic slingshot* mechanism repeats along the time in a quasi periodically way (Bouvier et al., 2014; Ferreira, 2013; Zanni and Ferreira, 2013).

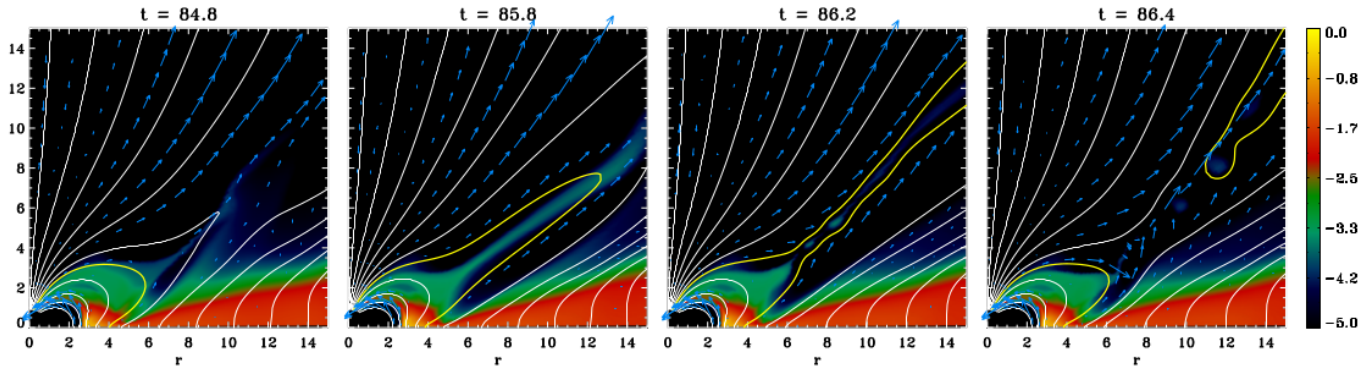

Figure 3.6: Temporal evolution of the periodic inflation/reconnection process of magnetospheric ejections powered by stellar and disk rotation. Blue arrows represent the poloidal velocity vectors and the white lines the magnetic fieldlines. Are also represented logarithmic density maps with and the yellow solid lines follow the evolution of a single magnetic surface showing the dynamics of the phenomenon. Time is given in units of rotation periods of the central star (Zanni and Ferreira, 2013).

Zanni and Ferreira (2013) concluded that MEs are partly responsible for controlling the rotation period of a star. They are able to efficiently extract angular momentum from the disk close to the truncation region such that the spin-up accretion torque is considerably reduced. Furthermore, and due to differential rotation, MEs can extract directly angular momentum from the star if the ejected plasma rotates slower than the star. Furthermore, the authors discovered that the combined effect of MEs and stellar wind lead to the spin-down torque on the star. For such matter, MEs could be one of the best mechanism to explain the disk-locking phenomenon observed in CTTS.

Jets

Although the precise origin of jets from YSOs is still being discussed, is accepted that the ignition process involves the interactive dynamics of accreted matter with stellar and/or disk magnetic field (Frank et al.,

2014). However, it is not defined if jets have their origin from the stellar surface (Sauty and Tsinganos, 1994), the magnetosphere/disk interface (Shu et al., 1995) or a wide range in disk radii (Ferreira, 1997).

In figure 3.7 are shown small jets detected in a CTTS. This kind of images provides the opportunity to test current ejection theories, because they not only give access to the interior wind regions (≤ 100AU) but also give information concerning stellar and accretion properties. Besides images to study non-relativistic jets in YSOs, position-velocity diagrams, emission lines, mass accretion rates are also useful tools (Ferreira, 2013).

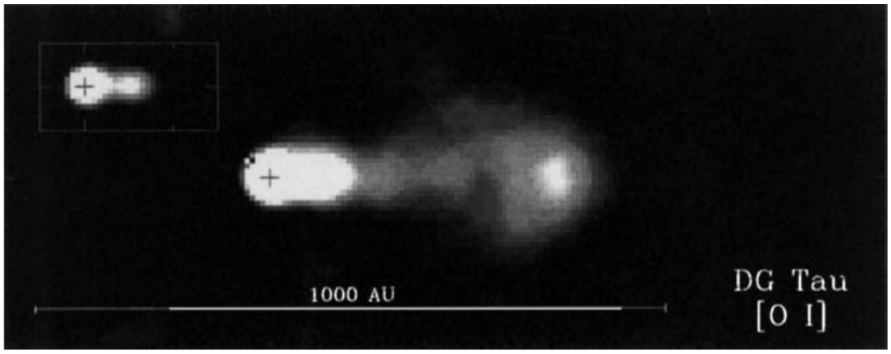

Figure 3.7: Deconvolved [OI] 6300Å plus the narrow-band image of DG Tau microjet through adaptive optics (Dougados et al., 2004)

Jets are highly collimated structures (opening angle of a few degrees) composed by bright separate nodes caused by pulsed acceleration of the jet of a young star. In addition, a bright arc (*bow shock*) may form where the collimated flow collides with the interstellar medium, as illustrated in figure 3.8 (Petrov, 2003). Moreover, jets can carry between 5×10^{-10} and $2 \times 10^{-8} M_{\odot}/yr$, which according to Schwartz (1983) and Mundt (1988), is suggest that only a small fraction of the stellar wind is collimated into jets. More specifically for CTTS, typical outflow rates vary between 10^{-9} and $10^{-7} M_{\odot}/yr$ (Frank et al., 2014).

When observing jets in the optical wavelength, its only possible to trace one side of the jet outflow (towards the observer in the blueshifted side), while the other one is traced in the NIR emission in molecular hydrogen and radio observations, which are unaffected by extinction (Hartmann, 2009). Hence, observations proved that YSO jets are bipolar, but interestingly, despite of ejecting the same amount of mass at each jet, terminal velocities may differ by up to a factor of 2 (Podio et al., 2011; Melnikov et al., 2009).

The observed jets among CTTS have regions of forbidden line emissions with sizes between 100 and 500 AU and carry velocities near $170\ km/s$ (Hirth et al., 1996). Interestingly, around half of the observed pair of opposite jets seem to present different velocities. This means that jets are not being equally accelerated (Hirth et al., 1994b; Woitas et al., 2002). To support these ideas, observations have shown that jets may suffer strong disturbances due to shocks and possibly unsteady ejections events from the star (Ferreira, 2013). Moreover, and according to Frank et al. (2014), a jet may be seen as a string of shocks with a wide range conditions.

Jets within 100 AU have lower shock speeds and are designated as microjets, according to Dougados

et al. (2000). Because jets are essentially a time-dependent phenomenon evidenced by their knotty morphology, steady-state models are a good starting point to study them under a theoretical perspective. There are already three main model types for YSO jets: stellar winds (Sauty et al., 2004; Matt and Pudritz, 2005a), X-winds (Shu et al., 1994; Cai et al., 2008) and magnetized winds (Blandford and Payne, 1982; Ferreira and Pelletier, 1993; Ferreira and Casse, 2004). Although they are based on different boundary conditions, they all share the same MHD equations and existence of a strong magnetic field in a rotating object (Ferreira, 2013).

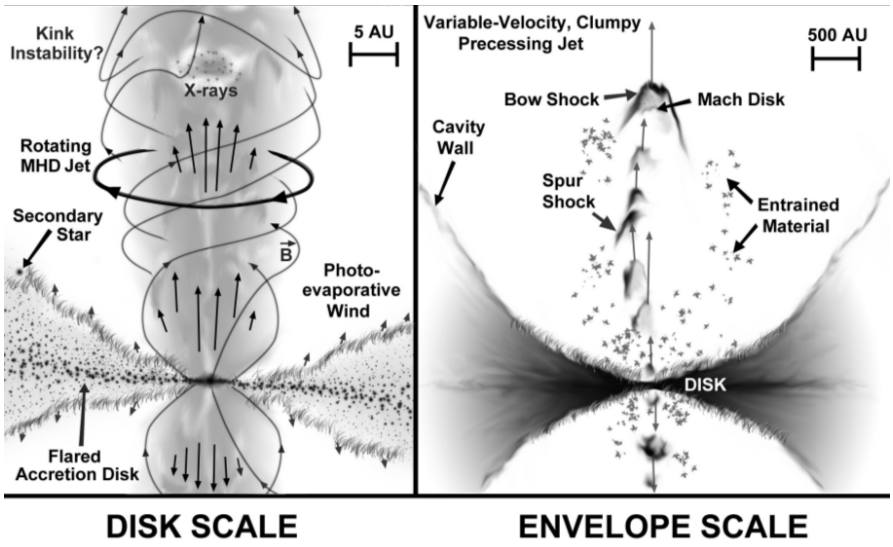

Figure 3.8: Illustration of jet features in T Tauri stars in two different scales by Frank et al. (2014).

3.3 ANGULAR MOMENTUM EXTRACTION

As mass, temperature and metallicity, the angular momentum of a PMS star is one of the most fundamental physical quantities, which characterizes the rotation and translation of a body: $\vec{L} = \vec{r} \times \vec{p} = \vec{r} \times m\vec{v}$. The rotation of a star influences not only its internal structure, energy transport, mixing processes in the stellar interior, but also its magnetic activity (Bouvier et al., 2014).

By studying the evolution of the angular momentum along the lifetime of the stars, questions concerning star formation processes, accretion/outflow mechanisms in YSOs, future of stellar activity and its impact on planetary formation could be answered (Bouvier et al., 2014).

One of the big questions is why are YSOs showing values for their rotation velocity lower than the ones expected theoretically. Looking to the solar case and according to Priest (1984), the velocity of the solar-wind plasma is inclined about $1.5°$ relatively to the radius vector. This is going to translate in a deceleration effect in the rotation of the Sun, due to the fact that angular momentum is being transferred from the Sun to the solar wind. In a similar way, this process will also occur in PMS stars but in a more pronounced level due to stronger magnetic fields and pronounced accretion/outflow mechanisms.

Stars with disks are slower rotators when compared with diskless ones. While the former ones have

rotation periods between 3 to 10 days, the later ones show periods between 1 and 7 days, which can be photometrically derived from monitoring surface spots (Bouvier et al., 2014).

In addition, it seems to exist a trend between stellar mass and rotation periods. According to Herbst et al. (2001) and Cody and Hillenbrand (2010), observational data suggests that rotational braking becomes gradually less efficient towards stars with lower masses ($M_* < 1M_\odot$).

Gallet and Bouvier (2013) suggest that the evolution of spin rates of solar-mass stars requires substantial angular momentum loss at nearly all stages of evolution and the required amount of torque is higher in the young forming ages. And the largest torques could be explained by the fact that a substantial fraction of stars with ages below 5 Myr are still accreting through a star-disk interaction (Koenigl, 1991). Therefore, the dissipation of the disk (which corresponds to the cessation of accretion processes) could explain the transition to weaker torques. Zanni and Ferreira (2013) concluded that, depending on the accretion rate, magnetospheric ejections can extract a relevant amount of accretion torque and, together with a weak but non-negligible stellar wind torque, can balance the spin-up due to accretion.

The *disk-locking* process, initially proposed by Ghosh and Lamb (1979), has been verified by observations and suggests that stars, during the first million years in the PMS, are interacting with their disks through the magnetic field. The model is confirmed by the inverse relationship between the angular velocity of the star and the near-infrared excess, suggesting the presence of a circumstellar disk (Artemenko et al., 2012).

According to figure 3.9, only if outer radius R_{out} (the outermost radial extent of the magnetic connection) is bigger than co-rotation radius R_{co} (where the Keplerian angular velocity is equal to the stellar angular velocity), magnetic braking and accretion will occur. As mentioned previously for X-winds, fieldlines connecting the disk outside the co-rotation radius will have a spin-down effect, while the fieldlines coupled to the disk inside will have the opposite effect. Hence, to enable accretion in the pre-main sequence stars, the truncation radius (R_t) needs to be smaller than the co-rotation radius ($R_t < R$co). Once again in figure 3.9, in the interior region to R_t, the disk material will be confined to the stellar fieldlines, will carry the same angular velocity as the star and material is accreted to magnetospheric columns. Outside R_{co} the stellar angular velocity is super-Keplerian, therefore material locked to the stellar field may experience a centrifugal force which will lead to an outer star-disk region (Matt and Pudritz, 2005b; Bouvier et al., 2007).

The presence of outflows such as stellar winds, magnetospheric ejections and disk-winds could also explain and/or complement the efficient angular momentum extraction from a star-disk system with a dipolar magnetosphere. In figure 3.10 three types of outflows in a star-disk system are represented: stellar winds accelerated along the open magnetic flux anchored onto the star, magnetospheric ejections associated with expansion and reconnection processes of closed magnetic fieldlines connecting the star and disk-winds (including X-winds) launched along the open stellar magnetic surfaces threading the disk (Bouvier et al., 2014; Zanni and Ferreira, 2013).

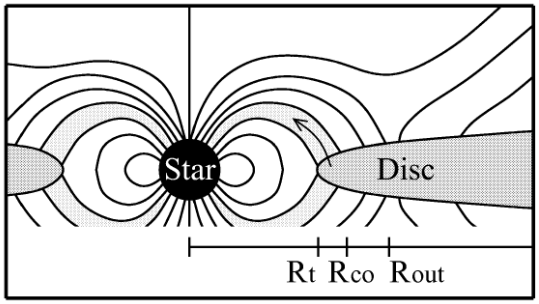

Figure 3.9: Illustration of the magnetic star-disk interaction by Matt and Pudritz (2005b). From the truncation radius R_t to the outer radius R_{out}, that region of the disk is connected to the star through the accretion flow (arrow).

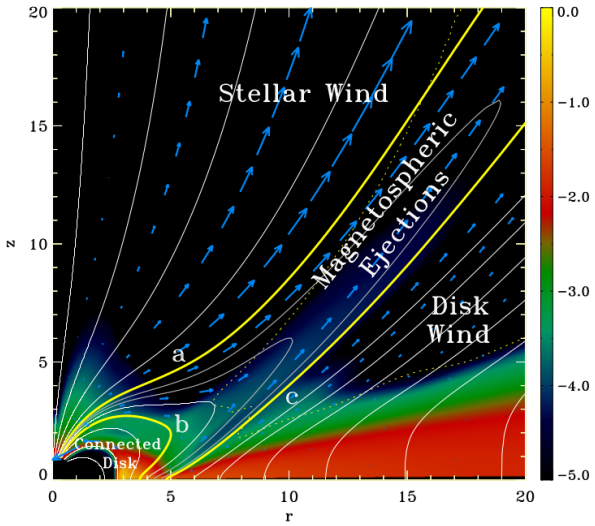

Figure 3.10: Representation of a star-disk interacting system with three different dynamical constituents of the system: (a) stellar winds, (b) magnetospheric ejections and (c) disk-winds. A logarithmic density map is shown in the background. Blue arrows represent poloidal velocity vectors. The dotted line marks the Alfvén surface and the white lines represent the field lines (Zanni and Ferreira, 2013).

The magnetic star-disk interaction, besides their effect on the star angular momentum evolution and the inner structure of the disk, could also have an important role regarding the migration of young planets close to the central object (Lin et al., 1996). The authors suggest that initially a planet forms at a greater distance from the star (~ 5 AU), and afterwards it subsequently migrates inwards through interactions with the remnants of the circumstellar disk. Moreover, tidal interactions with the star, or through truncation of the inner circumstellar disk by the stellar magnetosphere, may be responsible for interrupting the migration of the planet in its present orbit.

Chapter 4

Diagnostic line profiles

The observational study and analysis of this thesis project started with a sample of 58 reduced échelle spectra of T Tauri stars taken by António Pedrosa (from 1998 November 7 to 9) with UES (Utrecht Echelle Spectrograph) at the 4.2 m William Herschel Telescope, installed at the Spanish Observatorio del Roque de los Muchachos of the Instituto de Astrofísica de Canarias, on the island of La Palma. All spectra were originally wavelength-corrected for heliocentric velocity and normalized to a continuum level of unity.

When modelling accretion and outflow mechanisms, the strength and profile of the emission lines reveal to be useful tools (Fernandez et al., 1995). The spectra of CTTS includes emission line profiles that can give hints regarding outflow/accretion signatures. According to White and Basri (2003) classification, each star of the sample was classified as classical (if $W_\lambda(H\alpha) > 10$Å, where W_λ is the equivalent width) or weak line (if $W_\lambda(H\alpha) < 10$Å). Subsequently, the sample was reduced to 38 CTTS, the most active stars. In these selected sample, three stars were discarded: V510 Cas, V1082 Cyg and V1331 Cyg. In the first case, it was the most noisy spectrum in all the sample. The second star was discarded because the spectral type was not defined in many references. The spectrum of V1331 Cyg is a continuum spectrum with emission lines, therefore due to the lack of photospheric absorption lines, it was not possible to make the radial velocity determinations.

Because the spectra were already corrected from the heliocentric velocity, it was only necessary to make a final correction from the radial velocity (RV). The corrections adjust the stars observed velocity from the rotation and translation motions of Earth. In order to determine radial velocities for each spectrum, were used two routines from IRAF[1] (see table 4.1). The `fxcor` routine determines radial velocities through Fourier cross correlation by giving as inputs the spectrum of the star, a template (in the stellar rest-frame) and respective apertures of the échelle spectrum with less noise and strong emission lines. The `rvidlines` routine calculates the radial velocities through the determination of wavelength shifts in spectral lines relative to specified rest wavelengths. Contrary to `fxcor`, `rvidlines` does not give any

[1] Image Reduction and Analysis Facility: `http://iraf.noao.edu/`

associated error.

Later, from the two radial velocities obtained the best one was picked up to make the correction. In order to make this selection, for each observed spectra were added/subtracted, separately, each radial velocity value determined by the two routines and compared with a simulated spectra (template). The selected velocity (marked with an asterisk in table 4.1) was the one for which the shift would lead to an approximate/coincident overlap of photospheric lines between the observed and simulated spectra. Once the correction was done, the spectra were finally transformed into the stellar rest frame.

Taking all into account, most of the radial velocity corrections were made using the values obtained through `fxcor` routine. The `rvidlines` routine returned in many cases negative velocities contrasting with the positive ones determined by `fxcor` and available in the literature. This negative sign could be a result of applying the `rvidlines` routine in noisy spectra. Probably, IRAF identified noise as spectral lines given to make the comparison. One way to deal with this problem could be the selection, of the given list of spectral lines, according to less noisy wavelength intervals. When comparing the chosen RVs with the ones documented in the literature, some values are quite proximate namely for AA Tau, BP Tau, DL Tau, DQ Tau, DS Tau and GK Tau, for instance.

Besides radial velocity determinations, equivalent widths for different chemical elements were measured through IRAF's `splot` routine, namely: Hα 6563Å, Hβ 4861Å, He I 5876Å, Ca II triplet (8498, 8542 and 8662Å), Paschen line P11 8863Å, [OI] 6300Å, [SII] 6731Å and OI 7772Å listed in table 4.2. For the latest element, some inverse P Cygni (IPC) profiles were detected and indicated in the table, but they are not very strong.

The equivalent width is a quantitative tool to measure the strength of a line in emission/absorption. Considering an absorption line in figure 4.1, the equivalent width W_λ is given by an integral over the line

$$W_\lambda \equiv \int (1 - F_\lambda/F_0) d\lambda, \tag{4.1}$$

where F_λ and F_0 are the specific flux received from the star and the continuum flux on either side of the absorption dip, respectively. According to the last figure, this quantity can be interpreted as the width of a hypothetical line with rectangular profile, that represents the same integrated flux deficit from the continuum as the true one (Stahler and Palla, 2005).

For the Hα line, the equivalent width measurements were compared later with the values determined through a Python[2] script (see figure 4.2 and table 4.3). The equivalent width is more dependent of the continuum normalization than signal to noise ratio (S/N), which measures the strength of the signal relatively to background noise. For such matter, the error for the equivalent width of Hα was determined considering the corresponding values above and below 1% of the continuum ($W_{\lambda+1\%}$ and $W_{\lambda-1\%}$,

[2] www.python.org

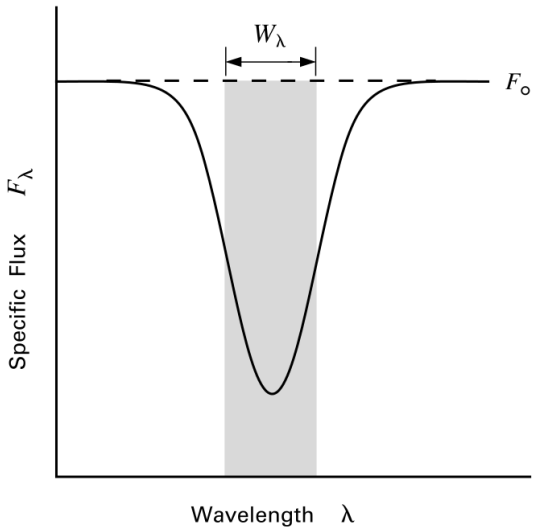

Figure 4.1: Representation of the definition of equivalent width for an absorption line (Stahler and Palla, 2005).

respectively):

$$\text{Error } W_\lambda(\text{H}\alpha) = \frac{1}{2}\left(|W_\lambda - W_{\lambda+1\%}| - |W_\lambda - W_{\lambda-1\%}|\right), \tag{4.2}$$

where W_λ is the equivalent width measured along the continuum.

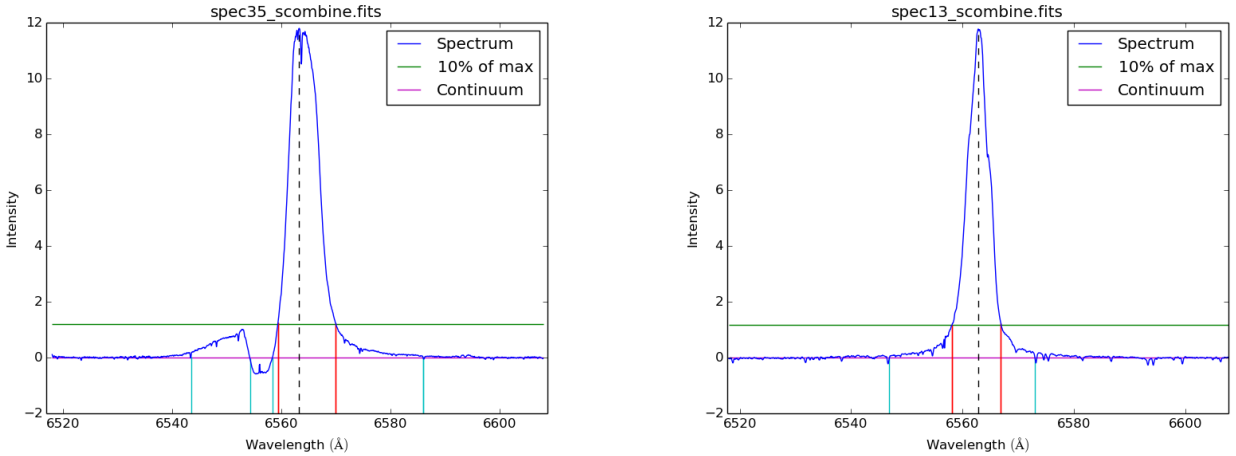

(a) AS 353A **(b)** BP Tau

Figure 4.2: Determination of equivalent widths for Hα emission line through a Python script for AS 353A (P Cygni profile) and BP Tau (gaussian-like profile). The green and magenta horizontal line marks 10% of the maximum intensity of the line and the continuum, respectively. Red and blue vertical lines mark the widths of the line at 10% of the maximum intensity and at the continuum, respectively.

Whenever two emission lines are well correlated, they are probably formed in the same region. For such matter, correlations between different line elements were made. In figure 4.3 were plotted the correlations for various lines including Hα 6563Å, Hβ 4861Å, He I 5876Å, Ca II 8498, 8542, 8662Å and P11 8863Å. In figures 4.3e and 4.3f, there is a low correlation between the line strengths of Hα with He I and Hα with P11. In contrast, in figure 4.3d, Hα and Hβ show the strongest correlation (Pearson correlation coefficient $= 0.837$), suggesting a common emitting region.

Muzerolle et al. (1998b) suggest that Ca II triplet lines are good indicators of accretion rates. The remaining plots correspondent to He I and Ca II triplet correlations, are somewhat less correlated at higher line strengths, as seen by the latest authors. Line profiles for Ca II triplet were not studied in detail for this thesis, but according to Hamann and Persson (1992), in these lines a broad and a narrow component can be identified. While the broad emission component is thought to come from an extended envelope with large turbulent velocities (apart from the stellar surface), the narrow component results from chromospheric activity in the star. For the latest, Batalha et al. (1996) suggest that the emission comes from the chromospheric active regions correlated with local concentration of fieldlines generated by stellar dynamo (the product of the combined effect between stellar differential rotation and subphotospheric convection). Later, Azevedo et al. (2006) besides suggesting that the narrow component fluxes may come from a hot chromosphere, they can also have their origin in accretion shock or wind, while the fluxes from the broad component are probably formed in the magnetospheric accretion flow.

Probably, the low correlation between He I and Ca II triplet seen in figure 4.3 may be related not only with different origin from He I, but also with the distinct origins for the two components in the Ca II triplet, as seen previously. Another important factor to take into account is veiling. Since the continuum excess is wavelength dependent, it will be more relevant for He I (at a lower wavelengths) than for Ca II (at higher wavelengths). Because the analysed spectra were not veiling corrected, variations in the continuum excess will probably lead to variations in the equivalent width of the lines and affect the correlations made.

In table 4.2 are listed the equivalent widths measured for He I $\lambda 5876$, Hα $\lambda 6563$ and OI $\lambda 7772$, and in table 4.3 are shown the determined accretion rates through Natta et al. (2004) empirical relationship for the Hα line (described in the following section). As seen previously in figure 4.3e, there is a correlation between Hα and He I $\lambda 5876$, where $W_\lambda(H\alpha)$ values increase with W_λ(He I). Additionally, when comparing these two last lines with OI $\lambda 7772$ and the determined accretion rates, it is possible to observe that, in a few cases, higher accretion rates are associated with OI in absorption ($W_\lambda > 0$), including IPC profiles. For instance, the highest value verified for $\dot{M}_{\text{acc}}$ corresponds to $10^{-6.18}\ M_\odot/yr$ for RW Aur, which has the highest absorption measured for OI within an IPC profile. In contrast, AA Tau presents lower equivalent widths, including OI in emission, and the lowest value among accretion rates, $10^{-11.31}\ M_\odot/yr$. It should be mentioned that these results could be influenced by the star inclination relatively to the observer and veiling. One way to obtain a proper correlation could be analysing the corresponding fluxes and/or luminosities for all the lines.

Table 4.1: Radial velocity determinations for each star identified in the 1^{st} column. In the 2^{nd} column are shown the spectral types, the 3^{rd} column shows the radial velocity values available in the literature. 4^{th} and 5^{th} columns correspond to radial velocity determination through IRAF's `fxcor` routine and associated error, respectively. In the last column are shown the radial velocities determined with `rvidlines` routine. The chosen RVs for the correction are followed by an asterisk.

Object	Spectral type	RV$_{lit}$ (km/s)	RV$_{fxcor}$ (km/s)	Error RV$_{fxcor}$ (km/s)	RV$_{rvidlines}$ (km/s)
AA Ori	K4[i]	18.8[q]	25.3*	0.7	26.7
AA TAU	K7[t]	17.1[b]	16.8*	0.6	16.4
AS 353A	K2[t]	−12.1[p]	−7.9*	1.9	−10.0
BM And	K5[a]	−27[k]	−8.1*	2.5	−5.7
BP Tau	K7[a]	16.18[c]	17.8*	1.6	18.0
BZ Sgr	K0Ve[r]	−5.4[r]	−1.7*	6.0	0.6
CI Tau	K7[a]	16.2[r]	−57.9	4.8	1.4*
CW Tau	K3[a]	16.4 ± 1.3[j]	30.8	2.0	26.7*
DF Tau	M2[a]	12[g]	172.5	6.4	9.7*
DG Tau	K6[a]	17.9[f]	−26.9	7.9	21.2*
DI Cep	G8[a]	−10[g]	−12.6	3.3	−11.5*
DK TAU	K7[a]	15.3[j]	19.2*	2.0	20.4
DL Ori	K1[e]	?	24.2*	2.2	−61.7
DL Tau	M0[a]	16[l]	17.9*	1.6	−35.0
DQ Tau	K7-M[s]	22.4[n]	22.7*	0.9	22.6
DR Tau	K7[a]	16.5[f]	23.3*	0.7	−22.7
DS Tau	K5[i]	13[l]	14.2*	1.1	7.6
EH Cep	K2[i]	?	−19.7	1.8	−9.5*
GK Tau	K7[a]	18.6 ± 1.4[j]	17.6*	1.4	14.7
GM Aur	K7[a]	15.0 ± 1.3[j]	15.9	0.9	13.7*
LkHα 191	K0[a]	?	−7.1*	0.4	−7.3
LkHα 330	G2[t]	20[k]	15.1	1.2	6.4*
RW Aur	K2[a]	14.0 ± 4.9[j]	15.9*	2.1	3.6
RY Tau	K1[a]	17.8[f]	7.7	2.2	20.4*
T Tau	K0[a]	23.9[g]	18.6	0.6	17.4*
UY Aur	K7[a]	18[d]	16.2*	1.3	23.7
UZ Tau E	M1.3[i]	2.8 − 36.8[m]	18.5	3.1	17.3*
V1079 Tau	K5[t]	?	17.4	0.6	16.3*
V1305 Ori	K5[e]	?	28.9*	2.2	25.9
V1980 Cyg	G[i]	?	−8.6*	3.1	4.4
V466 Ori	K1[t]	23.2[j]	34.3	1.7	27.9*
V625 Ori	K6[i]	?	−20.9	2.4	−16.9*
V649 Ori	G8III – K4V[s]	36[l]	27.4*	1.8	21.9
V828 Cas	K1[i]	?	−0.7*	0.8	−1.2
WY Ari	K5[t]	9[k]	−5.9*	2.7	−7.6

References: a - Artemenko et al. (2012); b - Bouvier et al. (2003); c - Chubak and Marcy (2011); d - Edwards et al. (1987); e - Fang et al. (2009); f - Gahm et al. (2005); g - Gontcharov (2006); h - Gramajo et al. (2014); i - Grankin et al. (2007); j - Hartmann et al. (1986); k - Herbig (1977); l - Joy (1949); m - Martín et al. (2005); n - Mathieu et al. (1997); o - Petrov et al. (2014); p - Rice et al. (2006); q - Tobin et al. (2009); r - Torres et al. (2006); s - The International Variable Star Index (http://www.aavso.org/vsx/index.php); t - SIMBAD (http://simbad.u-strasbg.fr/simbad/).

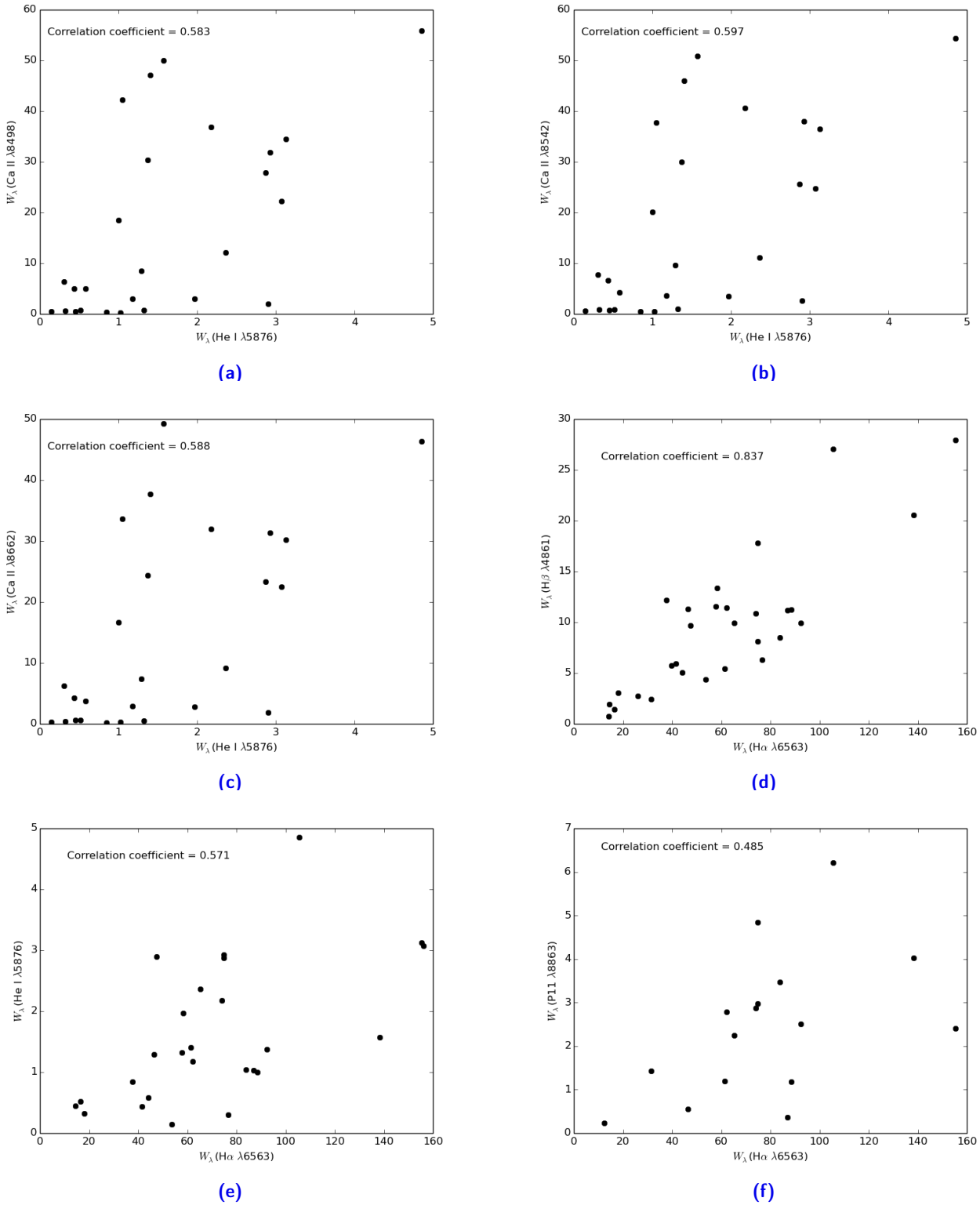

Figure 4.3: Equivalent width W_λ correlation between He I $\lambda 5876$ and Ca II $\lambda\lambda 8498, 8542, 8662$, H$\alpha$ $\lambda 6563$ with Hβ 4861, He I $\lambda 5876$ and P11 $\lambda 8863$. All measurements were made in angstroms and the Pearson correlation coefficients are mentioned at the top-left corner of each plot.

Table 4.2: Equivalent widths measured in IRAF for different chemical elements in angstroms (Å). Positive values refer to absorption lines while negative ones refer to emission lines. Inverse P Cygni profiles (IPC) are mentioned for OI λ7772.

Object	Hα 6563	Hβ 4861	He I 5876	Ca II 8498	Ca II 8542	Ca II 8662	P11 8863	[SII] 6731	[OI] 6300	OI 7772
AA Ori	−13.57	1.37	–	−0.46	−0.39	−0.18	–	–	–	0.07
AA TAU	−16.64	−1.44	−0.52	−0.70	−0.93	−0.66	–	–	–	−0.08
AS 353A	−83.78	−8.49	−1.05	−42.20	−37.77	−33.67	−3.46	–	–	0.74
BM And	−38.63	–	–	–	–	–	–	–	−0.04	1.05
BP Tau	−57.72	−11.56	−1.32	−0.69	−0.96	−0.56	–	–	–	–
BZ Sgr	−65.41	−9.94	−2.36	−12.09	−11.15	−9.13	−2.24	–	−0.22	−0.23/1.45 (IPC)
CI Tau	−74.85	−17.82	−2.87	−27.83	−25.59	−23.31	−2.97	–	−0.02	−0.65/0.30 (IPC)
CW Tau	−92.32	−9.95	−1.37	−30.36	−30.04	−24.34	−2.51	−0.24	−0.17	−0.21/0.96 (IPC)
DF Tau	−47.38	−9.71	−2.90	−2.01	−2.63	−1.90	–	–	−0.25	−0.09/1.13 (IPC)
DG Tau	−73.95	−10.89	−2.18	−36.84	−40.59	−31.98	−2.87	−1.94	−7.8069	−0.61
DI Cep	−88.62	−11.23	−1.00	−18.53	−20.14	−16.62	−1.18	–	–	−1.20
DK TAU	−46.45	−11.30	−1.29	−8.54	−9.59	−7.45	−0.55	–	–	−0.45
DL Ori	−138.21	−20.59	−1.57	−49.97	−50.91	−49.25	−4.02	−0.09	−0.15	−1.32
DL Tau	−105.45	−27.09	−4.86	−55.86	−54.42	−46.38	−6.21	–	−0.07	−0.89
DQ Tau	−53.58	−4.36	−0.14	−0.45	−0.66	−0.32	–	–	–	0.12
DR Tau	−74.83	−8.14	−2.93	−31.87	−38.05	−31.33	−4.84	–	–	−1.44/1.16 (IPC)
DS Tau	−58.24	−13.37	−1.97	−3.03	−3.46	−2.80	–	–	–	−0.08
EH Cep	−15.02	–	–	−3.98	−3.07	−2.61	–	–	–	−0.20/0.56 (IPC)
GK Tau	−18.13	−3.04	−0.33	−0.69	−0.87	−0.38	–	–	–	–
GM Aur	−87.00	−11.21	−1.03	−0.31	−0.51	−0.31	−0.36	–	–	−0.01
LkHα 191	−14.28	−0.75	–	−0.32	−0.65	−0.39	–	−0.04	–	0.14
LkHα 330	−14.53	–	–	0.61	1.03	1.32	–	–	–	0.11
RW Aur	−61.36	−5.46	−1.41	−47.14	−46.05	−37.75	−1.20	–	–	−0.08/2.52 (IPC)
RY Tau	−12.32	1.42	–	−1.62	−0.64	−0.99	−0.23	−0.22	−0.02	0.39
T Tau	−76.56	−6.34	−0.31	−6.33	−7.70	−6.26	–	−0.43	−0.30	−0.34
UY Aur	−62.10	−11.42	−1.18	−3.05	−3.67	−2.95	−2.79	−0.21	−0.23	−0.03/0.98 (IPC)
UZ Tau E	−37.76	−12.20	−0.84	−0.40	−0.56	−0.24	–	–	–	0.18
V1079 Tau	−14.39	−1.96	−0.45	−0.49	−0.71	−0.61	–	–	–	0.04
V1305 Ori	−39.69	−5.76	–	−5.81	−6.90	−5.39	–	–	–	−0.35
V1980 Cyg	−31.45	−2.46	–	−21.08	−20.54	−18.74	−1.42	–	–	−0.44
V466 Ori	−26.00	−2.72	–	−5.25	−4.85	−3.88	–	–	–	0.11
V625 Ori	−44.11	−5.08	−0.58	−5.02	−4.27	−3.73	–	–	–	−0.33
V649 Ori	−41.59	−5.96	−0.44	−5.03	−6.66	−4.31	–	–	–	–
V828 Cas	−13.97	–	–	−0.70	−0.50	−0.25	–	–	–	0.05
WY Ari	−155.40	−27.94	−3.13	−34.46	−36.46	−30.24	−2.40	–	–	−3.65

4.1 STELLAR DYNAMICS THROUGH SPECTRA

In this section, CTTS dynamics will be analysed through spectra of the selected sample. The most relevant lines studied include Hα, He I $\lambda5876$ and $\lambda6678$ and the forbidden lines of [OI] and [SII].

He I lines are associated with emission from the accretion shock at the base of the infalling matter and are usually present among stellar objects for which accretion was also verified through the Hα line. The latest is also an indicator for outflows due to the presence of a blueshifted absorption component. Forbidden emission lines are usually associated with winds and jets (Bouvier et al., 2007).

Hα

The Hα line is commonly observed among young stars due to its strong and broad emission, generated from the high temperatures and high velocities of winds and accreting cirmcumstellar material (White and Basri, 2003). Because Hα line is optically thick, the line results from contributions of different regions around the star where different physical and dynamical conditions may exist. It has been thought that the flux of this line has its origin in a dense chromosphere (Herbig, 1970) or boundary layer (Basri and Bertout, 1989), but on the other hand, P Cygni profiles among Hα lines also accuse the presence of winds with terminal velocities near $400\,km/s$. Moreover, Artemenko et al. (2012) affirms that CTTS with more intense Hα lines are associated with larger specific angular momentum, suggesting that accretion acts like a momentum regulator.

Usually mass accretion rates have been studied for low mass objects, mainly through Hα line model-fitting, veiling measurements (Muzerolle et al., 2003), radiative transfer models and accretion luminosities (Gullbring et al., 1998). Natta et al. (2004) found that the width of Hα measured at 10% of the peak intensity (Hα 10%) is an accretion indicator, giving reasonable estimates for mass accretion rates ($\dot{M}_{\rm acc}$) covering a wide range of stellar masses and can be applied from T Tauri stars to brown dwarfs. According to the previous authors, the relation between Hα 10% and $\dot{M}_{\rm acc}$ is given by the following empirical relationship:

$$\log \dot{M}_{\rm acc} = -12.89(\pm0.3) + 9.7(\pm0.7) \times 10^{-3} H\alpha 10\%, \tag{4.3}$$

where the Hα 10% width is in km/s and $\dot{M}_{\rm acc}$ is in $M_{\odot}/yr$.

Based on equation (4.3) for the Hα line, mass accretion rates and respective errors were determined through a simple Python script for each spectrum and listed in table 4.3. In the latest, are also shown the equivalent widths measured both with the `splot` routine from IRAF and the mentioned script as well as the associated error, the width of Hα measured at 10% in km/s. The profile types were classified both according with Finkenzeller and Mundt (1984) and Reipurth et al. (1996) classifications.

According to the first reference, *s* refers to a single symmetric emission peak, *PCyg* to a P Cygni profile

and *d* states for double-peak profile with a central absorption. Regarding the second one, the classification follows the scheme presented in figure 4.4, where the dotted line marks half of the maximum intensity. Type I profiles are symmetric and gaussian-like, type II shows two peaks, where the secondary one exceeds half the maximum intensity of the first peak. Type III profiles have two peaks, and the secondary one has less than half the maximum intensity of the first peak. Type IV profiles refer to pure P Cygni or inverse P Cygni profiles, for which no secondary peak is observed. If the secondary peak is located bluewards or redwards relatively to the primary peak, B or R letters are appended to the roman numeration (Reipurth et al., 1996).

According with Reipurth et al. (1996) classification scheme, in the active sample of 35 CTTS, the IIIB profile is more common, while for Finkenzeller and Mundt (1984) classification the double-peak profile d is the most observed for Hα emission lines.

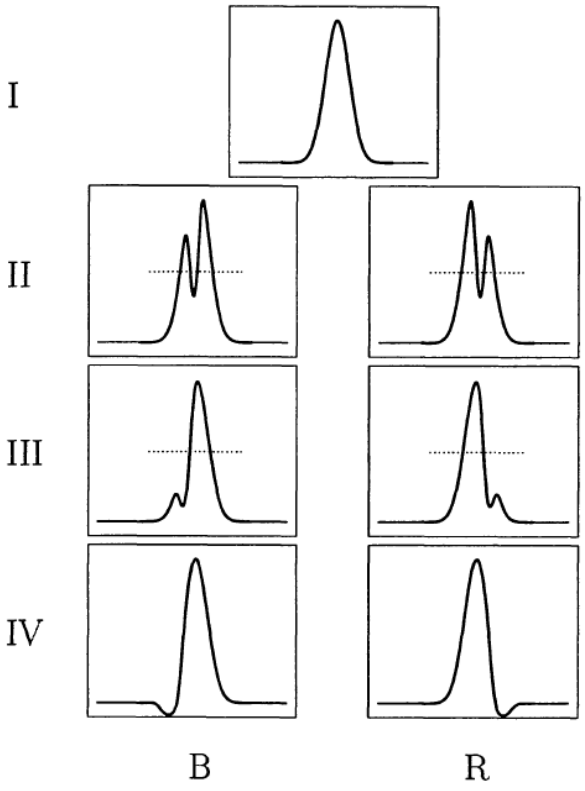

Figure 4.4: Reipurth et al. (1996) classification scheme for Hα emission line profiles. The dotted line marks 50% of maximum line intensity.

The determined mass accretion rates ($\dot{M}_{\text{acc}}$) vary from $10^{-11.3}$ for AA Tau, to $10^{-6.2}$ $M_{\odot}/yr$ for RW Aur, with corresponding Hα at 10% widths of 162.8 and 691.2 km/s and associated errors (in logarithmic scale) of 0.4 and 0.8, respectively. In figure 4.5, the accretion rates determined are mainly between 10^{-9} to 10^{-8} $M_{\odot}/yr$ and $10\%H\alpha$ widths are more recurrent between 400 to 450 km/s.

Although some differences between the determined mass accretion rates by equation (4.3) and the ones found in the literature, it should be taken into account that the $\dot{M}_{\text{acc}}$ determined through veiling, radiative transfer models, accretion luminosities or other methods, will all return slightly different results. Other factors that can influence mass accretion rates include the number of accretion columns unevenly spaced,

leading to individual emission line variable intensities over periods of days with the rotation of the star (Costigan et al., 2012). Also, inclined magnetospheres are needed to explain periodic variations regarding emission line and veiling fluxes among some CTTS (e.g. Johns and Basri (1995)), that could come from the variations of the projected funnel and shock geometry as the star rotates. For all these reasons, Frank et al. (2014) suggested that time-averaged accretion values should be considered when comparing mass accretion values.

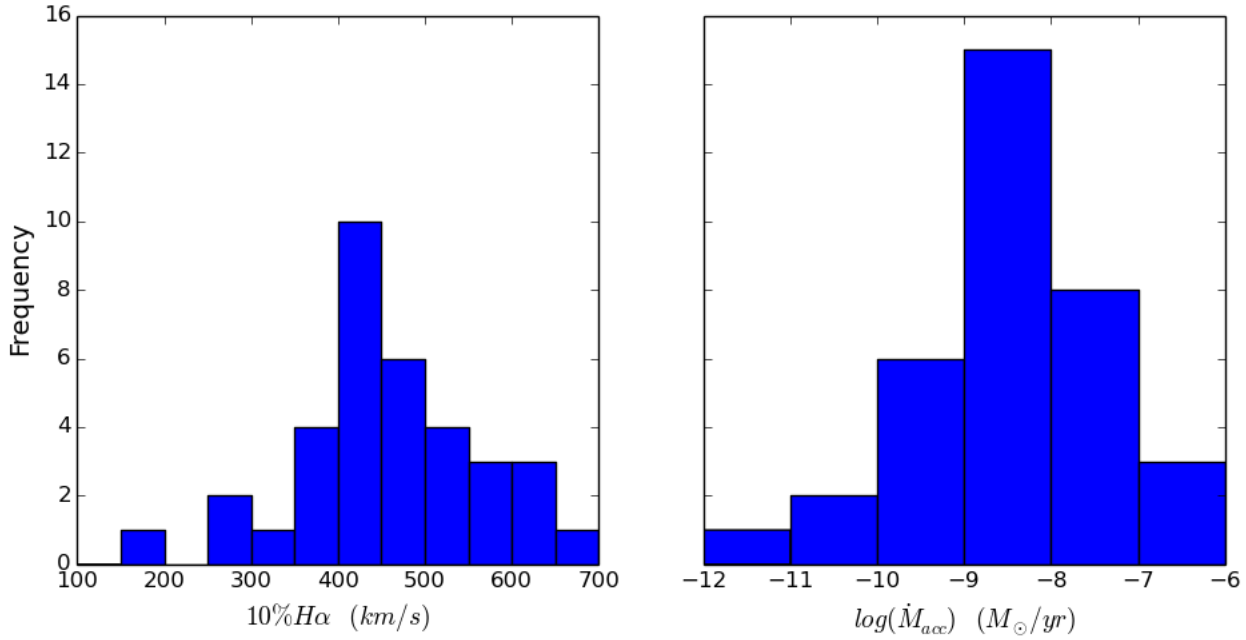

Figure 4.5: Distribution of Hα at 10% widths ($10\%H\alpha$) and mass accretion rates ($\dot{M}_{\rm acc}$) determined with Natta et al. (2004) empirical relation.

He I

Another spectral indicator of magnetospheric accretion is the presence of narrow and broad components in emission lines, which are thought to have chromospheric origin or even arise from the post-shock accreting gas (Batalha et al., 1996; Hartmann, 2009). Broad line profiles are usually asymmetric, have typical widths in excess of $100\ km/s$ and may include blueshifted and/or redshifted absorption components. Narrow profiles are centred at the line centre and are usually superposed on top of a broad component (Muzerolle et al., 1998b). Such spectral features can be found namely in He I at 5876Å and 6678Å emission lines, for instance.

Eleven stars of the selected active sample showed both line emission profiles for He I at $\lambda5876$ and $\lambda6678$. In figure 4.6 are shown the overlapped emission line profiles with mostly redshifted peaks. In the last figure, the line profiles for each star are quite identical to each other suggesting that line emission comes from the same region. Nevertheless, $\lambda5876$ intensity is always higher than $\lambda6678$. Additionally, there is evidence of the existence of a broad and a narrow component, as mentioned by Batalha et al.

(1996). The latest may be formed in a post-shock gas (Hartmann, 2009), while the broad components are thought to be formed in the magnetosphere (Muzerolle et al., 1998b). According to the authors, more veiled stars have more narrow component flux, controlled by accretion.

These line profiles are thought to be produced in an infalling magnetosphere, evidenced by the redshifted absorption (Hartmann et al., 1994). The redshifted absorption in the red wing or at the red edge of the emission profile leads to an IPC profile. The latest feature is indicative of high speed mass infall, including radial velocities for the redward edge of the absorption minima between ~ 200 and $300\ km/s$. According to Edwards et al. (1994), these velocities correspond to ballistic infall from heights of $2R_*$ or higher, when considering a TTS with $M_* = 0.5M_\odot$, $R_* = 2.5R_\odot$.

Some IPC profiles for He I at $\lambda 5876$ are not so evident as for DR Tau, where the red emission wing is depressed by the redshifted absorption. By looking to figure 4.6, He I plots of emission lines $\lambda 5876$ and $\lambda 6678$, it is possible to conclude that mass infall has a free falling velocity, near the redward edge of the absorption minimum, ranges between 200 and $400\ km/s$ for $\lambda 5876$, while for $\lambda 6678$ lies between 300 and $500\ km/s$. The observed values are near to the expected velocity range according to Hartmann (2009), where shock velocities are of order the free-fall values between $\sim 200 - 300\ km/s$.

Although DR Tau has the most defined redshifted absorption and has been know by a high accretion rate ($\dot{M}_{\text{acc}} = 10^{-5.4}\ M_\odot/yr$ according to Hartigan et al. (1995)), the determined values through Natta et al. (2004) empirical relationship returned a value of only $10^{-9.1}\ M_\odot/yr$, followed by CI Tau with the lowest rate of $10^{-9.4}\ M_\odot/yr$ in this set of 11 stars. Conversely, RW Aur has the highest accretion rate of the whole active sample followed by WY Ari, with rates of $10^{-6.2}$ and $10^{-7.6}\ M_\odot/yr$, respectively.

Depending on the disk inclination, line profiles could have different spectral characteristics. Edwards et al. (1994) suggested that IPC features may arise from moderate to high inclinations, when infalling gas is seen projected above the hot ring of magnetic footpoints. In addition, Batalha et al. (1996) argue that if the disk is seen nearly edge-on, the resulting narrow emission is centered at the stellar rest velocity. When considering high inclinations the circumstellar disk obscures the central region where the visible light comes from (Akeson et al., 2005). Also, depending on the rotation of the star, lines could be less or more broad. Another mentioned idea is if the narrow component forms in a magnetically controlled circumstellar flow, flux variability is expected due to erratic accretion rates and distinct inclination angles of the magnetic column.

[OI] and [SII]

Among many TTS, emission of optically thin and low-excitation forbidden line radiation is detected. Forbidden lines are good indicators for study wind kinematics and morphology by providing information regarding mass outflow rates, electron densities, wind velocities and radial extent of the wind. It has been accepted that the blueshifted component of forbidden emission lines is formed in jets of TTS at a large distance from the central proto-star, where ionized atoms recombine in the cooling region behind

the shock (Hartigan et al., 1995; Petrov et al., 2014).

Moreover, through [OI] at 6300Å and [SII] at 6731Å emission lines, highly collimated optical jets from YSOs can be detected (Hartmann, 2009). The [OI] and [SII] forbidden lines are characterized by broad, blueshifted, and double-peaked line profiles. The high-velocity component (HVC) has its origin in a fast, collimated jet characterized by low densities and high temperatures. The low-velocity component (LVC) forms in a region of smaller extent close to the star and is generally cooler and denser (Hartigan et al., 1995, 2004).

Among all the stars in the selected active sample, only five of them showed simultaneously emission lines for [OI] $\lambda 6300$ and [SII] $\lambda 6731$: CW Tau, DG Tau, RY Tau, T Tau and UY Tau. When looking to figure 4.7, the [OI] profiles are clearly affected by photospheric absorption lines. One way to correct this issue could be subtracting the spectrum with a template of the same spectral type including this absorption features.

Still in the latest figure, the terminal velocities at which the material is being ejected from the star can be estimated based on the blue edge of the HVC that crosses the continuum. The terminal velocities for [OI] and [SII] range between $\sim [-344, -123]\ km/s$ and $\sim [-338, -116]\ km/s$, respectively. Regarding the LVC, velocities range from $\sim [-50, -20]\ km/s$ for [OI] and $\sim [-60, -30]\ km/s$ for [SII]. Nevertheless, it must be taken into account that [SII] emission is weaker than [OI]. Therefore, it is more difficult to determine a correct terminal velocity for the former.

From the previous figure, is possible to observe both a broad HVC and a narrower and blueshifted LVC, more evident in [OI] than in [SII], suggesting that the two components have different physical origins with different densities and temperatures. The HVC refers to a narrowly directed jet, while the LVC is supposed to be related with an outflow of matter from the surface of an accretion disk (Hartigan et al., 1995; Kwan and Tademaru, 1988; Petrov, 2003). The LVC forms within a few tens of AU from the star, is blueshifted within few km/s and is more pronounced among lines with higher critical densities. Conversely, the HVC has more spatial extension, higher velocities (hundreds of km/s) and carries lower densities relatively to the LVC (Hartigan et al., 2004).

Some authors have concluded that [SII] emission in the HVC comes from a more distant region from the star than the [OI] emission (e.g. Hirth et al. (1994a)). Kwan and Tademaru (1988) associated the HVC to a focused wind from the star boundary layer and the LVC to a disk wind. In addition, it could be that [SII] does not emit strongly in the HVC close to the star because the flow is very dense. Hartigan et al. (1995) concluded that the HVC for forbidden line emissions in TTS has its origin in spatially unresolved emission in a dense stellar jet close to the star and the LVC is present whenever there is a NIR excess. For example, observational data confirmed already that CW Tau has a jet (Hartigan et al., 2004), which is clearly evidenced by the HVC in figure 4.7e.

Clearly, [OI] $\lambda 6300$ emission is stronger than [SII] $\lambda 6731$. In this sample with five stars, the maximum intensity peaks of [OI] are stronger 2 to 8 times the peaks of [SII]. Although in some cases the distinction

between the LVC and the HVC is not so evident, it is possible to observe in figure 4.8 that velocities for the LVC peaks are higher for [SII].

According to Hartigan et al. (1995) there is an inverse correlation between velocity and critical density. [SII] has a lower critical density ($n_e \sim 10^4\, cm^{-3}$, at a formation temperature of 10^4 K) and lower velocity when compared to [OI] ($n_e \sim 10^6\, cm^{-3}$), which is consistent with the idea that both disk wind and accretion column have their signature in the LVC. [OI] has higher critical density and forms closer to the disk relatively to lines with lower critical density as [SII], and the flow speeds up as it rises from the disk.

The inclination of the stars relatively to the observer could lead to the different observed emission profiles. For this sample of five stars, were found the following inclination angle relatively to the rotation axis: less than $30°$ for DG Tau (Isella et al., 2010), $42°$ for UY Aur (Close et al., 1998), $\sim 49°$ for CW Tau (Coffey et al., 2008), at least $65°$ for RY Tau (Isella et al., 2010) and $72°$ for T Tau (Ratzka, 2008).

DG Tau has the lowest inclination angle in this sample, which means that the star is more pole-on orientated. In this case, the observer is able to determine the velocities for the star jet more properly than with a star with high inclination (edge-on). As a matter of fact, DG Tau shows the highest terminal velocities of the sample near $-340\ km/s$. On the other hand, RY Tau and T Tau, besides presenting higher inclinations, the terminal velocities determined for the ouflow are lower, ranging between -123 and $-182\ km/s$. In this small example is possible to conclude that lower inclinations lead to the determination of higher terminal velocities for the jet region.

According to Cabrit et al. (1990), there is a correlation between forbidden line luminosities and accretion processes in CTTS suggesting that winds are powered by accretion. In this case, equivalent widths were analysed instead of luminosities to see if there could be any relation. In general, the results are inconclusive. When looking to figure 4.7, more intense line emissions are associated with higher terminal velocities for the outflow and lower accretion rates. Although there are only five stars to analyse, the results could be affected by the star inclination as well as the excess continuum, which can affect not only the width of Hα (and consequent accretion rate determined), but also [OI] and [SII] emission lines and correspondent terminal velocities for the outflow.

Table 4.3: The W_λs determined in IRAF and through a Python script are in the 2^{nd} and 3^{rd} columns, respectively. Determinations for Hα line width measured at 10% (4^{th} column) and respective errors (5^{th} column), logarithm of mass accretion rates $\dot{M}_{\rm acc}$ ($6^{th} column$) and associated errors (7^{th} column) are shown as well as the values available in the literature $\dot{M}_{\rm lit}$ (8^{th} column). The last two columns (A and B) refer to the classifications of the Hα profile type according to the classification system of Finkenzeller and Mundt (1984) and Reipurth et al. (1996), respectively.

Object	W_λ H$\alpha_{\rm IRAF}$ (Å)	W_λ Hα (Å)	Error W_λ Hα (Å)	10% Hα (km/s)	$\log(\dot{M}_{\rm acc})$ $(M_\odot/yr)$	Error $\log(\dot{M}_{\rm acc})$ $(M_\odot/yr)$	$\log(\dot{M}_{\rm lit})$ $(M_\odot/yr)$	M_* $(M_\odot)$	Profile type A	Profile type B
AA Ori	13.57	13.95	1.31×10^{-1}	565.40	−7.41	0.70			d	II B
AA Tau	16.64	16.33	1.02×10^{-4}	162.84	−11.31	0.41	-8.48^{i}	0.53^{b}	d	II R
AS 353A	83.78	85.94	7.15×10^{-4}	486.23	−8.17	0.64	-5.4^{g}	0.63^{g}	PCyg	III B
BM And	38.63	38.00	9.97×10^{-4}	573.76	−7.32	0.70			d	II R
BP Tau	57.72	59.71	4.21×10^{-4}	402.83	−8.98	0.58	-7.54^{i}	0.49^{b}	s	I
BZ Sgr	65.41	68.30	1.03×10^{-3}	296.55	−10.01	0.51			d	II R
CI Tau	74.85	72.41	2.02×10^{-4}	363.14	−9.37	0.55	-6.8^{g}	0.42^{g}	d/PCyg	II B
CW Tau	92.32	91.17	8.11×10^{-2}	337.35	−9.62	0.54	-8.8^{j}	1.03^{g}	d	II B
DF Tau	47.38	49.67	1.07×10^{-2}	400.72	−9.00	0.58	-5.9^{g}	0.27^{b}	d/PCyg	III B
DG Tau	73.95	74.04	3.72×10^{-2}	407.00	−8.94	0.58	-5.7^{g}	0.67^{g}	d/PCyg	III B
DI Cep	88.62	85.25	8.99×10^{-4}	467.62	−8.35	0.63			PCyg	III B
DK Tau	46.45	47.40	4.80×10^{-2}	455.17	−8.47	0.62	-6.4^{g}	0.43^{b}	d	II R
DL Ori	138.21	139.35	6.66×10^{-5}	448.62	−8.54	0.61			s	III B
DL Tau	105.45	104.59	1.71×10^{-4}	402.83	−8.98	0.58	-7.63^{j}	0.37^{g}	d/PCyg	III B
DQ Tau	53.58	51.44	1.07×10^{-3}	375.68	−9.25	0.56	-7.3^{g}	0.43^{g}	s	I
DR Tau	74.83	75.49	1.49×10^{-1}	388.07	−9.13	0.57	-5.1^{g}	0.38^{g}	PCyg	III B
DS Tau	58.24	59.82	9.74×10^{-4}	511.34	−7.93	0.66	-7.89^{i}	1.28^{g}	d/PCyg	III B
EH Cep	15.02	14.82	2.38×10^{-2}	540.52	−7.65	0.68			d/PCyg	III B
GK Tau	18.13	18.83	5.07×10^{-2}	465.36	−8.38	0.63	-8.19^{i}	0.46^{b}	d	II B
GM Aur	87.00	84.18	1.49×10^{-4}	590.76	−7.16	0.71	-8.2^{a}	0.52^{b}	d	II R
LkHα 191	14.28	14.16	3.74×10^{-4}	273.42	−10.24	0.49			s	I
LkHα 330	14.53	14.27	1.29×10^{-3}	407.03	−8.94	0.58	-8.80^{c}	2.5^{c}	s	I
RW Aur	61.36	62.25	2.00×10^{-1}	691.26	−6.18	0.78	-6.47^{j}	0.85^{g}	d	II B
RY Tau	12.32	12.41	1.86×10^{-2}	601.04	−7.06	0.72	-7.6^{g}	1.63^{g}	d/PCyg	III B
T Tau	76.56	74.48	9.34×10^{-2}	390.24	−9.10	0.57	-8.15 to -7.09^{d}	2.11^{b}	s	I
UY Aur	62.10	62.40	1.79×10^{-4}	442.47	−8.60	0.61	-7.18^{i}	0.29^{g}	s	I
UZ Tau E	37.76	38.35	8.21×10^{-4}	418.74	−8.83	0.59	-5.7^{g}	0.18^{g}	s	II R
V1079 Tau	14.39	13.59	5.08×10^{-4}	419.60	−8.82	0.59	-8.82^{a}	1.05^{a}	d	II R
V1305 Ori	39.69	40.14	1.59×10^{-3}	490.49	−8.13	0.64			s	I
V1980 Cyg	31.45	35.53	4.56×10^{-1}	440.36	−8.62	0.61		2.9^{h}	PCygni	III B
V466 Ori	26.00	25.45	1.20×10^{-3}	611.52	−6.96	0.73			s	III B
V625 Ori	44.11	44.95	5.91×10^{-4}	642.51	−6.66	0.75			d	II B
V649 Ori	41.59	41.94	4.43×10^{-4}	488.38	−8.15	0.64			s	II R
V828 Cas	13.97	14.20	3.50×10^{-4}	544.96	−7.60	0.68			d	II R
WY Ari	155.40	153.00	1.12×10^{-1}	542.65	−7.63	0.68		0.8^{e}	s	II B

References: a - Akeson et al. (2005); b - Bouvier et al. (2007); c - Brown et al. (2008); d - Calvet et al. (2004); e - Carmona et al. (2008); f - Gullbring et al. (1998); g - Hartigan et al. (1995); h - Levreault (1988); i - Muzerolle et al. (1998a); j - Valenti et al. (1993).

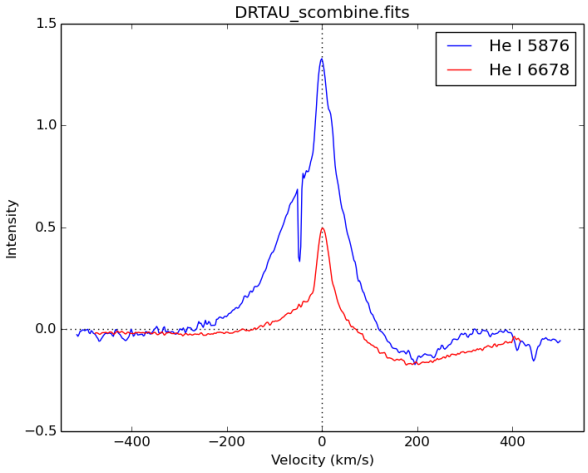

(a) DR Tau

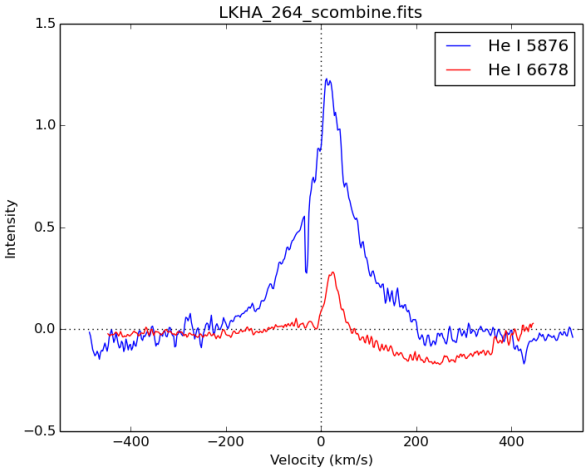

(b) WY Ari

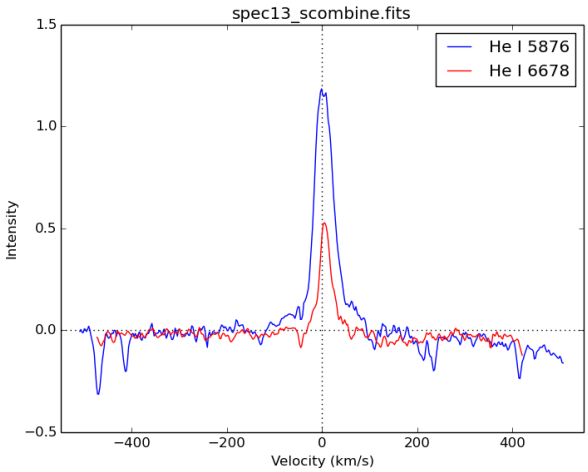

(c) BP Tau

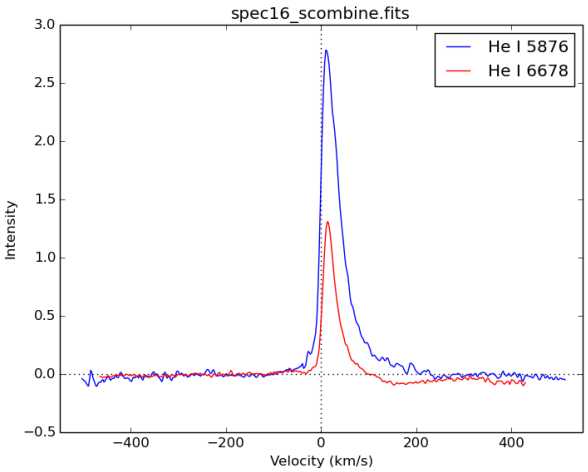

(d) DF Tau

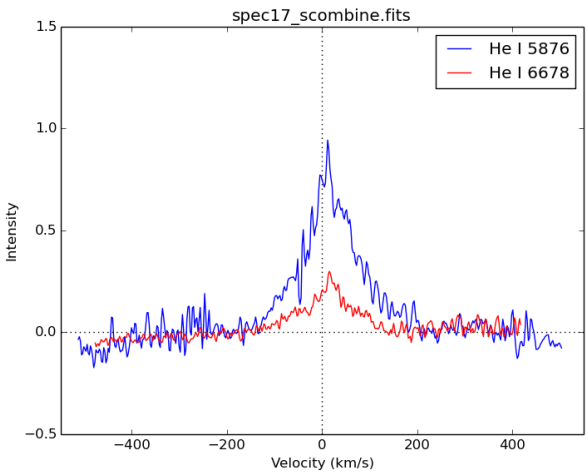

(e) DG Tau

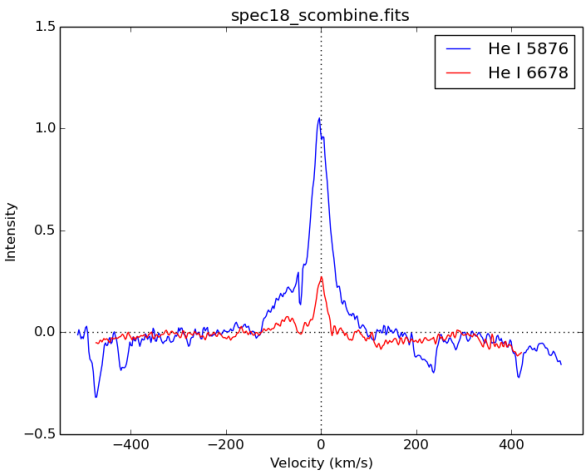

(f) DK Tau

Figure 4.6: Velocity plots for He I lines at 5876Å (blue line) and 6678Å (red line) in km/s. All the plots were corrected from the radial velocity.

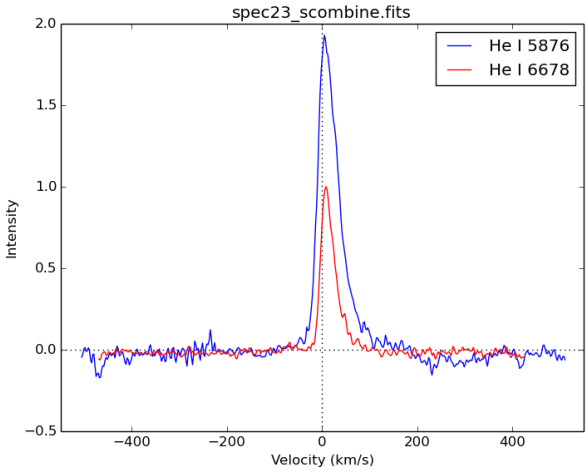

(g) DS Tau

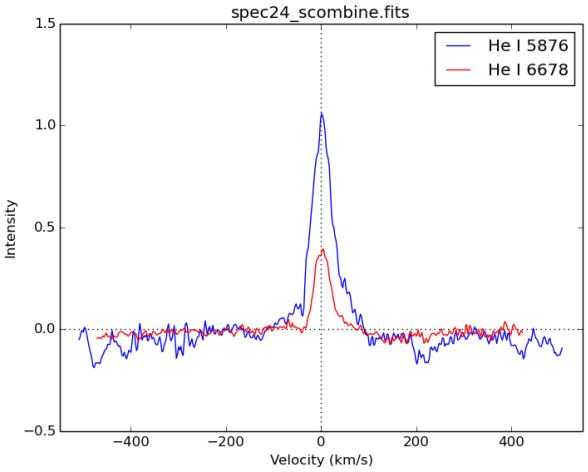

(h) UY Aur

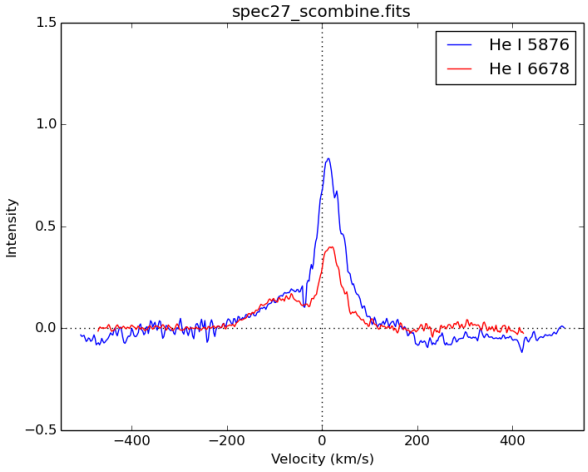

(i) RW Aur

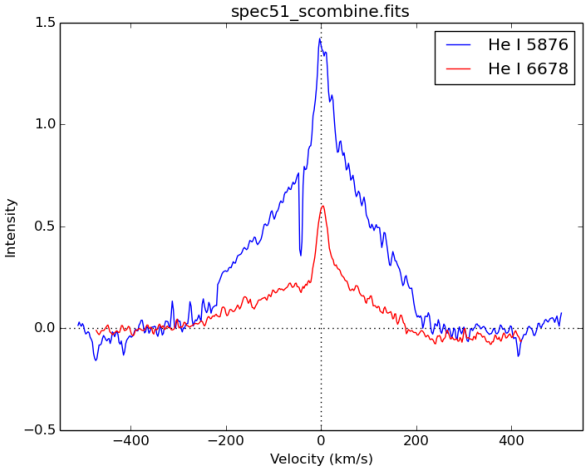

(j) DL Tau

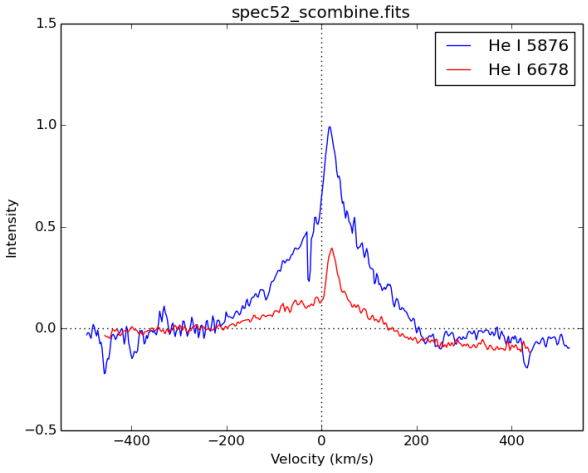

(k) CI Tau

Figure 4.6: (continued)

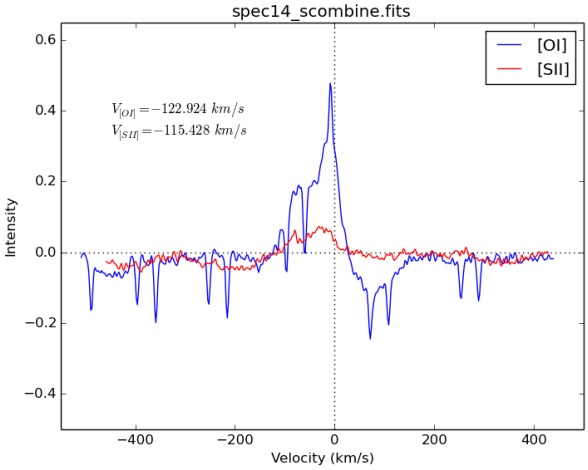

(a) RY Tau

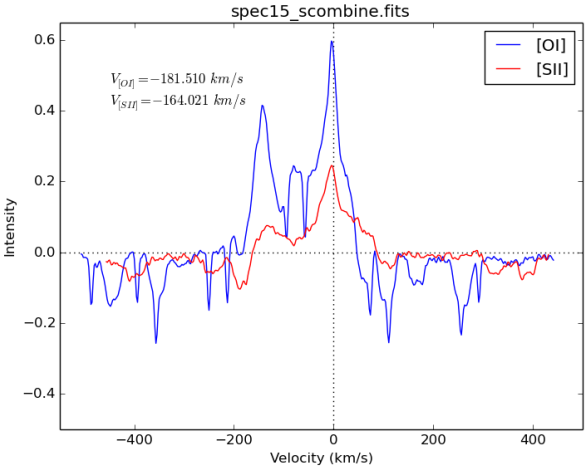

(b) T Tau

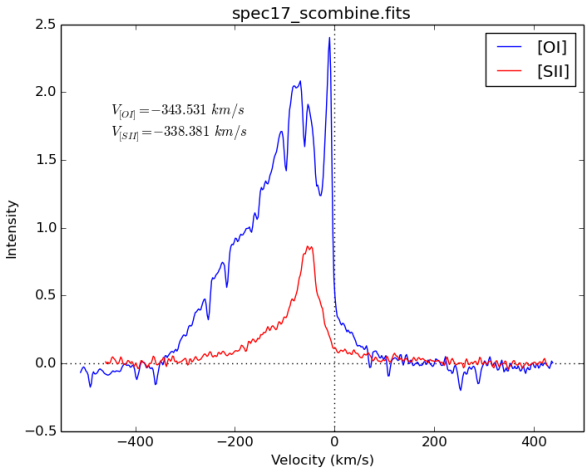

(c) DG Tau

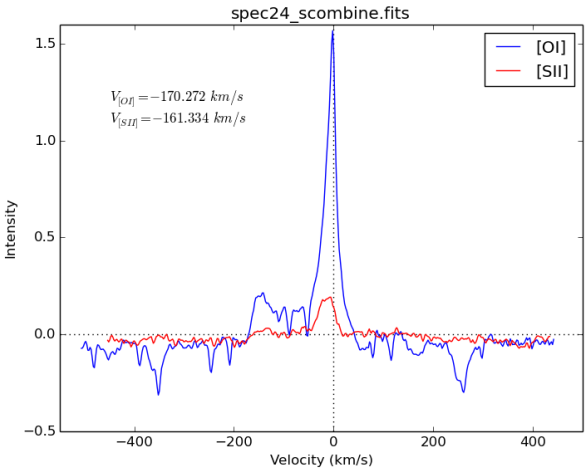

(d) UY Aur

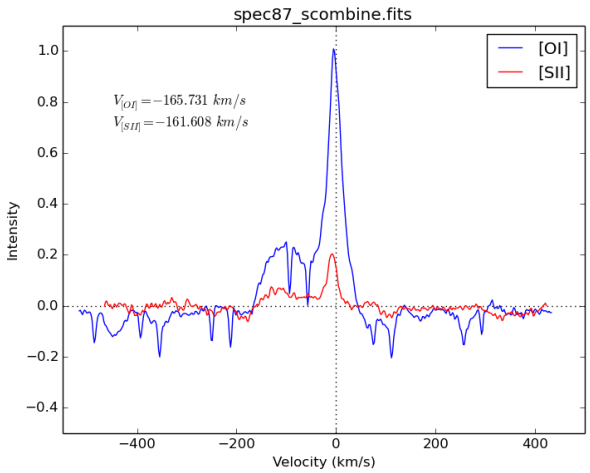

(e) CW Tau

Figure 4.7: Velocity plots for [OI] $\lambda 6300$ (blue lines) and [SII] $\lambda 6731$ (red line) forbidden lines, in km/s. For each plot were determined the terminal velocities for both lines. All the plots were corrected from the radial velocity.

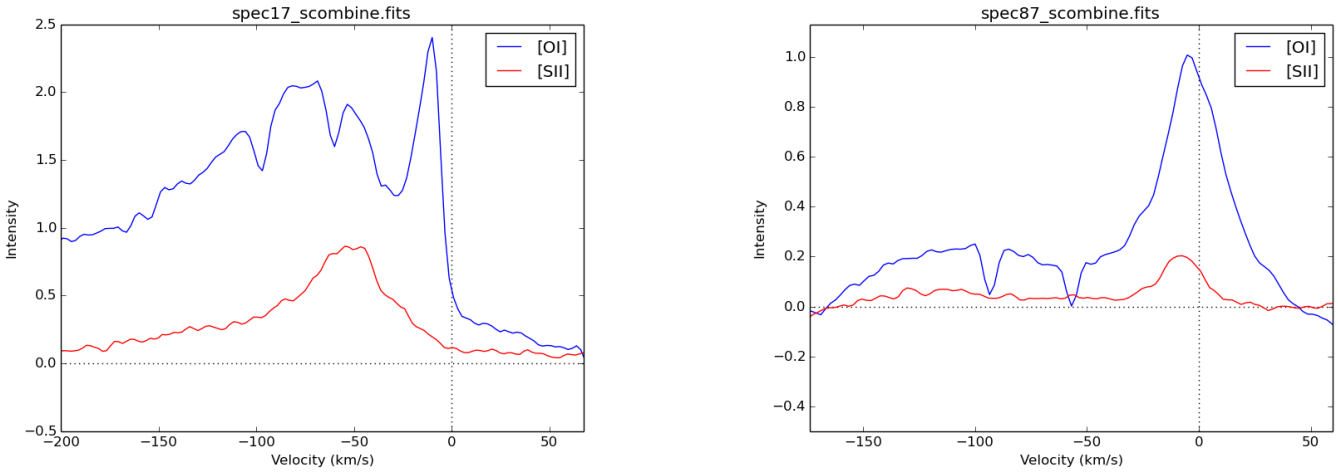

(a) DG Tau **(b)** CW Tau

Figure 4.8: Velocity profiles for [OI] $\lambda 6300$ and [SII] $\lambda 6731$ with a zoom-in for the low-velocity component (LVC) for DG Tau and CW Tau.

4.2 TRIPLE GAUSSIAN FITTING

When analysing emission line profiles, they can be decomposed in gaussian-like components with positive/negative intensities in order to fit emission/absorption features. Since each component is probably linked with a certain emitting region, where inflow and/or outflow processes occur, it would be interesting to evaluate the velocity peaks, intensities and dispersion velocities for the selected sample of CTTS.

The triple gaussian fitting (3GF) is able to adjust three gaussians to any emission line. Besides the spectrum, an initial condition vector (with central wavelength, peak intensity and standard deviation for each gaussian) and some additional constraints are introduced as inputs in a Python script. A first gaussian is fitted according to the maximum line intensity and a second one with the wings of the emission line. Finally, a third gaussian with negative intensity is introduced to fit possible strong absorptions. The fitting resorts of `mpfit.py`[3] function available for Python users, which uses the Levenberg-Marquardt optimization technique to solve the least-squares problem. Within certain constrains, that can be adjusted by the user, `mpfit` will converge to the best set of parameters for the data given as input, for which the sum of the weighted squared differences between the model and data is minimum. The mentioned routine purpose is to fit the sum of the three gaussians for each emission line profile of the sample of CTTS.

Line profiles

Hα

The majority of the profiles in the Hα line are asymmetric, double peaked and the line wings often extend near to $\pm 400\ km/s$, indicative of large-scale gas flows. While the main peak is closer to the line center, the secondary maximum is located at bluer wavelengths. This feature is shaped by an absorption dip overlapping the underlying symmetric emission profile. Muzerolle et al. (2001) concluded that blueshifted absorption components cannot be explained without including a wind outside of the magnetosphere. According to Stahler and Palla (2005), the absorption feature must arise from a partially opaque layer of gas at low densities moving away from the emission source. Therefore, this spectral feature accuses the presence of a stellar wind.

In the selected sample, P Cygni profiles with absorption below the continuum were found in the Hα emission line for V1980 (also known as LkHα 321), DR Tau and AS 353 A. This pronounced absorption dip is indicative of the presence of a stronger mass outflow with low density and is usually found among objects with high accretion rates.

More specifically, type III P Cygni profiles (see figure 4.9) are present as well in CI Tau, DF Tau, DG Tau, DI Cep, DL Tau, DS Tau, EH Cep and RY Tau. This line profile shows a significant blueward emission at the left of the absorption dip, which can be found above or below the continuum (Mihalas

[3] http://cars9.uchicago.edu/software/python/mpfit.html

and Conti, 1980). Additionally, the profiles are a combination of blueshifted emission arising from the infall region, with Stark line broadening (Hartmann, 2009). The latest consists in the broadening of line emission wings for very optically thick lines as Hα (Muzerolle et al., 2001).

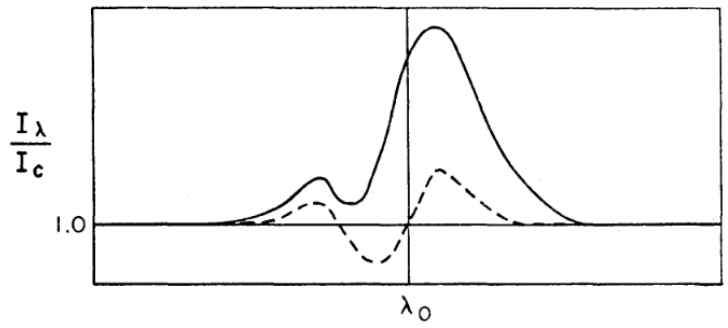

Figure 4.9: Illustration of Type III P Cygni profile by Mihalas and Conti (1980). The solid and dashed lines represent the two possible type III profiles, where the blueshifted absorption can be above or below the continuum.

Besides the presence of outflows, asymmetric line emission profiles are also the signature of accretion processes. As mentioned previously, the accreted material shocks onto the stellar surface along the magnetospheric lines. The accretion flow will achieve near free-fall velocities and the shocks will produce not only the hot continuum radiation, but also broad emission lines arising from the rapid infall of the gas (Hartmann, 2009).

In figure A.1 (in appendix), V649 Ori and UZ Tau E Hα profiles show redshifted absorptions, which could be related with magnetospheric accretion. Although confusing, it is possible to simultaneously detect both accretion and outflow signatures in Hα emission profiles. The dominance of accretion/outflow features will depend upon the excitation and optical properties of the line transition (Hartmann, 2009).

DR Tau is a very active CTTS with strong emissions, and is thought that its brightness is associated to an accretion rate increase, leading to a stronger hot continuum emission (Hartmann, 2009). It shows a P Cygni profile in the Hα emission line (see figure A.1b), probably formed almost entirely in the wind, contrasting with gaussian-like profiles as BP Tau, DQ Tau, LkHα 191, LkHα 330 and UY Aur, for instance, with no wind signatures in the line profile.

Additionally, DG Tau and AS 353A are known for being extremely active CTTS. They are characterized by exceptionally strong winds (evidenced here by their Hα profiles), spatially extended optical jets, strong veiling fluxes and considerable infrared excesses (Edwards et al., 1994).

Stochastic line profile variability should be taken into account. Also, Muzerolle et al. (2001) mentioned that depending on disk inclination the line flux can vary between a factor of 2 to 3. The flux is largest at low inclination angles (pole-on), and decreases with larger inclination (edge-on) as AA Tau (Bouvier et al., 2003), as occultation effects and redshifted absorption become significant. Consequently, the degree of profile asymmetry, peak velocity and presence of redshifted absorption can also be affected by disk inclination. Optical variability could also be explained by nonaxisymmetric accretion among CTTS (Bertout et al., 1988).

He I

Among the He I $\lambda5876$ and $\lambda6678$ emission lines observed (see figures A.2 and A.3 in appendix, respectively) and as mentioned previously, the presence of narrow and broad components in emission lines are indicative of magnetospheric accretion processes. Also, IPC profiles give estimates for free-falling velocities of the gas between $300-500km/s$ for both He I at $\lambda5876$ and $\lambda6678$. Unexpectedly, UZ Tau E is the only star which shows a P Cygni profile for He I $\lambda5876$ and RW Aur shows a blueshifted absorption dip for He I $\lambda6678$. For the latest feature, it could also depend on the position of the accretion column relatively to the observer. For this star, Petrov et al. (2001) suggests that the magnetosphere may be tilted relatively to it rotation axis, hence influencing the line emissions along time in the form of P Cygni or IPC profiles.

Velocity peaks

Figure 4.10 shows the distribution of emission peak velocities, of the sample of CTTS, for Hα $\lambda6563$, He I $\lambda5678$ and $\lambda6678$. Hα profiles have most of the velocity peaks between -50 to 50 km/s, but most of the cases are blueshifted. Conversely, for He I $\lambda5678$ and $\lambda6678$ the highest frequency of velocity peaks is redshifted, with values between 0 and 10 km/s.

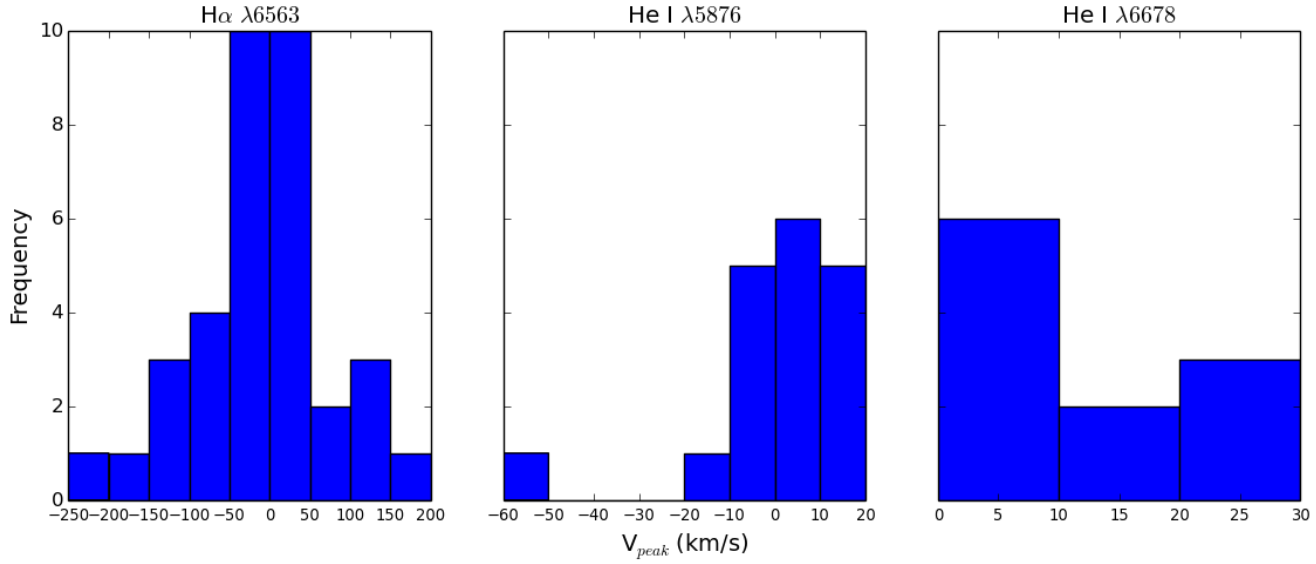

Figure 4.10: Distribution of emission peak velocities for Hα $\lambda6563$ (left), He I $\lambda5678$ (center) and $\lambda6678$ (right).

3GF routine

The 3GF script returns the fitted parameters for each gaussian, namely: central velocity (v_n), correspondent intensity (I_n) and standard deviation (σ_n), where n is the number of the adjusted gaussian.

To evaluate properly this set of computed parameters for each emission line, listed in tables 4.4, 4.5 and 4.6 (for Hα, He I $\lambda5876$ and $\lambda6678$, respectively), triple histograms were made and plotted in figure 4.12.

In the latest, each row of histograms (a, b and c) corresponds to Hα, He I $\lambda5876$ and $\lambda6678$ emission lines. The gaussian parameters determined for each element include the central velocity v (left column), intensity I (central column) and standard deviation σ (right column). The blue bars correspond to the 1^{st} gaussian (adjusted according with the peak intensity of the line), while the green correspond to the 2^{nd} gaussian (fits the line wings) and the red stands for the 3^{rd} one (fits the absorption features, if any).

From the last figure, we may observe that the fitted central velocities (left column) are mainly blueshifted for Hα, within the range of $[-100, 0]$ km/s. In contrast, for He I $\lambda5876$ and $\lambda6678$, the velocities for the two first gaussians are redshifted between $[0, 50]$ km/s. When looking at table 4.4 for Hα, an outlier (discarded in the histogram) is present in v_3 column for UY Aur, with an astonishing value of 1136.35 km/s and a null value for σ_3. In the corresponding figure A.1q, the third gaussian was not fitted due to the inexistence of absorptions features. Although 3GF fitted a extremely high central velocity, the gaussian was suppressed by the null standard deviation value.

Concerning the intensities (central column), it is possible to confirm that the script is working properly since the negative gaussians always present negative intensities (red bars), while the remaining ones present positive values. Additionally, assuming the absolute value for all intensities, Hα shows the highest intensities ($[0, 5]$), followed by He I $\lambda5876$ ($[0; 0.5]$) and He I $\lambda6678$ ($[0; 0.4]$).

Regarding the standard deviations (right column), they are associated to the aperture of the gaussian, namely the full width at half maximum (FWHM) of the peak according to $FWHM = 2\sqrt{2\ln 2}\sigma \approx 2.35482\sigma$ [4]. For Hα and He I $\lambda5876$ the highest dispersions are always for the second gaussian (green bars), which adjusts the wings of the emission line ($[100, 200]$ and $[100, 120]$ km/s, respectively). For He I $\lambda6678$, because the emission component is narrower than the absorption feature, the σ values are higher for the third gaussian ($[80, 100]$ km/s). As expected, Hα has the highest standard deviations due to its broad line emission. Clearly, He I $\lambda5876$ has a stronger emission than $\lambda6678$, and the latest seems to have broader absorption dips ranging until 180 km/s.

For Hα were observed typical outflow signatures, namely central blueshifted velocities (mainly between -100 and 0 km/s), asymmetric profiles (due to the presence of blueward absorption dips), high intensities and broad line wings confirmed by high σ values. Muzerolle et al. (1998b) suggests that blueward asymmetry, large line width, central or slightly blueshifted peak, are typical signatures of magnetospheric infall, which is in agreement with what was previously observed.

In contrast, He I although not so intense as Hα, shows mostly redshifted velocities in the range of 0 to 50 km/s, for both $\lambda5876$ and $\lambda6678$, and the line wings can extend almost to 140 and 100 km/s. The presence of relevant IPC profiles is characteristic of accretion processes as mentioned before. The latest profiles have central velocities that can reach 350 km/s and standard deviations near 180 km/s.

The origin of Hα line may be misleading, since it is an opaque line and its emission may have different origins. On the other hand, the opacity of He I is much less and the emitting components can give proper

[4] http://mathworld.wolfram.com/GaussianFunction.html

hints regarding its origin. As mentioned previously, He I narrow component is though to have its origin in a post-shock region on the star. Hence, the narrow component of both He I $\lambda 5876$ and $\lambda 6678$ is probably emitted in the same region. To confirm this hypothesis, the correlation between the fitted velocities for the first gaussian (v_1) for He I $\lambda 5876$ and $\lambda 6678$ was plotted in figure 4.11. In the latest, we can see that there is a correlation between the velocities fitted for the narrow component, suggesting that both emission lines must have their origin in a post-shock region.

It should be mentioned that, for this last correlation, DL Tau was discarded since it was an outlier in the sample (see figure A.2o). Because the latest star shows a more irregular profile, 3GF found the need to fit a first gaussian (black line) with a central velocity of $-42.62\ km/s$, for He I $\lambda 5876$, in order to match the given spectrum. This is one of the flaws of the routine that should be improved in future work.

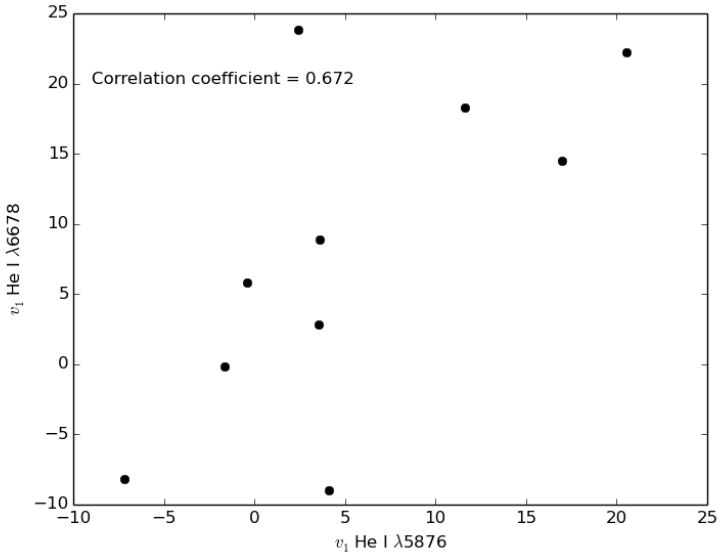

Figure 4.11: Correlation of the fitted velocities for the first gaussian (v_1) for He I $\lambda 5876$ and $\lambda 6678$.

In He I $\lambda 5876$ emission lines analysed, an atmospheric absorption line (also known as telluric absorption) was observed at the left of the emission peak near 5875.6Å for several stars of the sample. At first, it was thought that could be an absorption with origin in the molecular cloud, but since this feature was observed in stars of different constellations (namely the constellation of Cepheus, Aries and Taurus), that possibility was discarded. This absorption was a problem along the fitting, because whenever it was present, 3GF would fit a negative intensity gaussian unless additional constraints were introduced according to each spectrum.

As expected, the 3GF routine fitted more easily gaussian-like emission profiles. The remaining ones, with more complex and asymmetric profiles, were more difficult to adjust and more constrains were add. Nevertheless, the routine should be polished so it can fit more accurately narrow and broad components, as seen for He I.

Table 4.4: Determined parameters with the triple gaussian fitting for Hα emission line. Columns 2 to 4, 5 to 7 and 8 to 10 correspond to the 1^{st}, 2^{nd} and 3^{rd} fitted gaussians, respectively, with the determined parameters for each one: central velocity (v_n), correspondent intensity (I_n) and standard deviation (σ_n). In the last column are show the velocity peaks for the Hα in each star.

Object	1^{st} Gaussian			2^{nd} Gaussian			3^{rd} Gaussian			V_{peak}
	v_1 (km/s)	I_1	σ_1 (km/s)	v_2 (km/s)	I_2	σ_2 (km/s)	v_3 (km/s)	I_3	σ_3 (km/s)	(km/s)
AA Ori	6.47	8.55	102.77	−107.57	0.50	132.86	−5.24	−8.00	85.79	104.21
AA Tau	−8.84	4.13	106.40	142.73	0.16	182.72	−6.86	−4.00	39.02	−92.51
AS 353A	47.53	20.35	134.21	−104.47	1.50	400.07	−5.19	−10.00	178.64	32.28
BM And	−1.89	8.70	130.09	−119.85	0.50	91.36	−10.60	−8.00	58.45	−130.74
BP Tau	−13.31	10.41	82.72	−101.99	1.01	258.03	−380.66	−0.29	101.83	−15.44
BZ Sgr	−57.83	9.57	194.10	−15.93	0.10	274.08	−56.59	−9.00	65.03	−208.51
CI Tau	41.79	12.20	124.29	234.18	1.00	319.76	−13.10	−12.00	40.30	83.70
CW Tau	−2.39	15.55	145.53	17.63	0.80	296.92	−17.66	−15.00	55.45	105.13
DF Tau	−0.92	13.50	61.05	100.11	1.50	193.88	−55.31	−8.00	28.21	5.72
DG Tau	35.37	15.00	114.20	−9.60	1.00	288.67	−52.72	−8.00	73.92	24.99
DI Cep	−6.10	11.81	134.34	−45.92	1.00	228.40	−200.16	−4.42	56.74	−60.08
DK Tau	−68.26	10.73	99.10	−10.06	1.00	182.72	−44.19	−10.00	39.01	−123.67
DL Ori	11.85	21.84	111.88	7.39	0.35	711.25	172.69	−2.84	38.63	63.69
DL Tau	−9.66	15.00	143.34	−8.79	0.50	429.60	−115.33	−11.56	35.27	−14.85
DQ Tau	15.39	12.89	70.42	−35.17	1.00	182.72	60.73	−3.70	38.76	−6.50
DR Tau	146.37	12.68	78.21	51.37	1.50	380.07	−71.18	−1.90	102.07	143.34
DS Tau	−20.85	11.62	101.23	−12.64	0.84	319.25	−87.34	−7.12	49.49	5.39
EH Cep	22.71	3.40	94.23	−30.63	0.25	271.32	−30.75	−2.50	46.19	43.37
GK Tau	−29.45	5.79	92.54	66.71	0.25	182.72	−34.95	−5.46	41.83	37.64
GM Aur	3.17	11.17	138.44	159.77	0.37	365.44	7.29	−5.84	22.79	−51.88
LkHα 191	−7.31	3.50	51.52	10.59	0.72	140.30	82.42	−0.10	319.76	−12.46
LkHα 330	−1.51	2.74	96.12	−97.13	0.00	243.26	245.34	−0.10	0.00	−26.16
RW Aur	−33.05	9.43	155.65	59.93	1.00	228.40	−48.90	−9.00	62.71	−182.12
RY Tau	38.31	1.42	147.19	−56.91	0.50	160.75	−74.56	−1.03	54.99	17.69
T Tau	4.18	14.71	90.04	−7.37	0.24	406.15	132.42	−1.91	27.50	34.54
UY Aur	−35.52	10.13	89.84	36.54	1.15	192.16	1136.35	−0.10	0.00	−2.46
UZ Tau E	15.34	7.71	98.45	−12.52	0.00	324.93	54.73	−2.54	23.51	−14.19
V1079 Tau	−2.23	9.97	66.15	−97.68	0.60	137.04	−1.53	−10.00	48.46	−64.62
V1305 Ori	−27.31	6.20	128.88	−52.63	1.00	133.45	−103.48	−1.60	123.79	−22.03
V1980 Cyg	44.78	5.42	96.91	−51.70	0.57	339.48	−262.44	−1.23	84.32	12.54
V466 Ori	−15.38	3.40	147.87	−98.18	0.00	326.28	−134.88	−1.01	22.84	−7.15
V625 Ori	198.53	3.68	59.67	47.43	3.53	205.56	−14.18	−2.38	31.37	184.39
V649 Ori	19.20	6.55	117.50	−18.23	0.50	182.72	63.04	−2.13	41.49	−6.68
V828 Cas	−33.54	2.68	114.20	55.50	0.50	164.30	−32.38	−2.52	50.02	−122.11
WY Ari	−27.41	21.73	116.14	151.27	6.00	65.74	−60.09	−5.31	36.27	11.59

Table 4.5: Determined parameters with the triple gaussian fitting for He I $\lambda 5876$ emission line. Columns 2 to 4, 5 to 7 and 8 to 10 correspond to the 1^{st}, 2^{nd} and 3^{rd} fitted gaussians, respectively, with the determined parameters for each one: central velocity (v_n), correspondent intensity (I_n) and standard deviation (σ_n). In the last column are show the velocity peaks for the He I $\lambda 5876$ in each star.

Object	1^{st} Gaussian			2^{nd} Gaussian			3^{rd} Gaussian			V_{peak}
	v_1 (km/s)	I_1	σ_1 (km/s)	v_2 (km/s)	I_2	σ_2 (km/s)	v_3 (km/s)	I_3	σ_3 (km/s)	(km/s)
AA Tau	4.80	0.30	10.61	11.36	0.23	33.34	46.65	−0.09	3.14	3.21
AS 353A	−25.78	0.42	47.52	−56.31	0.10	76.53	−37.59	−0.24	25.51	−5.28
BP Tau	−0.38	1.18	21.44	4.33	0.07	59.81	−25.66	−0.36	10.20	−1.31
BZ Sgr	−84.88	0.31	112.94	−13.45	0.15	102.05	250.95	−0.20	102.05	−11.97
CI Tau	20.54	0.47	15.70	17.66	0.48	102.05	224.66	−0.11	51.02	17.94
CW Tau	−53.25	0.35	71.77	−83.04	0.05	119.66	227.92	−0.06	51.02	−57.53
DF Tau	16.98	2.22	15.50	35.18	0.56	43.14	90.08	−0.01	0.51	9.67
DG Tau	11.63	0.94	51.02	11.63	0.15	102.05	11.63	−0.05	5.10	11.63
DI Cep	14.33	0.35	51.02	−8.16	0.05	83.25	37.61	−0.10	7.65	17.35
DK Tau	−1.62	1.05	25.51	−29.12	0.20	76.53	−2.36	−0.20	25.51	−3.61
DL Ori	−4.84	0.68	36.31	26.65	0.10	112.15	247.77	−0.09	51.02	1.14
DL Tau	−42.62	1.32	76.53	13.54	0.37	127.56	−65.13	−0.95	47.78	−3.05
DR Tau	3.56	0.62	17.47	−9.66	0.71	85.15	146.59	−0.22	82.51	−0.66
DS Tau	3.63	1.83	24.28	44.53	0.20	51.02	−21.86	−0.85	13.53	4.92
RW Aur	4.12	0.73	31.26	−30.58	0.19	78.27	−23.37	−0.43	19.73	12.12
UY Tau	−7.18	1.04	24.79	1.21	0.14	51.02	−27.94	−0.50	17.73	1.00
UZ Tau E	5.37	1.00	14.29	19.59	0.10	51.02	−128.24	−0.14	51.02	0.87
WY Ari	2.40	1.13	49.08	17.43	0.14	118.46	−26.28	−0.50	22.93	11.53

Table 4.6: Determined parameters with the triple gaussian fitting for He I $\lambda 6678$ emission line. Columns 2 to 4, 5 to 7 and 8 to 10 correspond to the 1^{st}, 2^{nd} and 3^{rd} fitted gaussians, respectively, with the determined parameters for each one: central velocity (v_n), correspondent intensity (I_n) and standard deviation (σ_n). In the last column are show the velocity peaks for the He I $\lambda 6678$ in each star.

Object	1^{st} Gaussian			2^{nd} Gaussian			3^{rd} Gaussian			V_{peak}
	v_1 (km/s)	I_1	σ_1 (km/s)	v_2 (km/s)	I_2	σ_2 (km/s)	v_3 (km/s)	I_3	σ_3 (km/s)	(km/s)
BP Tau	5.83	0.43	9.94	13.12	0.11	22.45	-68.11	-0.01	2.24	4.31
CI Tau	22.26	0.40	7.34	2.57	0.14	89.78	335.92	-0.10	130.53	21.23
DF Tau	14.51	1.31	9.27	35.41	0.34	22.45	207.91	-0.08	89.78	12.96
DG Tau	18.29	0.30	34.40	-7.39	0.05	89.78	18.29	-0.10	34.40	15.06
DK Tau	-0.16	0.27	7.68	-21.97	0.05	54.19	175.99	-0.05	89.78	0.47
DL Tau	2.62	0.60	8.62	-17.54	0.29	96.82	-24.75	-0.10	35.15	4.90
DR Tau	2.84	0.50	11.01	3.49	0.23	78.14	149.43	-0.18	161.99	0.30
DS Tau	8.87	1.00	10.74	30.94	0.20	22.45	248.30	-0.02	89.78	8.49
RW Aur	-8.96	0.40	44.89	-67.58	0.10	70.44	-30.21	-0.35	22.45	21.01
UY Aur	-8.19	0.53	20.35	-11.72	0.04	44.89	-22.25	-0.35	16.69	4.85
WY Ari	23.86	0.28	11.61	10.56	0.05	47.45	235.94	-0.16	95.13	25.35

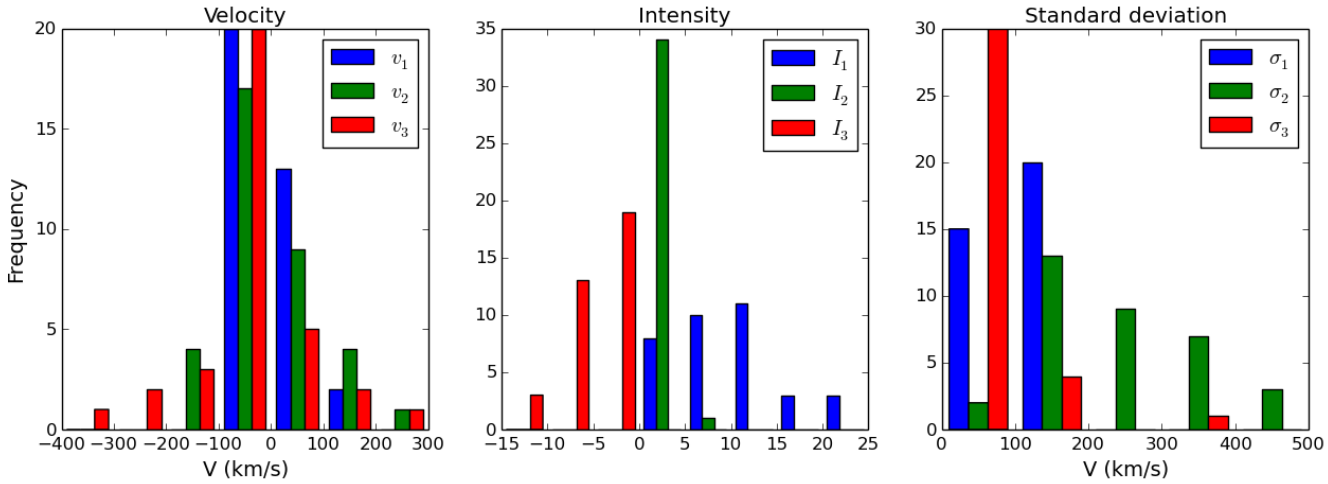

(a) Hα λ6563

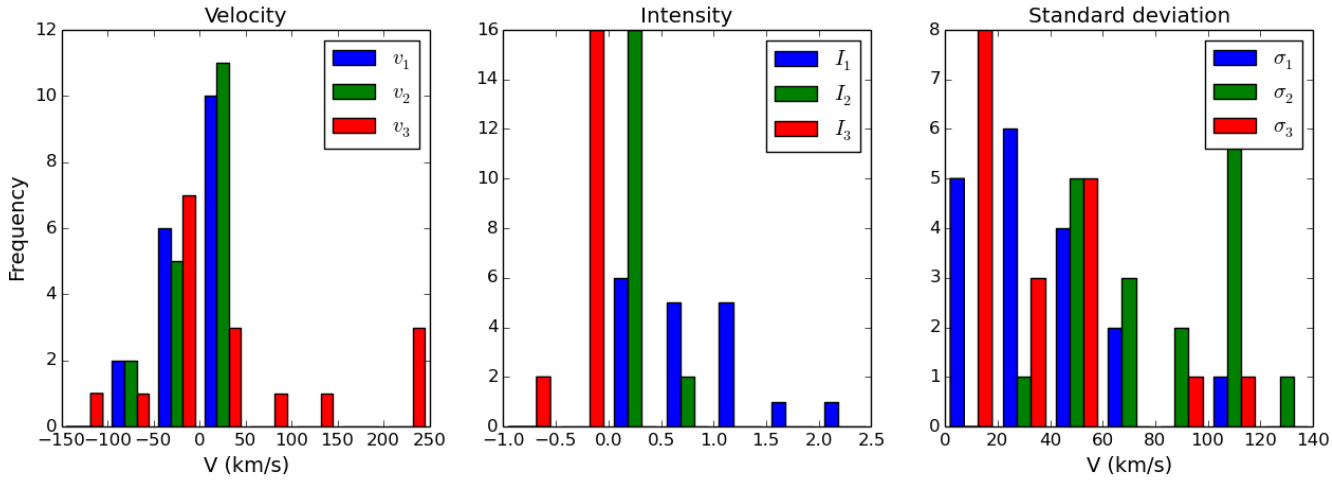

(b) He I λ5876

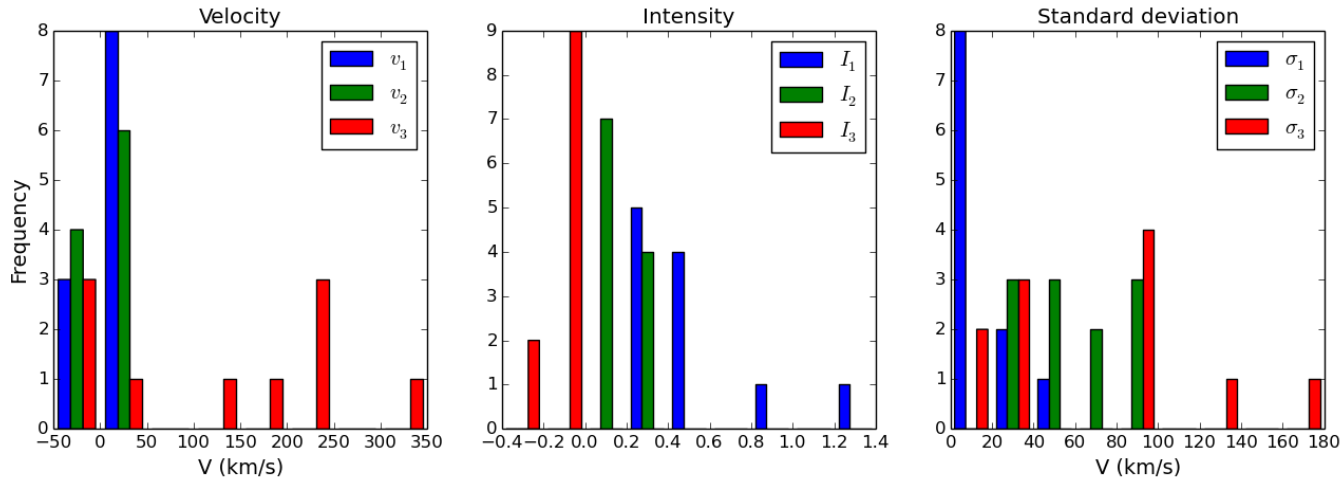

(c) He I λ6678

Figure 4.12: Histograms for the parameters for each one of the 3 gaussians adjusted determined by the triple gaussian fitting: central velocity (left), correspondent intensity (center) and standard deviation (right). Each row of histograms corresponds to Hα, He I λ5876 and λ6678, respectively.

Chapter 5

Modelling accretion and outflow regions

Models are useful to study the dynamics of stellar systems by gathering the effects of density, velocity, temperature and many other physical quantities. In the last years, numerical simulations of magnetized stellar winds have been developed in order to understand how young stars exchange angular momentum with their disks through the magnetic field (Bouvier et al., 2014).

Outflows have been studied theoretically through ideal steady or time-dependent magnetohydrodynamics (MHD). Firstly, steady models were developed by Parker (1963), Weber and Davis (1967) and Michel (1969), which considered a one-dimensional model with spherical symmetry. Later, Suess (1972) and Nerney and Suess (1975) developed the first two-dimensional axisymmetric model which describes, through a linearisation of the MHD equations, the interaction between magnetic fields and rotation in stellar winds.

Afterwards, Blandford and Payne (1982) showed that Keplerian accretion disks (if the poloidal fieldlines have an inclination of $i \leq 60^{\circ}$) could be responsible for jet acceleration. Furthermore, Low and Tsinganos (1986) and Tsinganos and Low (1989), in order to model the axisymmetric wind, introduced the meridionally self-similar exact MHD solutions with a variable polytropic index. In addition, Vlahakis and Tsinganos (1998) unified all cases of self-similar, jet/wind type exact MHD solutions.

Sauty and Tsinganos (1994) were able to determine self-consistently the shape of the fieldlines from the base of the outflow to infinity for nonpolytropic cases using self similarity. The authors suggested that as a young star rotates slower by losing angular momentum, the initial outflow in the form of a jet becomes progressively a conical expanding wind.

Observations suggest that there is variability within the outflows. For such matter, time-dependent models are useful in order to make a more accurate replication from the observations. Uchida and Shibata (1985) performed the first time-dependent simulations and showed that when the magnetic field of a vertical disk is twisted by the disk rotation, bipolar plasmas can be ejected through the torsional Alfvén waves generated.

Driving our attention to accretion models, these were initially developed by Lynden-Bell and Pringle

(1974). According to the authors, the luminosity of the accretion disk is given by

$$L_{\text{acc}} = GM_*\dot{M}/R_* \tag{5.1}$$

, where G is the gravitational constant, $\dot{M}$ is the accretion rate, M_* is the stellar mass, and R_* the stellar radius. By knowing M_*, R_*, L_* and the excess luminosity (*veiling*) from observations, it is possible to determine L_{acc} as well the accretion rate $\dot{M}$, which has been estimated by several authors varying from 10^{-9} to $10^{-6} M_\odot/yr$.

Later, Bertout et al. (1988) and Basri and Bertout (1989) applied, directly to TTS, the theory of accretion disks by assuming quasi-keplerian orbits for rotating gas that would reach the surface of the star and create a shock front in the equatorial region.

Models regarding magnetospheric accretion were firstly applied to neutron stars (Ghosh and Lamb, 1979) and latter to TTS. These models aim to explain CTTS low rotation velocities based on a more active interaction between the star and the disk through the magnetic field.

In order to combine accretion and stellar winds in TTS, Shu et al. (1994) developed a model in which stellar winds are accelerated by the magnetic field by its interaction with ionized gas in the accretion disk at a distance $r = R_X$ (see figure 5.1). The later depends not only in the magnetic field strength, but also in the accretion rate, mass and radius of the star. In the vicinity of R_X, closed magnetic field lines of the magnetosphere of the star ($r < R_X$) and open magnetic field lines of the disk ($r > R_X$) cross the circumstellar disk. Disk material falls on the stars along the closed lines while open lines are highways for ejected material.

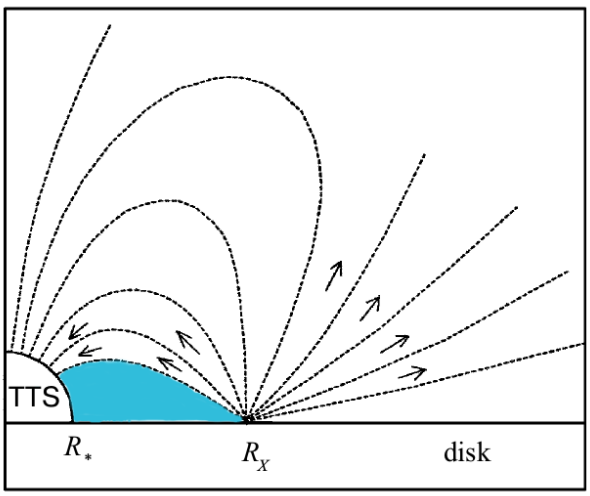

Figure 5.1: Direction of gas flows in a star-disk magnetic system according to the model developed by Shu et al. (1994). The blue region represents a magnetospheric region with closed field lines, where accretion is not verified.

5.1 ANALYTICAL MODEL

The main goal in this chapter is to model the structure of the magnetosphere of YSOs, where accretion and outflow mechanisms occur. The numerical simulations use as initial conditions the model developed by Sauty and Tsinganos (1994) (described in a following section), which was implemented in PLUTO[1] code by researchers from the Astronomical Observatory of Paris. In the mentioned simulations, as only as a code user, were only changed the multiplying factors of some main physical quantities.

Regarding the model used, Sauty and Tsinganos (1994) when considering a non polytropic heating and magnetic rotation forces, thermal pressure gradients are responsible for conducting the stellar outflows. One of the main advantages of implementing this model in numerical simulations is that it enables the study of time-dependent solutions both in accretion and outflow regions.

The solutions for this model can be reached by separating the variables of the spherical distance (R) and magnetic flux function (α) in a range of selected physical quantities. For such matter, the solutions may be classified as magnetic flux self-similar and consider the whole flow dynamics from the source to large distances. In order to easy construct analytical models and simplify numerical computations, self-similar models are useful scaling tools in which are considered certain variable dependences. One of the advantages, for instance, is that these models allow a reduction of the set of ideal MHD partial differential equations (PDE) to a smaller set of ordinary differential equations (ODE). By doing so, instead of dealing with PDEs with, at least, two independent variables and their derivatives, ODEs have only one independent variable.

Regarding the self-similarity method, it can be applied whether in time or space. A physical phenomenon is called temporarily self-similar if it can be reproduced at any time through a self-similar mechanism from a previous temporal state. When a physical phenomenon is called spatially self-similar it means that it can be reproduced everywhere in space through a spatial self-similar mechanism. Furthermore, spatial self-similarity is a method of nonlinear variable separation in the set of steady MHD equations, contributing to achieve analytical solutions (Tsinganos, 2007).

In self-similarity it is assumed that both the normalized cylindrical radius G and the Alfvén number M are functions of a single variable χ.

In one hand, if $\chi = \theta$, we obtain radially self-similar models with surfaces of constant poloidal Alfvén Mach number (the magnetic flux scales with a power of the spherical radius), as shown in figure (5.2a), which illustrates the radial self-similar character of the poloidal field lines resulting from assuming $\varpi = \varpi_a G(\theta)$ (Vlahakis and Tsinganos, 1998). These models are suitable for disk winds ejected from the external part of an accretion disk as in Blandford and Payne (1982) model.

On the other hand, when $\chi = r$, we achieve the meridionally self-similar models with spherical surfaces of constant poloidal Alfvén Mach number (the magnetic flux scales with the colatitude). This familly of

[1] http://plutocode.ph.unito.it/

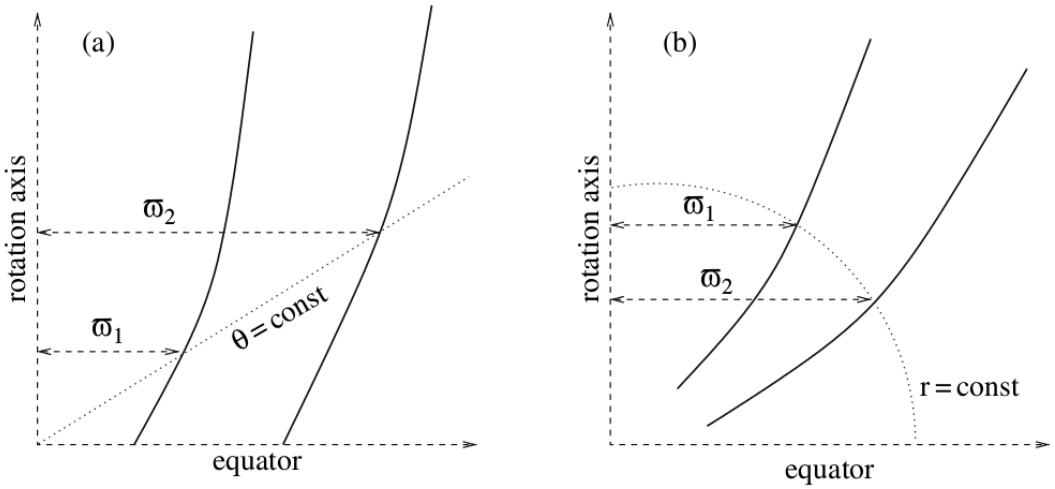

Figure 5.2: Illustration of the two possibilities of self-similar field line structure. The thick lines represent two random field lines. Plot (a) shows the radial self-similarity case, wherein the ratio of the cylindrical distances ϖ_1/ϖ_2 for the intersection of any poloidal field line with a cone is the same for any θ value. Plot (b) illustrates the case for meridional self-similarity , where the cylindrical distance ratio is the same for any spherical surface of constant radius r. For both cases, once we know one fieldline we are able to construct all the others (Tsinganos, 2007).

models includes not only the Parker (1963) model for the stellar wind as well the simple prescribed fieldline model of Tsinganos and Trussoni (1991). Figure (5.2b) represents the meridional self-similar models by assuming $\varpi = \varpi_a G(r)$ (Vlahakis and Tsinganos, 1998). As in Sauty and Tsinganos (1994), these models can be applied to the stellar part of ejection and/or the internal part of the accretion disk, including the study of physical properties of the outflow close to its rotation axis such as accelerated and collimated jets (Sauty et al., 1998; Tsinganos, 2007).

MHD equations for MHD outflows

A fundamental assumption in MHD is that the electromagnetic variations are non-relativistic or almost static, because the bulk speed of the flow is much less than the speed of light ($V_0 \ll c$), where $V_0 = L_0/t_0$ is the characteristic velocity of the plasma given by the ratio between the chacterictic length and time. This assumption will lead to four main consequences described below (Priest, 1984).

From the Maxwell equation we can write:

$$\nabla \times \mathbf{E} = -\frac{\partial \mathbf{B}}{\partial t} \rightarrow |\nabla \times \mathbf{E}| \approx \frac{E_0}{L_0}, \left|\frac{\partial \mathbf{B}}{\partial t}\right| \approx \frac{B_0}{t_0}, \tag{5.2}$$

where $\mathbf{E}$, E_0, $\mathbf{B}$ and B_0 represent the vectorial and characteristic electric and magnetic fields, respectively. Therefore:

$$\frac{E_0}{L_0} = \frac{B_0}{t_0} \Rightarrow \frac{E_0}{B_0} = \frac{L_0}{t_0} = V_0. \tag{5.3}$$

From the Ampère's law we may see that

$$\frac{\left|\frac{1}{c^2}\frac{\partial \mathbf{E}}{\partial t}\right|}{|\nabla \times \mathbf{B}|} \approx \frac{\frac{1}{c^2}\cdot\frac{E_0}{t_0}}{B_0/L_0} = \frac{V_0^2}{c^2} \ll 1. \tag{5.4}$$

Hence, if $V_0^2 \ll c^2$

$$|\nabla \times \mathbf{B}| \gg \left|\frac{1}{c^2}\frac{\partial \mathbf{E}}{\partial t}\right|, \tag{5.5}$$

is the MHD approximation for which the Ampére's law reduces to equation

$$\nabla \times \mathbf{B} = \mu_0 \mathbf{j}, \tag{5.6}$$

where μ_0 corresponds to the magnetic permeability and $\mathbf{j}$ to the current density. Equation 5.6 is the first consequence of assuming non-relativistic velocities for the plasma. Another consequence is that the term $\frac{1}{c^2}\frac{\partial \mathbf{E}}{\partial t}$ is negligible in the Ampére's law. The latest corresponds to the low frequency limit of the correspondent Maxwell equation:

$$\frac{V_0}{c} \ll 1 \Rightarrow \frac{L_0}{t_0 c} \ll 1 \Rightarrow \frac{1}{t_0} \ll \frac{c}{L_0} \Rightarrow \omega_0 \ll \frac{c}{L_0}, \tag{5.7}$$

where ω_0 is the characteristic frequency. The third consequence is the charge continuity equation achieved by the divergence of Ampére's law:

$$\begin{aligned} \nabla \times \mathbf{B} &= \mu_0 \mathbf{j} \\ \nabla \cdot (\nabla \times \mathbf{B}) &= 0 \\ \nabla \cdot (\mu_0 \mathbf{j}) &= 0 \\ \nabla \cdot \mathbf{j} &= 0, \end{aligned} \tag{5.8}$$

This last equation implies that local charge accumulations in time are negligible and the electric current flows in a closed circuit. The fourth an last consequence is that the ratio between electrostatic ($E_{\text{elec}} \sim \varepsilon_0 E^2$) and magnetic energy ($E_{\text{magn}} \sim B_0^2/\mu_0$) is much less than the unity:

$$\frac{E_{\text{elec}}}{E_{\text{magn}}} \approx \frac{\varepsilon_0 E_0^2 \mu_0}{B_0^2} \approx \mu_0 \varepsilon_0 \left(\frac{E_0}{B_0}\right)^2 \approx \frac{V_0^2}{c^2} \ll 1, \tag{5.9}$$

where ϵ_0 is the permittivity.

When dealing with MHD is fundamental to state the ideal MHD equations, which describe the hydrodynamic interaction in typical astrophysical plasmas (fully ionized), such as those encountered in stellar atmospheres and star forming regions. For the steady case we have:

$$\nabla \cdot \mathbf{B} = 0, \tag{5.10}$$

$$\nabla \cdot (\rho \mathbf{V}) = 0, \tag{5.11}$$

$$\nabla \times (\mathbf{V} \times \mathbf{B}) = 0 \Leftrightarrow \mathbf{V} \times \mathbf{B} = \nabla \Phi, \tag{5.12}$$

$$\rho(\mathbf{V} \cdot \nabla)\mathbf{V} = -\nabla P + \frac{1}{4\pi}(\nabla \times \mathbf{B}) \times \mathbf{B} - \frac{\rho G M}{r^2} e_r, \tag{5.13}$$

where $\mathbf{V}$ is the bulk flow speed, $\mathbf{B}$ the magnetic field, ρ the density, P the pressure, M the mass of the central object, G is the gravitational constant, r the spherical distance from the central object and Φ the electrical potential. Magnetic flux and mass flux conservation are represented in equations (5.10) and (5.11), respectively. The induction law for a high conductive plasma is expressed in equation (5.12), while equation (5.13) represents the motion equation, which expresses the total momentum balance along the flow.

The above set of MHD equations described for ideal plasmas takes into account that the electrical conductivity is high such that the plasma behaves like a superconductor and the viscosity (mainly from the ions) is negligible for the diluted astrophysical gases ($\mu \approx 10^{-16} T^{5/2}$ g/cm sec), which cannot cover the angular momentum transfer in circumstellar disks (Tsinganos, 2007), therefore we need equation (5.14) to complement it.

Sauty and Tsinganos (1994) mention that a heating function is needed to describe how a wind flows out from a gravitational well of a central object. Therefore, from energy conservation, q defines the volumetric rate of the thermal energy input

$$q = \rho \mathbf{V} \cdot \left[\nabla h - \frac{\nabla P}{\rho} \right], \tag{5.14}$$

where h is the specific enthalpy. This thermodynamic variable represents the heat reservoir from which the gas in the wind absorbs thermal energy and converts it to kinetic energy. According to the authors, if q assumes a positive/negative value, we are in the presence of a heating/cooling function.

The MHD equations of Sauty and Tsinganos (1994) model were solved without constraining any polytropic relations and the volumetric rate of thermal energy is defined as a function of the spherical radius R and the colatitude θ, $q(R, \theta)$. By considering an axisymmetric system ($\frac{\partial}{\partial \varphi} = 0$), there will be a reduction of equations (5.10) to (5.14) regarding conserved quantities along each magnetic field line. According to Tsinganos (1982), the general properties of systems with an ignorable coordinate will lead to a set of free integrals, which are functions that remain constant on the magnetic surfaces generated by the revolution around the magnetic/flow symmetry axis of the system of a poloidal magnetic line $A(r, \theta) = constant$, where A is the magnetic flux function. When considering the surface of a flux tube with $A = const.$,

some physical quantities will remain invariant such as: the ratio between mass and magnetic flux $\Psi_A(A)$, the total specific angular momentum carried by the flow and the magnetic field $L(A)$ and the angular velocity of each streamline at the base of the flow $\Omega(A)$ (Sauty et al., 1998).

In Sauty and Tsinganos (1994) meridionally ($\theta-$) self-similar model, all quantities are normalized to the Alfvén surface (with radius r_*) along the rotation axis, by using spherical coordinates (r, θ, φ), where r, θ and φ correspond to the radial, polar and azimuthal/toroidal components, due to the spherical symmetry of the gravitational field. Cylindrical coordinates are also used (ϖ, φ, z), where ϖ is the radial distance, φ the azimuth angle followed by height z. This coordinate system can be more handy when dealing with collimated flows along the z axis. To convert coordinates from one system to another it will be considered $\varphi = r\sin\theta$ and $z = r\cos\theta$.

Taking all into account and assuming a steady and an axisymmetric system, the poloidal magnetic field ($\mathbf{B}_p$) is defined as

$$\mathbf{B}_p = \nabla \times \left(\frac{A}{r\sin\theta} e_\varphi\right) = \frac{\nabla A}{\varpi} \times e_\varphi, \tag{5.15}$$

where A refers to the magnetic flux function. In order to define a poloidal mass flux, a stream function Ψ is introduced in the following expression

$$4\pi\rho\mathbf{V}_p = \nabla \times \left(\frac{\Psi}{r\sin\theta} e_\varphi\right) = \frac{\nabla\Psi}{\varpi} \times e_\varphi. \tag{5.16}$$

As a result of axisymmetry and equations (5.10) to (5.14), Ψ is constant on surfaces of constant A on which the corresponding streamlines and fieldlines are *roped* (Sauty and Tsinganos, 1994). Hence, when considering the velocity and magnetic field poloidal components, they will be parallel to each other and the poloidal velocity can be expressed as

$$\mathbf{V}_p = \frac{\Psi_A}{4\pi\rho}\mathbf{B}_p, \tag{5.17}$$

where the lower indexes A and p denote a derivative with respect to A ($\Psi_A = \frac{d\Psi}{dA}$) and poloidal component, respectively. Due to the presence of an electrical potential Φ, when considering a rotating wind, the total velocity $\mathbf{V}$ and magnetic field $\mathbf{B}$ are not aligned. In addition, each surface of constant magnetic flux function is a surface of constant electrical potential ($\Phi = \Phi(A)$). From equation (5.12), the toroidal component of the frozen flux condition will lead to the angular speed equation (Ω)

$$\Omega(A) = \Phi_A = \frac{1}{\varpi}\left(V_\varphi - \frac{\Psi_A B_\varphi}{4\pi\rho}\right). \tag{5.18}$$

Φ_A is denoted by Ω because it has the dimensions of an angular speed. Equation (5.18) is also defined as the isorotation law, since at the footpoints of each magnetic field line on the disk or the star where it is verified a magnetic field dominance, their angular speed its the same as Ω.

By integrating the momentum equation in the azimuthal direction, we obtain another free integral $L(A)$, corresponding to the total angular momentum of the system fluid plus field,

$$L(A) = \varpi \left(V_\varphi - \frac{B_\varphi}{\Psi_A} \right). \tag{5.19}$$

The ratio of the poloidal velocity to the characteristic poloidal Alfvén velocity can be written using the poloidal Alfvén number (M)

$$M^2 = 4\pi\rho \frac{\mathbf{V}_p^2}{\mathbf{B}_p^2} = \frac{\Psi_A^2}{4\pi\rho}. \tag{5.20}$$

When the density equals the Alfvén density (ρ_*), it means that the equations have a singularity at the Alfvén point and we may write from equation (5.20)

$$M^2 = 1 \Rightarrow B_*^2 = \pi\rho_* V_*^2, \tag{5.21}$$

where B_* and V_* are, respectively, the magnetic field and velocity at the Alfvén surface which is equivalent to a sphere of radius r_*. Hence, the latest radius is defined as the Alfvén radius, where the magnetic energy density equals the kinematic energy density, or bulk velocity equals the Alfvén velocity (Belenkaya et al., 2015).

Sauty and Tsinganos (1994) mention that the two free integrals of L and Ω need to be related in order to *impose regularity*. For such matter, the Alfvénic cylindrical radius (ϖ_a) is introduced in function of A:

$$\varpi^2|_{M=1} = r^2 \sin^2\theta|_{M=1} = \varpi_a^2(A) = \frac{L(A)}{\Omega(A)}. \tag{5.22}$$

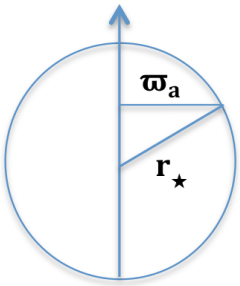

Figure 5.3: Representation of the Alfvénic cylindrical radius ϖ_a in a Alfvén surface of radius r_*. Picture courtesy: Véronique Cayatte.

Dimensionless variables

The following dimensionless variables (Weber and Davis, 1967; Sakurai, 1985) will be useful to simplify the analysis of the present model:

$$R = \frac{r}{r_*}, \qquad \frac{B_*}{4\pi\rho_*} = V_*^2, \qquad A = \frac{r_*^2 B_*}{2}\alpha(R,\theta), \tag{5.23}$$

where α is a dimensionless magnetic flux function. The Alfvén surface will be assumed as spherical, such that the Alvén number $M(R, A)$ will only depend on the spherical radius (also named dimensionless radial distance) R rather than a certain fieldline. Sauty and Tsinganos (1994) expect that this assumption will be more suitable when considering regions around the axis of a jet, because the flow has an approximate spherical Alfvén surface and in the disk-wind region the Alfvén surface may be more flexible to deal with any other model-dependent shape:

$$M(R, A) = M(R). \tag{5.24}$$

By assuming a spherical Alfvén surface, the density will take a separable form as $\rho = \rho(R)\rho_a(\alpha)$ and only the first order term of $\rho_a(\alpha)$ will be expanded in α as $\rho_a(\alpha) = \rho_*(1 + \delta\alpha)$, where δ describes the deviations from a spherically symmetric density:

$$\alpha = \frac{R^2}{G^2}\sin^2\theta = \left(\frac{\varpi_a}{r_*}\right)^2. \tag{5.25}$$

This is one of the ways to expand, in the magnetic flux α, the gravitational term in equations (5.13). Therefore, when considering the Alfvén number and the magnetic flux function, the density may be written as:

$$\rho(R, \alpha) = \frac{\rho_*}{M^2(R)(1 + \delta\alpha)}. \tag{5.26}$$

The dependence of the magnetic flux function on R and θ, $\alpha(R, \theta)$ gives the form of the magnetosphere. Whenever we have a region of compact closed fieldlines at the equator by a region of open fieldlines, α_{out} will be defined as the dimensionless magnetic flux for the last fieldline connected to the star, which corresponds to the last fieldline of the stellar jet. Hence, at $r = r_*$ the open fieldlines may extend up to an angle of θ_{out}. In this magnetospheric region with closed field lines represented in figure 5.1 in blue, the material is "frozen" and accretion does not occur. This region will be mention hereafter as dead zone.

In order to measure the cylindrical distance to the polar axis of a flux tube limited by the magnetic field line α, the normalized cylindrical radius is introduced:

$$G(R) = \frac{\varpi}{\varpi_a}, \tag{5.27}$$

where $\varpi(R, \alpha) = \varpi_a(\alpha)G(R)$ and $\varpi(\alpha) = r_*\sqrt{\alpha}$. When considering $G^2(R)$, it represents the cylindrical cross section of a flux tube, $S(R)$, normalized to its cross section at the Alvén point, S_a:

$$\frac{S}{S_a} = \frac{\varpi^2}{\varpi_a^2} = G^2(R) \tag{5.28}$$

Another important equation considered in Sauty and Tsinganos (1994) model is the logarithmic expansion factor $F(R)$, which measures the angle that the projection of a fieldline makes on the poloidal plane

with the radial direction:

$$F(R) = \frac{\partial \ln \alpha(R,\theta)}{\partial \ln R} = 2\left(1 - \frac{d\ln G}{d\ln R}\right). \tag{5.29}$$

For instance, when $F = 2$ the magnetic fieldlines will have a cylindrical shape, while $F = 0$ will correspond to radial fieldlines.

Mass loss rate

To derive a mass loss rate $\dot{M}$, first we need to take into account the free function $\Psi_A(\alpha)$ (which considers the Alfvén density as mention previously):

$$\Psi_A(\alpha) = \frac{4\pi\rho_* V_*}{B_*}\sqrt{1+\delta\alpha}. \tag{5.30}$$

Then, the poloidal mass flux can be expressed according to the stream function Ψ as

$$\Psi = 2\pi\rho_* r_*^2 V_* \int_0^\alpha \sqrt{1+\delta\alpha'}d\alpha', \tag{5.31}$$

where the mass is a conserved quantity. So, for each hemisphere of a stellar object, the derived mass loss rate is given by

$$\dot{M} = \int\int_S \rho \mathbf{V}_p \cdot \mathbf{dS} = \frac{\Psi_{\text{out}}}{2} = \pi\rho_* r_*^2 V_* \int_0^{\alpha_{\text{out}}} \sqrt{1+\delta\alpha'}d\alpha', \tag{5.32}$$

where $\Psi_{\text{out}} = \Psi(\alpha_{\text{out}})$. Integrating the previous expression, the mass loss rate can be written as

$$\dot{M} = \pi\rho_* r_*^2 V_* \frac{2}{3\delta}\left[(1+\delta\alpha)^{3/2} - 1\right], \tag{5.33}$$

for $\delta \neq 0$.

Regarding, for instance, magnetic fieldlines that are disconnected from the star (lines with $\alpha > \alpha_{\text{out}}$ that could be connected to a circumstellar disk) the previous set of equations remains valid.

In addition to all these equations, the total angular momentum per unit mass (L) and the angular velocity of the corotating system (Ω) given by equations (5.19) and (5.18) respectively, can be rewritten in function of α as

$$L(\alpha) = \lambda r_* V_* \frac{\alpha}{\sqrt{1+\delta\alpha}}, \tag{5.34}$$

$$\Omega(\alpha) = \frac{\lambda V_*}{r_*}\frac{1}{\sqrt{1+\delta\alpha}}, \tag{5.35}$$

where the parameter λ describes the strength of the magnetic torque at r_*.

Velocity and magnetic fields

The velocity and magnetic field components can be expressed in terms of unknown functions of R:

$$V_r = V_* \frac{M^2(R)}{G^2(R)} \frac{\cos\theta}{\sqrt{1+\delta\alpha(R,\theta)}}, \tag{5.36}$$

$$V_\theta = -V_* \frac{M^2(R)}{G^2(R)} \frac{F(R)}{2} \frac{\sin\theta}{\sqrt{1+\delta\alpha(R,\theta)}}, \tag{5.37}$$

$$V_\varphi = V_* \frac{\lambda}{G^2(R)} \frac{G^2(R)-M^2(R)}{1-M^2(R)} \frac{R\sin\theta}{\sqrt{1+\delta\alpha(R,\theta)}}, \tag{5.38}$$

$$B_r = B_* \frac{1}{G^2(R)} \cos\theta, \tag{5.39}$$

$$B_\theta = -B_* \frac{1}{G^2(R)} \frac{F(R)}{2} \sin\theta, \tag{5.40}$$

$$B_\varphi = -B_* \frac{\lambda}{G^2(R)} \frac{1-G^2(R)}{1-M^2(R)} R\sin\theta. \tag{5.41}$$

Pressure and gravitational potential

An equation for the pressure will be obtained once again through a first order expansion in terms of α, such that is consistent with the motion equation given by (5.13)

$$P(R,\alpha) = \frac{1}{2}\rho_* V_*^2 \Pi(R)\left[1+\kappa\alpha\right], \tag{5.42}$$

where $\Pi(R)$ is the dimensionless pressure and κ is a parameter that controls the deviations from the spherically symmetric pressure configuration. In the present model this variable will be assumed with a constant value, which means that the effective polytropic index γ will be the same function of R on each streamline.

Another dimensionless variable to take into account is the strength of the gravitational potential ν from which the wind escapes and is given by the ratio between the escape velocity at the Alfvén surface and

the polar velocity there:

$$\nu = \frac{V_{\text{esc}}}{V_*} = \sqrt{\frac{2GM}{r_* V_*^2}}. \tag{5.43}$$

Finally, the gravitational potential can be expressed by

$$U = \frac{GM}{r} = \frac{1}{2} V_*^2 \frac{\nu^2}{R}. \tag{5.44}$$

5.2 ADAPTING AN MHD OUTFLOW MODEL TO AN ACCRETION MODEL

The previous analytical model was conceived to simulate outflow mechanisms in YSOs, namely jets and stellar winds. In order to simulate accretion processes, we needed to reverse the sign of the radial component of the poloidal velocity V_r expressed by equation (5.36). By doing so, we get the initial conditions such that accretion mechanisms in the magnetosphere are included in PLUTO simulations. Observing figure 5.4, the V_p sign inversion inside the magnetosphere was accomplished for Test001_04 (for example), were negative velocity values (in blue) are present inside the magnetospheric region.

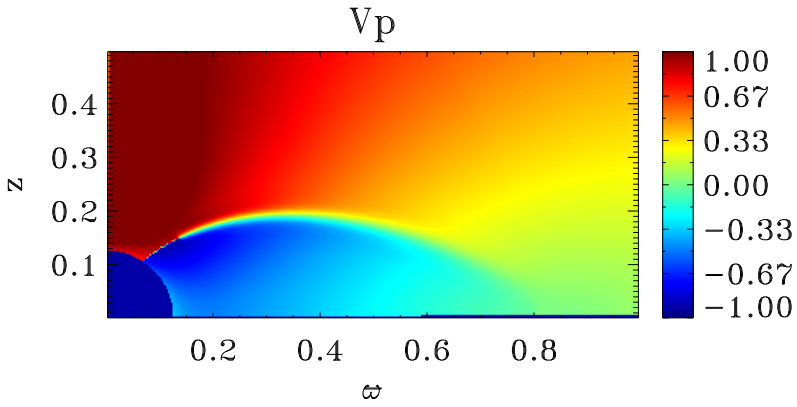

Figure 5.4: Representation of the poloidal velocity inversion in the initial moments ($t = 0.5$) of Test001_04 with PLUTO simulations. The blue region represents negatives velocities where accretion is expected to take place.

In addition, the heating function was adapted two times after some tests. In the first alteration (mentioned hereafter as new cooling function), the volumetric rate of thermal energy (q) was reversed with the same multiplying factors of V_r, so it would include negative values in the analytical dead zone. The second alteration (hereafter 2^{nd} new cooling and detailed in the following subsection), takes into account a vectorial shift between the simulated results and the analytical solution, since the heating function is in fact the heat flux and is moving with the flow.

Heating source

By integrating the equation of motion (5.13) along each streamline or fieldline and combining with equation (5.14) we have along the flow

$$\rho \mathbf{V} \cdot \nabla E = q, \tag{5.45}$$

where E denotes the sum of kinetic, thermal, gravitational and Poynting energy flux densities,

$$E \equiv \frac{1}{2}V_p^2 + \frac{1}{2}V_\varphi^2 + h - \frac{GM}{r} - \frac{\Omega}{\Psi_A}\varpi B_\varphi. \tag{5.46}$$

The Poynting energy flux is responsible for accelerating the outflow in the absence of thermal gas pressure (Hartmann, 2009). Due to the heating source q, E is not conserved along a fieldline. Nevertheless, it is possible to express the conserved quantity as

$$E - \int_{s_0}^{s} \frac{q(s,A)}{\rho(s,A)V_p(s,A)} ds = F(A), \tag{5.47}$$

where $F(A)$ is the generalized classical Bernoulli integral and s is the path length along a fieldline of $A = const$. The volumetric rate of thermal energy q, can be written in the vectorial form as

$$\vec{q} = q_r \vec{e_r} + q_\theta \vec{e_\theta}. \tag{5.48}$$

Then, q is normalized by the poloidal velocity V_p giving

$$\frac{q}{V_p} = \frac{q_r}{V_r} = \frac{q_\theta}{V_\theta}, \tag{5.49}$$

where V_p is given by $V_p = (V_r^2 + V_\theta^2)^{1/2}$.

It should be mentioned that simulated results $\vec{V_p} = V_r\vec{e_r} + V_\theta\vec{e_\theta}$ may differ from the ones of the analytical solution $\vec{V_{pAns}} = V_{rAns}\vec{e_r} + V_{\theta Ans}\vec{e_\theta}$ (see figure 5.5). To consider such shifts in the mentioned 2^{nd} new cooling function, the volumetric rate of thermal energy q along the fieldline was normalized with the poloidal velocity given by the analytical solution:

$$\begin{aligned} q = \frac{\vec{q}_{Ans}}{V_{pAns}} \cdot \vec{V_p} &= \frac{q_{Ans}\vec{V}_{pAns}}{V_{pAns}^2} \cdot \vec{V_p} \\ &= \frac{q_{Ans}}{V_{pAns}^2}[V_{rAns}\vec{e_r} + V_{\theta Ans}\vec{e_\theta}] \cdot [V_r\vec{e_r} + V_\theta\vec{e_\theta}] \\ &= \frac{q_{Ans}}{V_{pAns}^2}[V_{rAns}V_r + V_{\theta Ans}V_\theta]. \end{aligned} \tag{5.50}$$

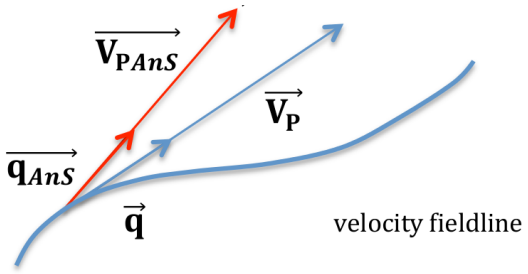

Figure 5.5: Representation of the poloidal velocity $\vec{V}_p$ and the volumetric rate of thermal energy $\vec{q}$ vectors for the analytical solution (*Ans* index and red vectors) and for the simulated results (blue vectors). The curvy blue line represents a velocity fieldline. Picture courtesy: Véronique Cayatte.

5.3 PLUTO SIMULATIONS

The analytical model described is already coded in PLUTO. The latest is a numerical code directed for astrophysical simulations and is able to compute hypersonic flows from 1 to 3 spatial dimensions in different coordinate systems. Besides, different hydrodynamic modules and algorithms are available for the user including Newtonian, relativistic, MHD or relativistic MHD fluids (Mignone et al., 2007).

The challenge is to "play" with the physical quantities involved and try reproduce the observations made so far regarding accretion and outflow mechanisms which occur in YSOs. Through the simulations will be increased some of the main physical quantities (pressure, density, velocity, volumetric rate of thermal energy and/or magnetic field) and some signs will be reversed (poloidal velocity and/or poloidal magnetic field). All the technical details of the simulations made are listed in table 5.1 jointly with some observations.

To begin with, each simulation needs a set of fundamental PLUTO files to run. The `init.c` file defines relevant data regarding initial and boundary conditions; `pluto.ini` refers to the number of grid zones and output frequency; `definitions.h` concerns the simulation geometry, dimensions and time stepping. For the following simulations, a cooling function was implemented (`cooling.c`), where the heating source described previously, was coded in C programming language by Véronique Cayatte from the Astronomical Observatory of Paris.

In the following subsections, detailed observations for each simulation are drawn. But before analysing the results, it will be mentioned some initial considerations regarding the simulations taxonomy:

- **Testxyz**: Test001, Test002, Test003 and so on refer to the first simulations done with specific values for the multiplying factors of V_r and V_θ and/or with different implemented cooling functions;
- **Testxyz_wt**: The fifth and sixth numbers of the simulation ID, is indicative of the number of the remake of the simulation, which includes small changes always mentioned in table 5.1. For example, Test001_03 is the third remake for Test001. This simulation uses the same initial values as in Test001 for V_r and V_θ multiplying factors, but has a different radius R_{beg} (boundary radius where the numerical simulations begin) plus some alterations implemented in the `cooling.c` file.

Test001

For both simulations Test001 and Test001_01, ran in different computers (my personal laptop and CAUP server, respectively), it was not possible to reach any conclusions due to the fact that during the running process were found NaNs (i.e. Not a Number) and the simulations automatically stopped at 14%.

In order to solve the problem, the resolution was lowered from 512 to 200 in Test001_02. Although the simulation ran longer, it was not sufficient to pass the 29% barrier.

In another attempt with Test001_03, the initial radius R_{beg} was changed from 0.20 to 0.30 and the heating sign from `cooling.c` file was reversed (it will be mentioned hereinafter as new cooling) and the simulation ran successfully until 100%. In figure 5.6, when observing the angular velocity plots (Ω) at $t = 2.5$, it is possible to observe a structure at $\varpi = 0.9$ which evolves to a loop at $t = 5.0$ and is also verified for β-parameter[2] and the total angular momentum. Loops are magnetic reconnection events which connect the circumstellar disk with the stellar surface and are related to the presence of shear velocities (also known as friction velocities between layers of a flow). In addition, for the poloidal velocity (V_p) at $t = 5.0$, there is a light shaded streamer associated to the loop and a curved structure near $\varpi \leq 1.5$ near the equatorial plane filled in blue and green. This feature could be identified as an X-wind with origin in the exterior radius of the circumstellar disk. It should be pointed out that the sign inversion in the heating function is solving the problem and not the value change in R_{beg}.

To prove so, Test001_04 includes $R_{beg} = 0.20$, as in these first set of simulations, and jointly with the new cooling the simulation ran until the end with very reasonable results. Furthermore, regarding the angular velocity plots in figure 5.7, it is possible to observe once again a loop structure formation at $t = 5.0$ enabling a star-disk connection and leading to the formation of a streamer when looking to the corresponding poloidal velocity plot. This feature does not seem to stabilize until $t = 10.0$, instead is elongating even further. When computing the toroidal magnetic field (B_ϕ) plots for this simulation (see figure 5.14), its evolution does not evidence any kind of anomalies or strange behaviour.

In order to achieve another more physical simulation, besides maintaining the density, R_{beg} and the new cooling, the B_ϕ sign was reversed in Test001_05. By multiplying B_ϕ with -1.0, the total angular momentum flux L and the angular velocity Ω keep the same values in the magnetosphere relatively to the analytical solution.

In Test001_05 at $t = 0.5$ (see figure 5.8) the toroidal velocity V_ϕ shows two velocity bands that contrasts with positive (warmer colours) and negatives values (blue colours). This bi-band seems to come from the exterior region of the dead zone near $\varpi = 0.8$ and seems to shock with the stellar surface at $\varpi = 0.15$. The same feature can be seen in total angular momentum and angular velocity plots. This simulation could be the most physical solution obtained so far, which describes approximately accretion/wind mechanisms. Furthermore, when looking to the following times, namely at $t = 10.0$, are formed pronounced and elongated features coming out of the equatorial region which are once again associated with streamers

[2] The ratio between the plasma pressure and the magnetic pressure.

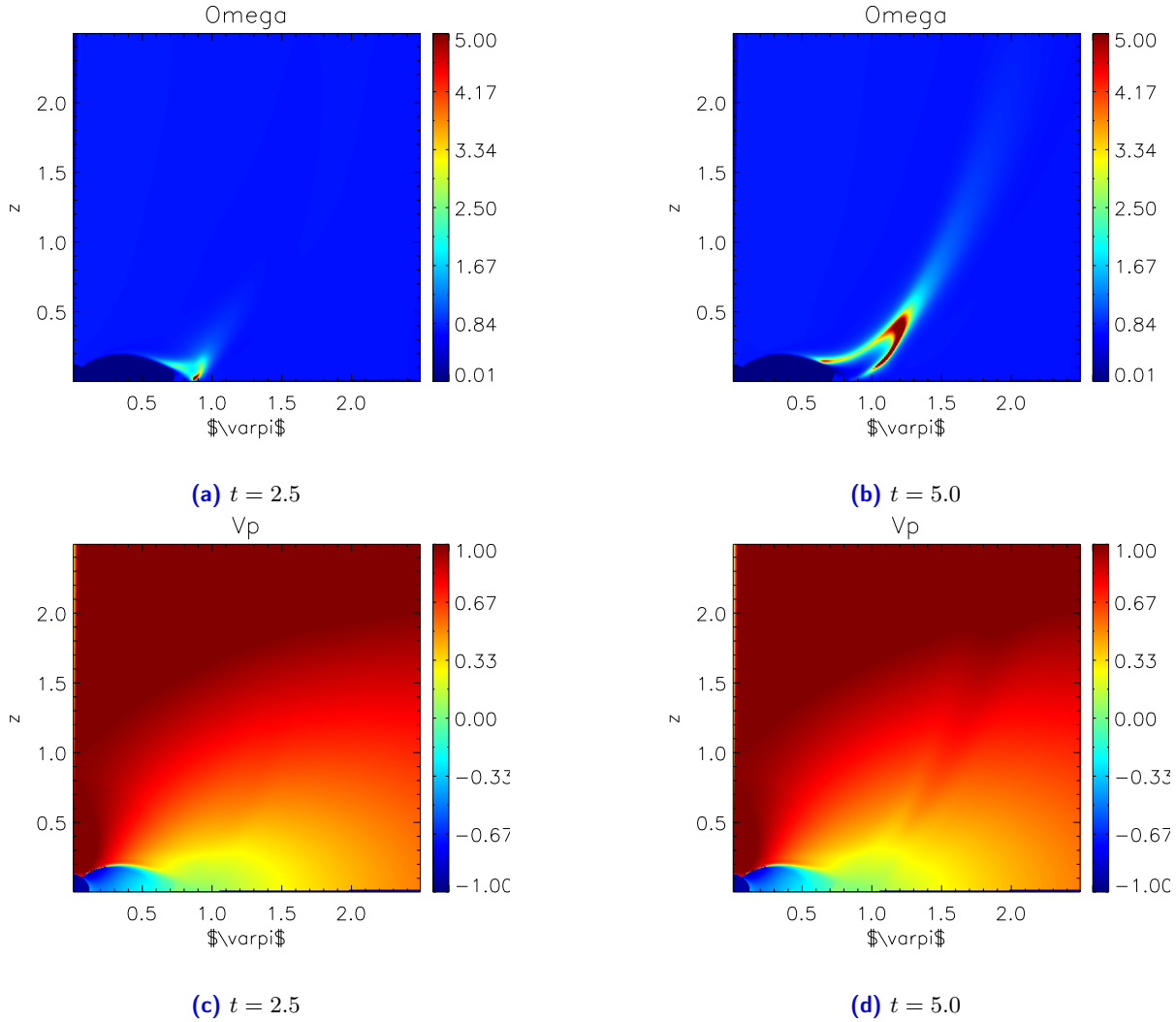

(a) $t = 2.5$ **(b)** $t = 5.0$

(c) $t = 2.5$ **(d)** $t = 5.0$

Figure 5.6: Plots of angular velocity Ω and poloidal velocity V_p for the times mentioned in the subcaption for Test001_03. The x-axis corresponds to the radial distance ϖ, while the y-axis corresponds to height z.

(see figure 5.9). Also, when looking to figure 5.9b, is possible to see a high density structure linking the accretion disk to the star similar to an accretion column. In these two last simulations, the running time was extended until $t = 10.0$ in order to see if the system is able to stabilize during that period.

Test002

Due to the fact that the simulation was performed with the first `cooling.c` file, it stopped at 13% by finding NaNs as in Test001 and Test001_01.

Test003, Test004, Test005

In order to increase the accretion rate, V_r and V_θ were changed in Test003 by a factor of -2.5 and -1.5, respectively. By observing the resulting plots in figure 5.10, the initial irregular bubble structure present in all physical quantities plotted at $t = 0.5$ evolves to a more unstable scenario until $t = 5.0$. The remake of the latest simulation with the new cooling in Test003_01, shows similar perturbed results but with a

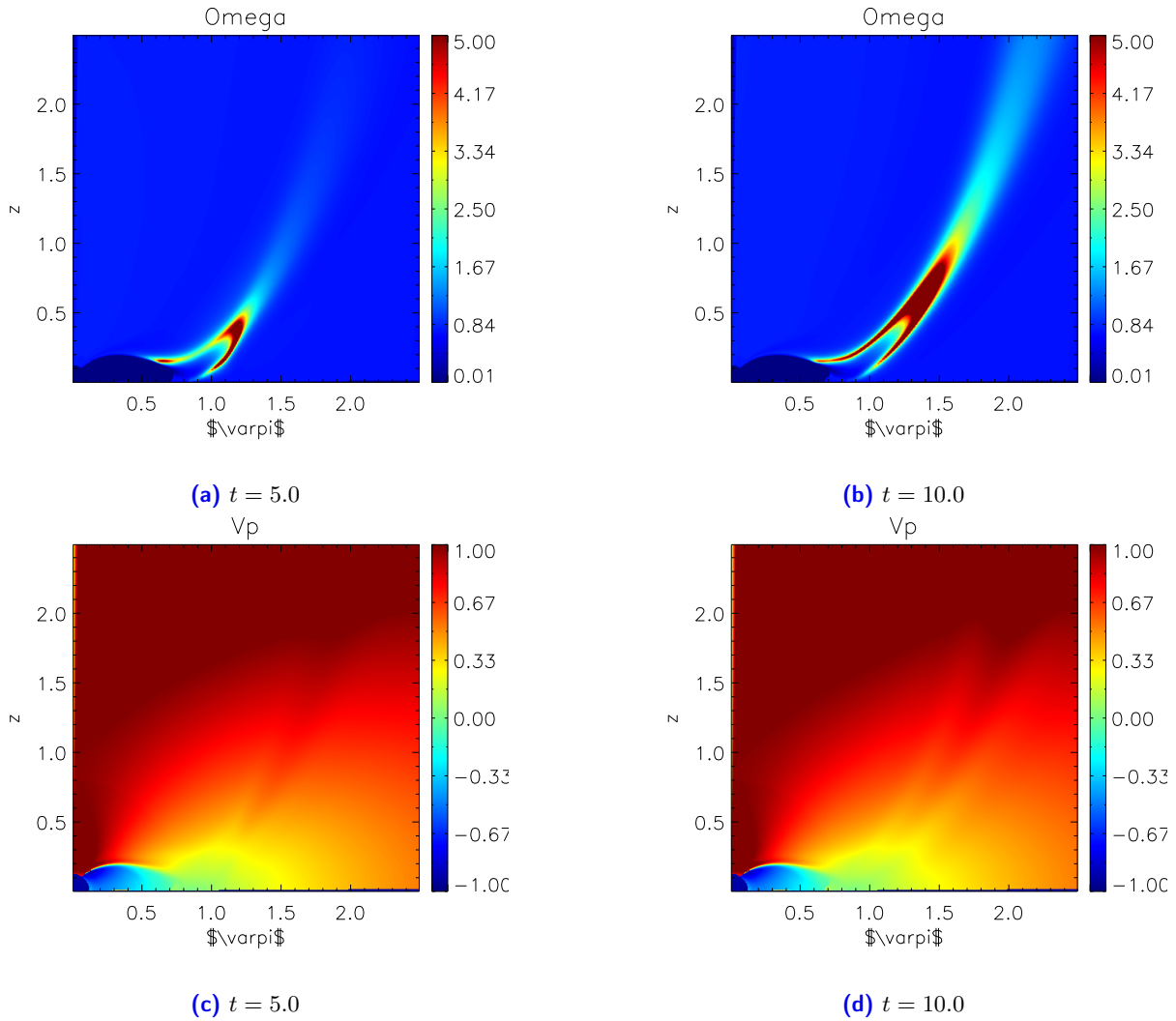

(a) $t = 5.0$ **(b)** $t = 10.0$

(c) $t = 5.0$ **(d)** $t = 10.0$

Figure 5.7: Plots of poloidal velocity V_p and angular velocity Ω, for the times mentioned in the subcaption for Test001_04. The x-axis corresponds to the radial distance ϖ, while the y-axis corresponds to height z.

slightly less intense values, which are more evident when comparing L plots in both tests, for instance.

Regarding Test004 and Test004_01, these simulations show even more pronounced instabilities with or without the sign inversion on the heating function and the same applies to Test005 and Test005_01, where sinusoidal structures may be observed for all quantities at $t = 5.0$ (see figure 5.11).

Test006, Test007, Test008

Taking a closer look at both simulations Test006 and Test006_01, where V_r and V_θ coefficients were increased to 1.0 and 1.5 respectively, it is possible to observe at $t = 0.5$ a bubble structure around the star, which is more evident among L plots (see figure 5.12). In the latter ones, for Test006, we may see higher values for the total angular momentum coming from a dark blue region of lower values attached to the simulated star. The same region is more elongated in the corresponding plot in Test006_01, but seems to be more stable when considering the new cooling and the same applies to the remaining plots. Could this region be formed by NaNs to indicate a non-physical mechanisms that are occurring in that region? When analysing the following times, the structure does not stabilize. Instead it becomes more

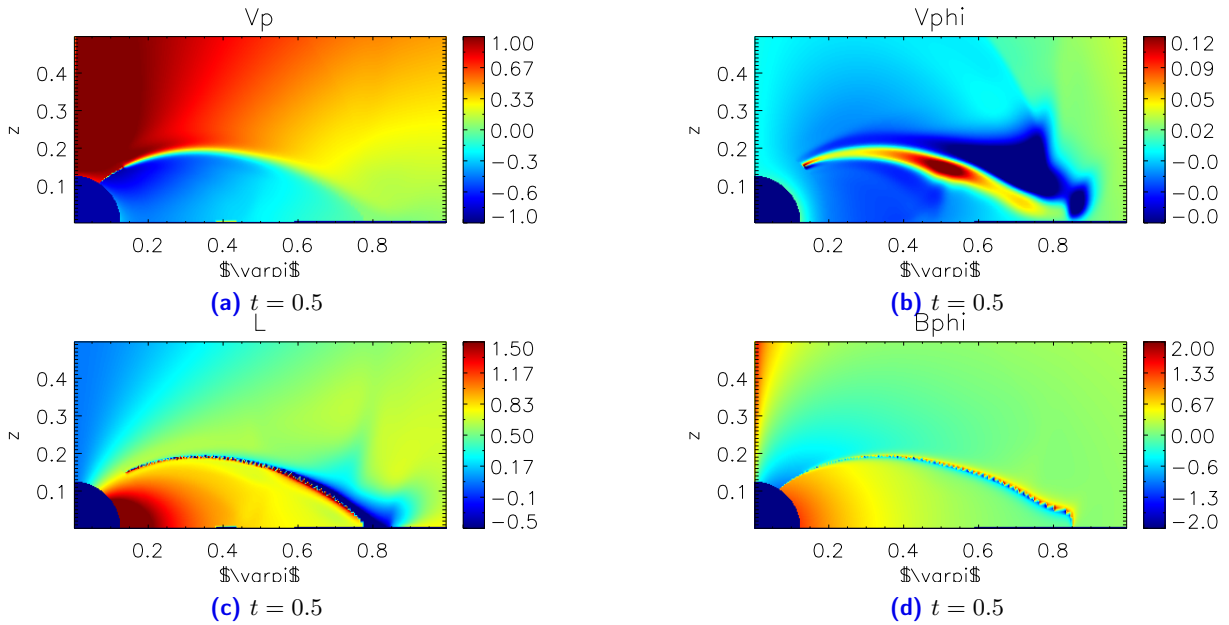

(a) $t = 0.5$ **(b)** $t = 0.5$ **(c)** $t = 0.5$ **(d)** $t = 0.5$

Figure 5.8: Plots of velocities V_p, V_ϕ, Ω and ϕ-component of the magnetic field B_ϕ for the $t = 0.5$ for Test001_05. The x-axis corresponds to the radial distance ϖ, while the y-axis corresponds to height z.

active and eccentric, specially when looking to β-parameter at $t = 5.0$ in both simulations, where a slip coming from the dead zone arises. Here the gas pressure is clearly taking over the magnetic pressure.

The same conclusions can be taken regarding Test007 and Test007_01, where V_r and V_θ coefficients assume both the value -1.5. In these pair of simulations, the rise in the θ-component is going to lead to a more perturbed solution. Features mentioned on the previous test are present as well, but now they appear to be more irregular, intense and unstable until $t = 5.0$.

When assuming $V_r = -2.0$ and $V_\theta = -1.5$ for the velocity coefficients in Test008 and Test008_01, the previous scenario aggravates even further. After $t = 0.5$, the previous features lose their structure and all the plots show evidence of strong perturbations and instability.

Test009

Since the new cooling is bringing more stability to the system, all the following simulations will be computed with this change.

In Test009 and Test009_01, V_r and V_θ multiplying factors are assumed to be -2.0 and -1.0 respectively, and for the latest simulation, the volumetric rate of the thermal energy (q) was also increased by the same amount as V_r, which led to more intense instabilities (see figure 5.13). This alteration was implemented for all remakes of Test009. Identically to Test006 and Test006_01, the bubble structures are present in both simulations at time $t = 0.5$ for several physical quantities: V_p, V_ϕ, Ω, L and B_p. In addition, at $t = 2.5$ there is a disruption of these structures which evolved to unstable configurations in the following time.

An important detail forgotten during the simulations was that the polar component V_θ was coded in function of the radial one V_r. So whenever we increased the first component, the second was also increased

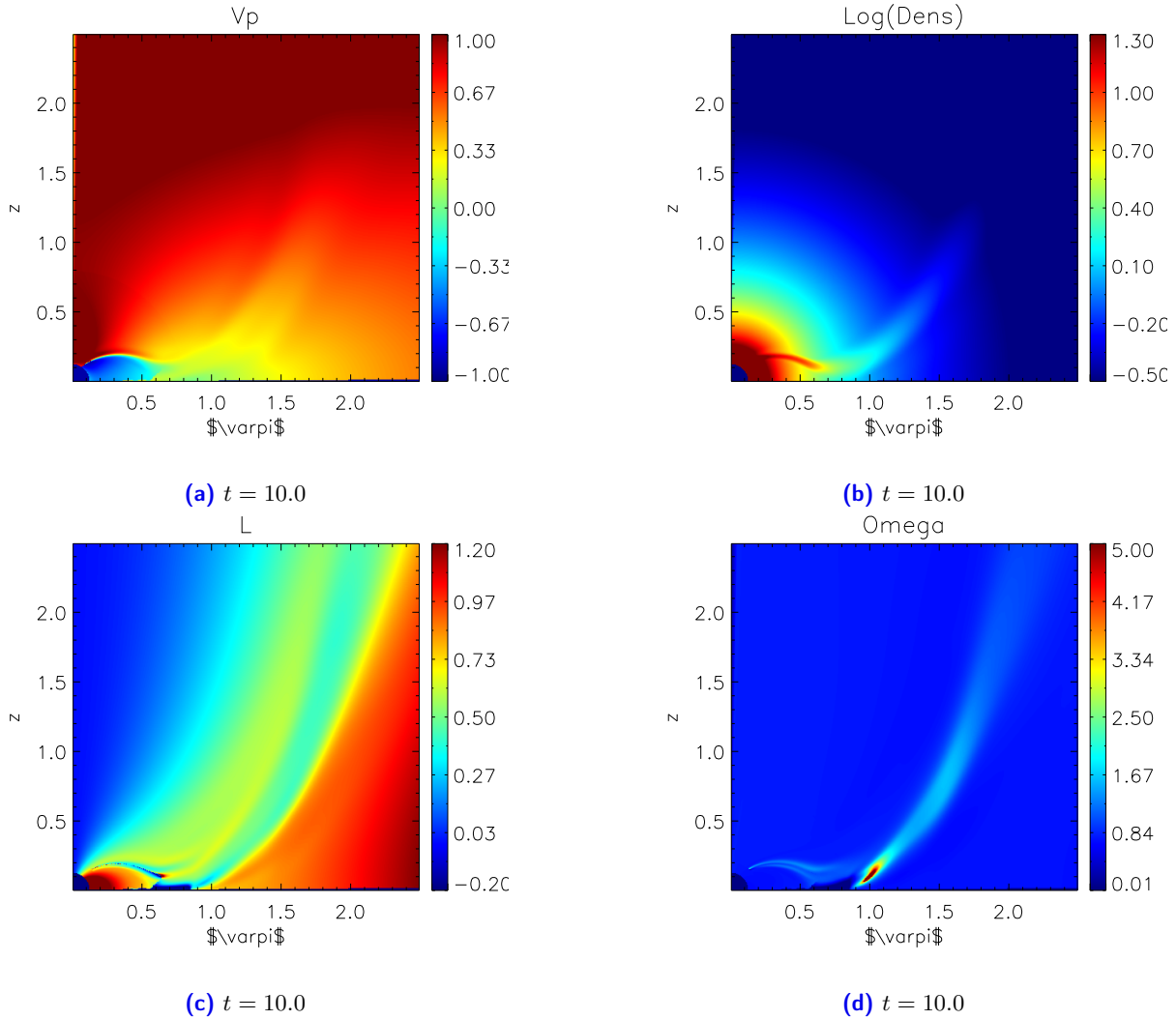

(a) $t = 10.0$ **(b)** $t = 10.0$

(c) $t = 10.0$ **(d)** $t = 10.0$

Figure 5.9: Plots of densitity $\log \rho$, total angular momentum L and velocities V_p, Ω for $t = 10.0$ for Test001_05.The x-axis corresponds to the radial distance ϖ, while the y-axis corresponds to height z.

by the same factor. Only from Test009_02, the polar component was kept the same while the radial component of the velocity was multiplied by different factors.

In order to maintain the proportion of multiplying factors between V_r and V_θ, from Test009_02 to Test009_10, the corresponding coefficients will be assumed as -2.0 and -0.5. In Test009_02 there is a strange behaviour concerning the evolution of B_ϕ, where a round structure, located near the dead zone between $0.4 \leq \varpi \leq 0.6$, appears at time $t = 0.3$ and its intensity decreases until a minimum at $t = 3.0$ (see figure 5.14). Afterwards, the intensity of the magnetic field in that region increases and the feature becomes more diffuse. This behaviour is not observed for B_ϕ in Test001_04.

Furthermore, regarding the β-parameter plot in figure 5.15, it is possible to observe a loop structure formation with some extension at $t = 5.0$, which is also evident among other physical quantities as well (L, Ω and V_ϕ, for example). This structure is more pronounced relatively to Test001_04 and shows a loop discontinuity near $\varpi = 0.9$. The question is if this feature is physical and could it be related to the disconnection of magnetic fieldlines, which lead to the formation of magnetospheric ejections as studied by Zanni and Ferreira (2013), similarly to coronal mass ejections which are the result of flares followed

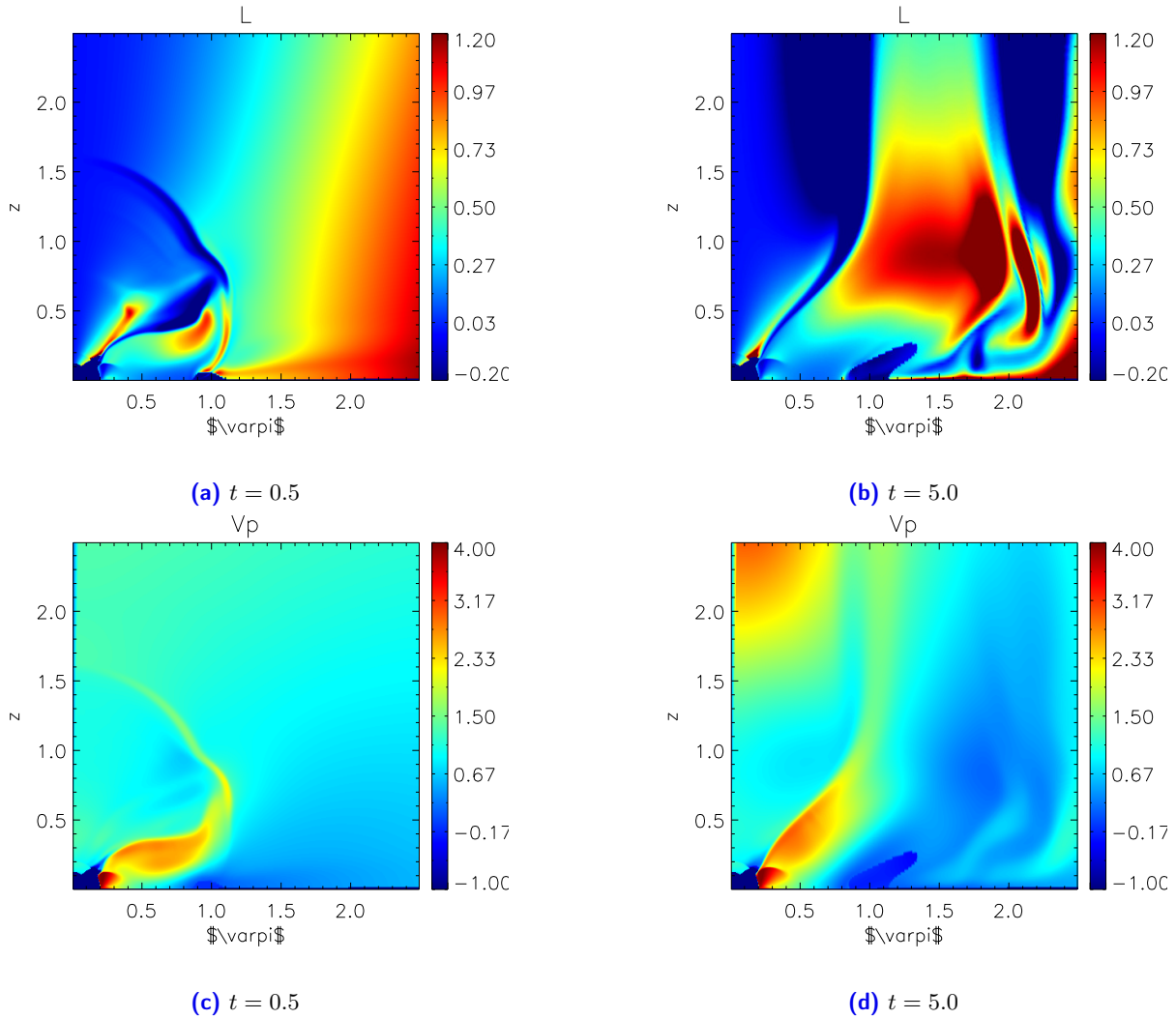

(a) $t = 0.5$ **(b)** $t = 5.0$

(c) $t = 0.5$ **(d)** $t = 5.0$

Figure 5.10: Plots for the total angular momentum L and poloidal velocity V_p for the times mentioned in the subcaption for Test003. The x-axis corresponds to the radial distance ϖ, while the y-axis corresponds to height z.

by reconnection events (Sauty et al., 2011). Also, taking a closer look at the poloidal velocity and the logarithmic density ($\log(\rho)$) it is possible to observe streamers coming from the equatorial region.

By increasing the density, ρ, the mass flux is increased as well as the accretion rate onto the star. For such matter, in Test009_03 both pressure and density were increased by a factor of 5 in the initial border conditions. At time $t = 0.5$ in figure 5.16, is possible to observe the formation of mysterious and complex vortex feature, which is more evident in the plots for β-parameter and $\log(\rho)$. In addition of this massive increase, from $t = 2.5$ to $t = 5.0$, the simulation return highly unstable results.

In Test009_04 only the density was increased by a factor of 5 in the initial border conditions, but the simulation crashed at half way probably due to instabilities in B_ϕ. For such matter, its sign was inverted and this alteration was implemented from Test009_06 to Test013.

Observing the results in Test009_06 (remake of Test009_02 with the reversed sign of B_ϕ) at $t = 0.5$ in figure 5.17, we can see clearly the inversion of V_p and V_ϕ values are more intense when compared to Test001_05. In the following times there is the formation of a more irregular loop structure. Nevertheless, this simulation shows more stability in the accretion and outflow regions relatively to Test009_02.

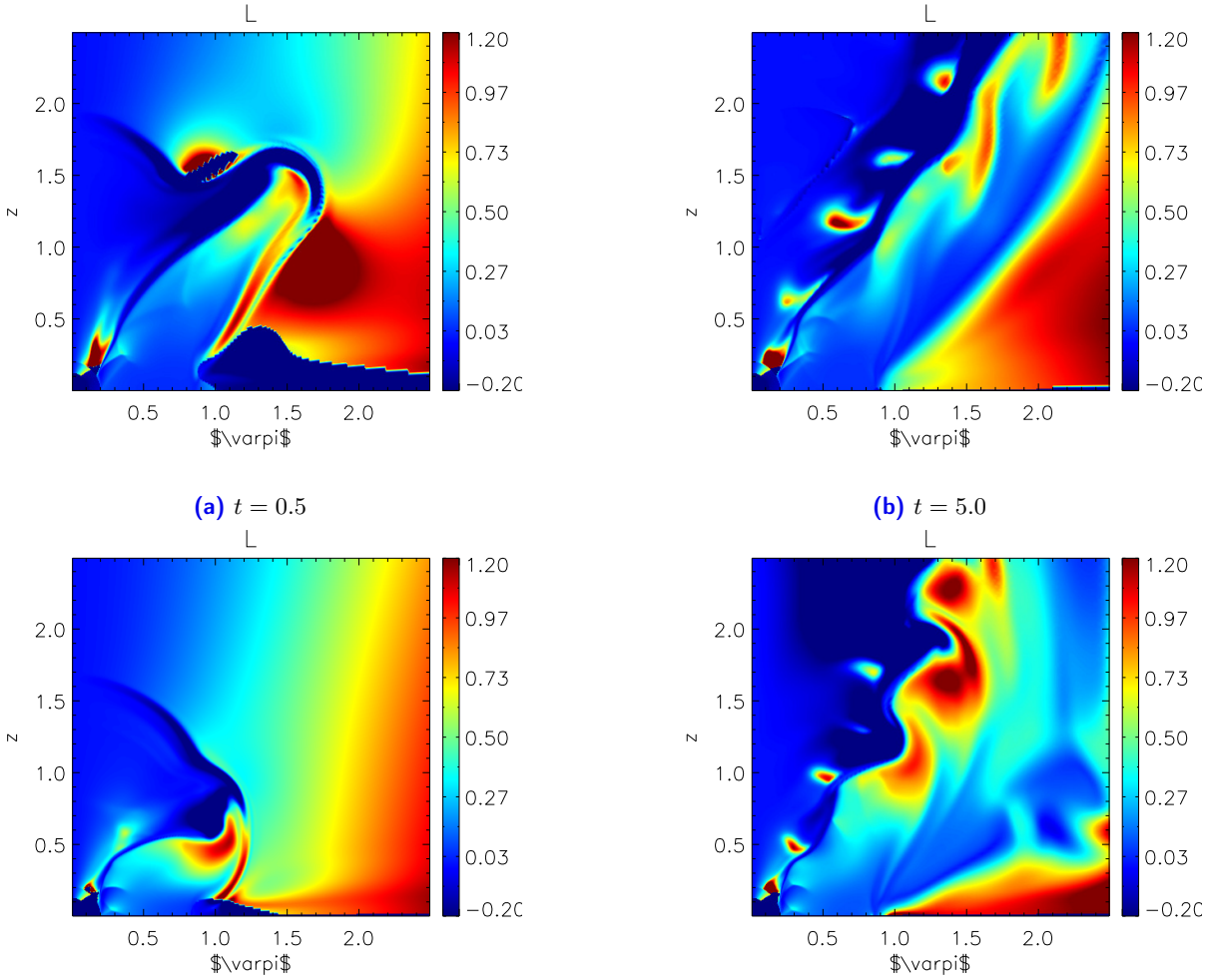

(a) $t = 0.5$ **(b)** $t = 5.0$

(c) $t = 0.5$ **(d)** $t = 5.0$

Figure 5.11: Plots for the total angular momentum L for the times mentioned in the subcaption for Test004 (first row) and Test005 (second row). The x-axis corresponds to the radial distance ϖ, while the y-axis corresponds to height z.

In Test009_07 (which is the remake of Test009_04 with the reversed sign of B_ϕ), V_ϕ plots in figure 5.18 for $t = 0.5$ show some high velocity regions inside $\varpi = 1.0$, that are increasing and becoming more unstable towards $t = 5.0$. In addition, a loop structure is visible at $t = 2.5$ for β-parameter and it seems that is falling towards the equatorial plane. Also, a streamer is evident in V_p and L plots at $t = 5.0$.

Regarding the remaining simulations, Test009_05, Test009_08, Test009_09 and Test009_10 all of them crashed due to abrupt decreases in the time-step (dt). This is probably due to sharp gradients for density, pressure, velocity or magnetic field, which lead to a thermally unstable system and PLUTO cannot adjust the time step in the calculations.

Test010, Test011, Test012 and Test013

Test010 has the same velocity multiplying factors as Test001 and following remakes, but the cooling function was changed to account for the shift between the results of the analytical solution and the computed ones, as mentioned previously (hereafter 2^{nd} new cooling). In figure 5.19 is represented V_p, where streamers coming from the equatorial region can be seen and are supported by lower angular

momentum values and high β-parameter values. The latter means that there is a dominance of kinetic over magnetic energy contribution for the outflow of the stellar material. In addition, a high density column in $\log(\rho)$ plot related to a possible magnetospheric column is present.

In Test011, V_r was increased by a factor of 1.5, while ρ was kept with its original value. When comparing the same physical quantities at time $t = 7.5$ in figure 5.20, the corresponding values are higher and it seems that there is a disconnection near $\varpi = 1.5$. To clarify this feature, were plotted the poloidal velocity and mass flux plots $(\log(\rho|V_p|))$, jointly with the poloidal magnetic fieldlines in figure 5.21 and this seems that we are assisting the formation process of a magnetospheric ejection, observed by Zanni and Ferreira (2013) with axisymmetric time-dependent MHD simulations. When comparing these two quantities, it is possible to observe in the mass flux column that there is a disconnection feature at $t = 5.0$ followed by a reconnection event at $t = 20.0$, identical to $t = 2.5$. Regarding the poloidal velocity, the green elongated structures at $t = 5.0$ become more diffuse towards $t = 20.0$ and the higher velocities seem to go along a mass ejection.

In these four simulations is possible to observe sporadic X-winds. Specially when density is increased in Test012 and Test013 by a factor of 5 and 10, respectively, because mass flux in X-wind is powered by accretion. In the former simulation, as density is increased, the mass flux increases and the region with negative values for the poloidal velocity is more extended (near $\varpi = 0.8$) in figure 5.22a. Interestingly, the density shows negative values in figure 5.22b relatively to opposite ones in the previous simulation (see 5.20b). In figures 5.22c and 5.22d, the disconnection structure seen in the previous simulation does not exist for this case.

Regarding Test013, by increasing the density by a factor of 10, helmet streamer perturbations and coronal mass ejections can be seen as well as a decreasing of the stellar jet region (see figure 5.23). Besides the induction of higher mass fluxes through density, this alteration reflected also in a more unstable simulation relatively to Test012, as illustrated in figure 5.24.

It was discussed that it seems that to increase velocity, density needs also to be increased. But there could also be only one set of suitable density values for each multiplying factor for velocity.

It was observed that Test010 and Test011 are not static along time but show more stability when comparing to the remaining ones. Although there are some instabilities, they do not seem to destroy the overall outflow. In addition, the simulations ran to the end without abrupt time step (dt) decreases.

Table 5.1: List of all PLUTO simulations made. In the table are listed the simulation identification (1^{st} column), date in which the simulation was made and corresponding initial, final and elapsed time (2^{nd} to 5^{th} columns, respectively). Finished/Interrupted simulations are also listed (6^{th} column), as well as the multiplying factors for V_r and V_θ (7^{th} and 8^{th} columns, respectively). Observations regarding the simulations are mentioned in the 9^{th} column

Simulation ID	Date	Start	End	Elapsed time	Status	Inversion V_p		Observations
						V_r	V_θ	
Test001	11 Mar 2015	15:48:24	?	?	Interrupted	-1.0	-0.5	Interrupted in laptop at 14%
Test001_01	18 Mar 2015	10:46:00	?	?	Interrupted	-1.0	-0.5	Remake in Supernova. The simulation is taking too long at stage 14%. Same problem as in Test001?! NaN found at 14%.
Test001_02	23 Mar 2015	15:46:57	?	?	Interrupted	-1.0	-0.5	Same as Test001 but with lower resolution (R=200). The simulation is taking too long at stage 29%. NaN found at 29%.
Test001_03	24 Mar 2015	14:44:14	21:44:18	0d:7h:0m:3s	Finished	-1.0	-0.5	New cooling.c and Rbeg changed from 0.2 to 0.3.
Test001_04$*$	25 Mar 2015	15:06:09	22:29:43	0d:7h:23m:34s	Finished	-1.0	-0.5	New cooling.c
	06 Apr 2015	14:27:21	21:59:57	0d:7h:32m:35s	Finished			Restarted simulation Test001_04 from t=5.0 to t=10.0
Test001_05$*$	30 Apr 2015	12:14:22	01:37:56	0d:13h:23m:33s	Finished	-1.0	-0.5	New cooling.c. Remake of Test001_04 with reversed sign of B_ϕ until t=10.0
Test002	13 Mar 2015	11:59:39	?	?	Interrupted	-1.5	-0.5	NaN found at 13%.
Test003	16 Mar 2015	15:20:32	21:52:45	0d:6h:32m:12s	Finished	-2.5	-1.5	
Test003_01	26 Mar 2015	09:38:07	17:02:06	0d:7h:23m:59s	Finished	-2.5	-1.5	New cooling.c
Test004	17 Mar 2015	10:03:25	18:55:31	0d:8h:52m:6s	Finished	-2.5	-3.0	
Test004_01	26 Mar 2015	09:44:18	18:52:29	0d:9h:8m:11s	Finished	-2.5	-3.0	New cooling.c
Test005	18 Mar 2015	09:48:45	17:38:53	0d:7h:50m:7s	Finished	-1.5	-3.0	
Test005_01	26 Mar 2015	09:37:06	17:08:12	0d:7h:31m:6s	Finished	-1.5	-3.0	New cooling.c
Test006	20 Mar 2015	12:07:24	19:33:30	0d:7h:26m:6s	Finished	-1.0	-1.5	
Test006_01	25 Mar 2015	16:25:28	23:53:23	0d:7h:27m:54s	Finished	-1.0	-1.5	New cooling.c
Test007	20 Mar 2015	12:07:56	19:13:45	0d:7h:5m:48s	Finished	-1.5	-1.5	
Test007_01	25 Mar 2015	16:26:47	23:53:25	0d:7h:26m:38s	Finished	-1.5	-1.5	New cooling.c
Test008	20 Mar 2015	12:08:25	19:27:56	0d:7h:19m:30s	Finished	-2.0	-1.5	
Test008_01	26 Mar 2015	09:36:29	16:57:46	0d:7h:21m:16s	Finished	-2.0	-1.5	New cooling.c

Table 5.1: (continued)

Simulation ID	Date	Start	End	Elapsed time	Status	Inversion V_p		Observations
						V_r	V_θ	
Test009	25 Mar 2015	15:06:43	22:37:36	0d:7h:30m:52s	Finished	-2.0	-1.0	New cooling.c
Test009_01	06 Apr 2015	14:44:55	22:30:54	0d:7h:45m:59s	Finished	-2.0	-1.0	New cooling.c with theq=VX1 (line 205)
Test009_02$*$	07 Apr 2015	16:19:51	23:48:19	0d:7h:28m:27s	Finished	-2.0	-0.5	New cooling.c with theq=VX1 (line 205)
Test009_03	16 Apr 2015	11:55:16	20:11:16	0d:8h:15m:59s	Finished	-2.0	-0.5	New cooling.c with theq=VX1 (line 205) PRS and RHO increased by a factor of 5 on init.c
Test009_04$*$	20 Apr 2015	09:58:23	?	?	Interrupted	-2.0	-0.5	New cooling.c with theq=VX1 (line 205) RHO increased by a factor of 5 on init.c **Error message** on pluto.log at 53%: ! dt is too small (9.989903e-15)! ! Cannot continue
Test009_05	20 Apr 2015	09:59:23	?	?	Interrupted	-2.0	-0.5	New cooling.c with theq=5*VX1 (line 205) PRS and RHO increased by a factor of 5 on init.c. **Error message** on pluto.log: ! dt is too small (9.541526e-15)! ! Cannot continue
Test009_06 $*$	30 Apr 2015	12:19:41	19:06:35	0d:6h:46m:53s	Finished	-2.0	-0.5	New cooling.c with theq=VX1 (line 205). Remake of Test009_02 with reversed sign of B_ϕ
Test009_07$*$	05 May 2015	14:30:05	21:16:27	0d:6h:46m:22s	Finished	-2.0	-0.5	New cooling.c with theq=VX1 (line 205) RHO increased by a factor of 5 on init.c Remake of Test009_04 with reversed sign of B_ϕ
Test009_08	05 May 2015	14:32:55	?	?	Interrupted	-2.0	-0.5	New cooling.c with theq=VX1 (line 205). Remake of Test009_06 with reversed sign of B_ϕ and B_p increased by a factor of 2 **Error message** on pluto.log: ! dt is too small (9.980791e-15)! ! Cannot continue

Table 5.1: (continued)

Simulation ID	Date	Start	End	Elapsed time	Status	Inversion V_p		Observations
						V_r	V_θ	
Test009_09	05 May 2015	14:40:23	?	?	Interrupted	-2.0	-0.5	New cooling.c with theq=VX1 (line 205) RHO increased by a factor of 5 on init.c Remake of Test009_07 with reversed sign of B_ϕ and B_p increased by a factor of 2. **Error message** on pluto.log: ! dt is too small (9.914590e-15)! ! Cannot continue
Test009_10	05 May 2015	14:41:44	?	?	Interrupted	-2.0	-0.5	New cooling.c with theq=VX1 (line 205) RHO increased by a factor of 5 on init.c Remake of Test009_07 with reversed sign of B_ϕ increased by a factor of $\sqrt{5}$ and B_p increased by a factor of $2\sqrt{5}$. **Error message** on pluto.log: ! dt is too small (9.741391e-15)! ! Cannot continue
Test010$*$	23 June 2015	10:36:35	09:00:25	0d:22h:23m:49s	Finished	-1.0	-0.5	2^{nd} new cooling.c file. Reversed sign of B_ϕ. Ran until $t = 20.0$.
Test011$*$	23 June 2015	10:38:30	08:59:00	0d:22h:20m:29s	Finished	-1.5	-0.5	2^{nd} new cooling.c file. Reversed sign of B_ϕ. Ran until $t = 20.0$.
Test012$*$	23 June 2015	10:39:55	?	?	Interrupted	-1.5	-0.5	2^{nd} new cooling.c file. Reversed sign of B_ϕ. RHO was multiplied by a factor of 5 on init.c. Simulation was interrupted because was taking too long at 98% (more than 16 days!!!).
Test013$*$	23 June 2015	10:40:55	08:44:35	0d:22h:3m:40s	Finished	-2.0	-0.5	2^{nd} new cooling.c file. Reversed sign of B_ϕ. RHO was multiplied by a factor of 10 on init.c Ran until $t = 20.0$.

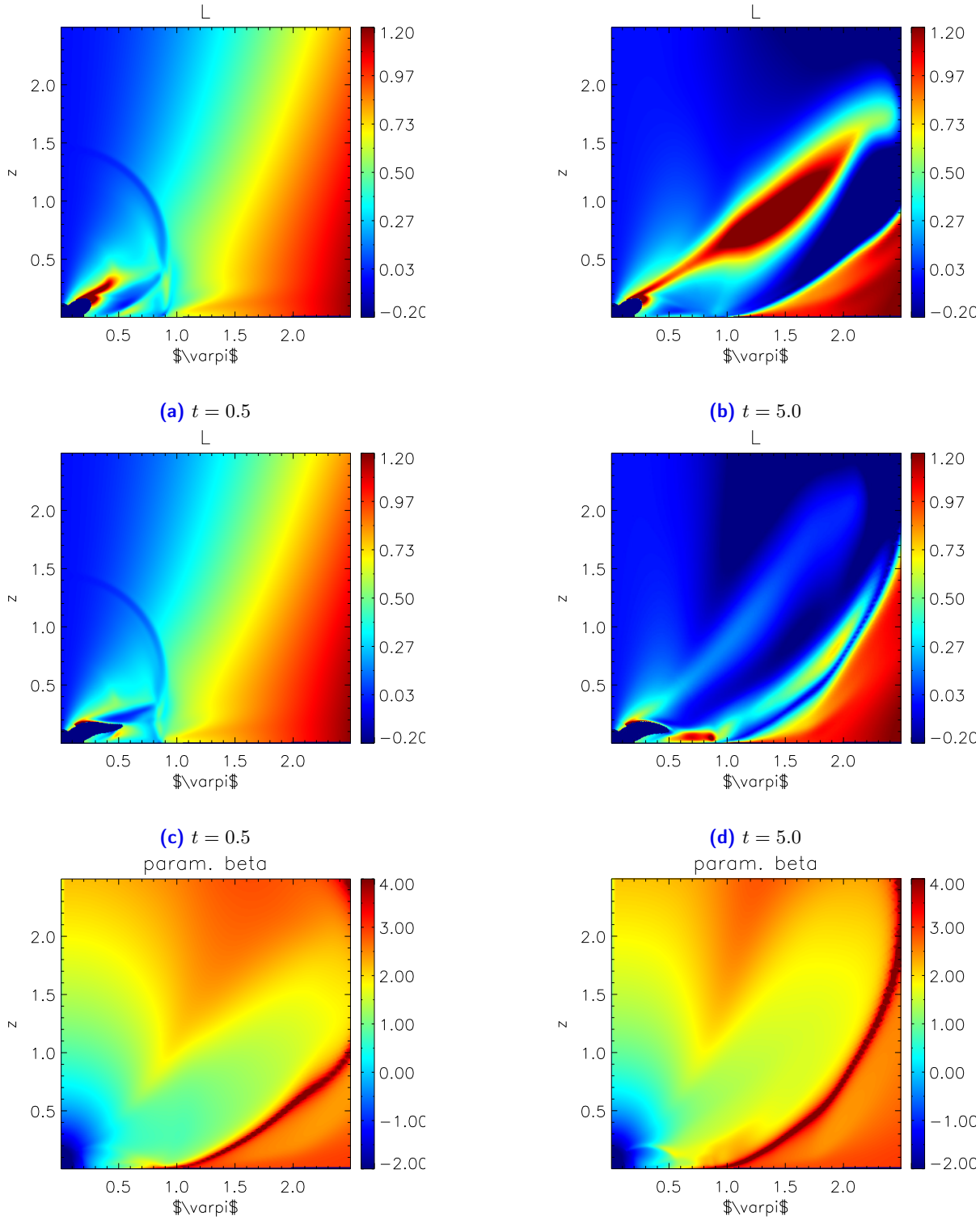

(a) $t = 0.5$ **(b)** $t = 5.0$

(c) $t = 0.5$ **(d)** $t = 5.0$

(e) Test006 $t = 5.0$ **(f)** Test006_01 $t = 5.0$

Figure 5.12: Plots for the total angular momentum L for the times mentioned in the subcaption for Test006 (first row) and Test006_01 (second row). The β-parameter is represented in the third row for Test006 and Test006_01. The x-axis corresponds to the radial distance ϖ, while the y-axis corresponds to height z.

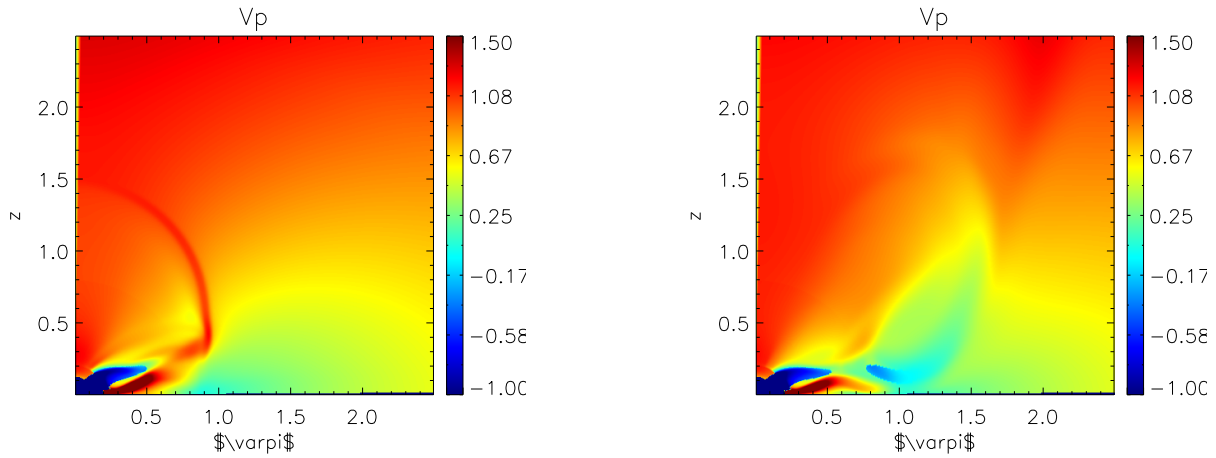

(a) $t = 0.5$ **(b)** $t = 2.5$

(c) $t = 0.5$ **(d)** $t = 2.5$

Figure 5.13: Plots for the poloidal velocity V_p for the times mentioned in the subcaption for Test009 (first row) and Test009_01 (second row). The x-axis corresponds to the radial distance ϖ, while the y-axis corresponds to height z.

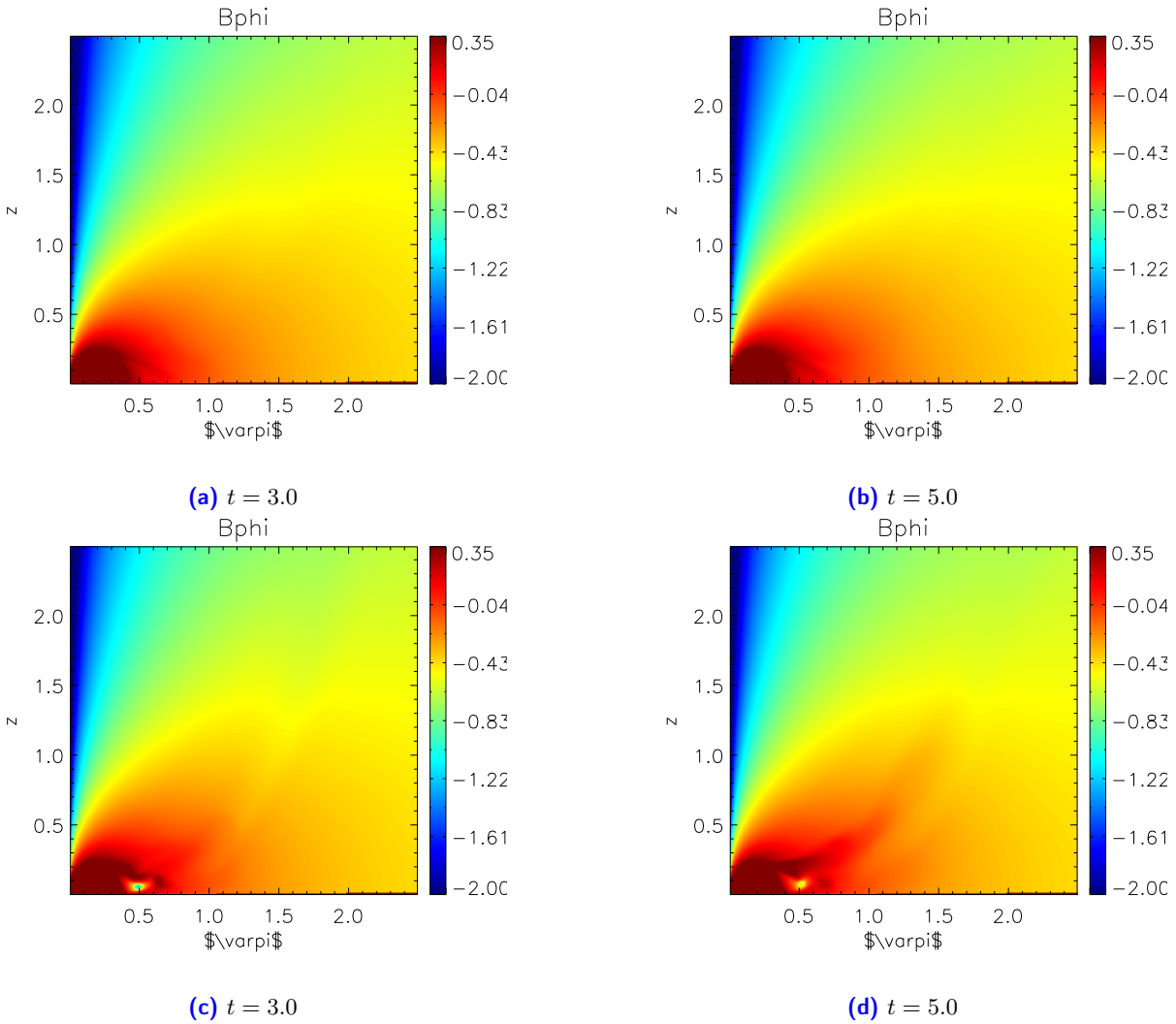

(a) $t = 3.0$ **(b)** $t = 5.0$

(c) $t = 3.0$ **(d)** $t = 5.0$

Figure 5.14: Plots for the ϕ-component of the magnetic field B_ϕ for the times mentioned in the subcaption for Test001_04 (first row) and Test009_02 (second row). The x-axis corresponds to the radial distance ϖ, while the y-axis corresponds to height z.

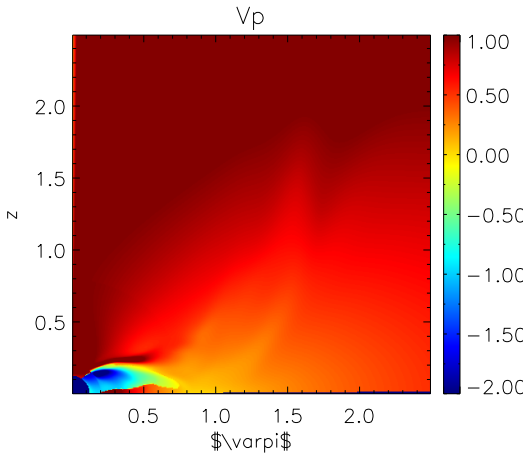

(a) $t = 5.0$

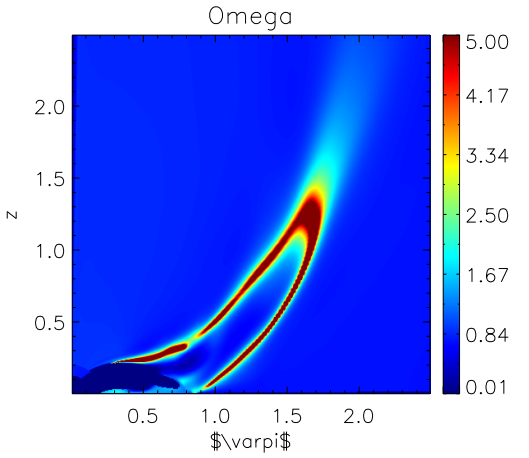

(b) $t = 5.0$

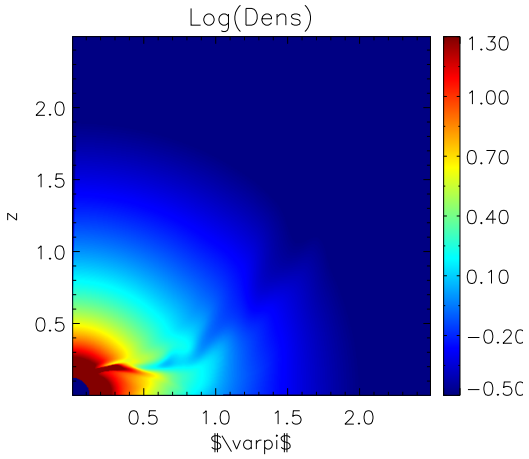

(c) $t = 5.0$

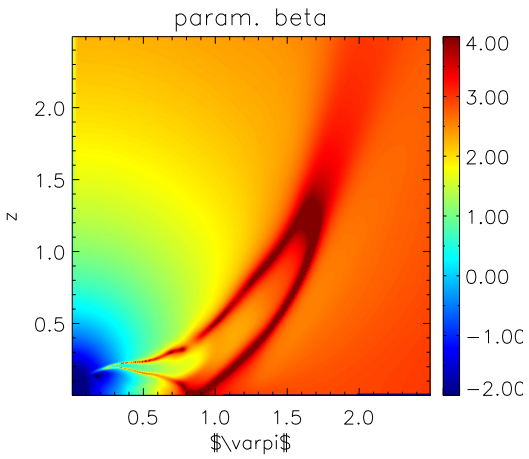

(d) $t = 5.0$

Figure 5.15: Plots for the poloidal velocity V_p, angular velocity Ω, logarithmic density $\log \rho$ and β-parameter for $t = 5.0$ for Test009_02. The x-axis corresponds to the radial distance ϖ, while the y-axis corresponds to height z.

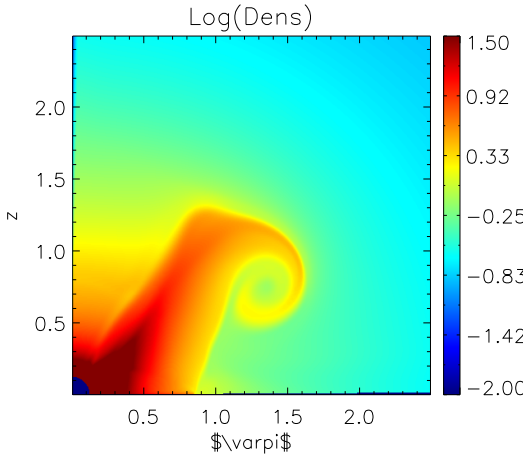

(a) $t = 0.5$

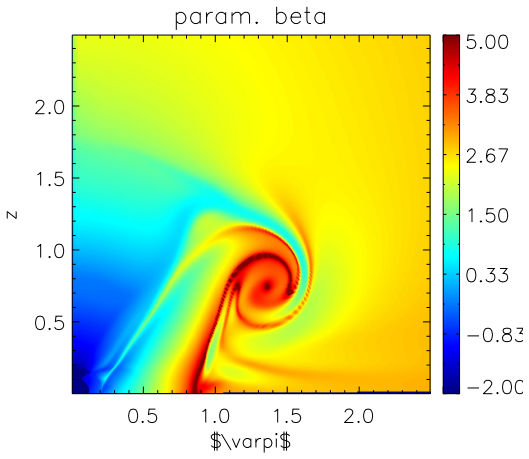

(b) $t = 0.5$

Figure 5.16: Plots for the logarithmic density $\log \rho$ and β-parameter for $t = 0.5$ for Test009_03. The x-axis corresponds to the radial distance ϖ, while the y-axis corresponds to height z.

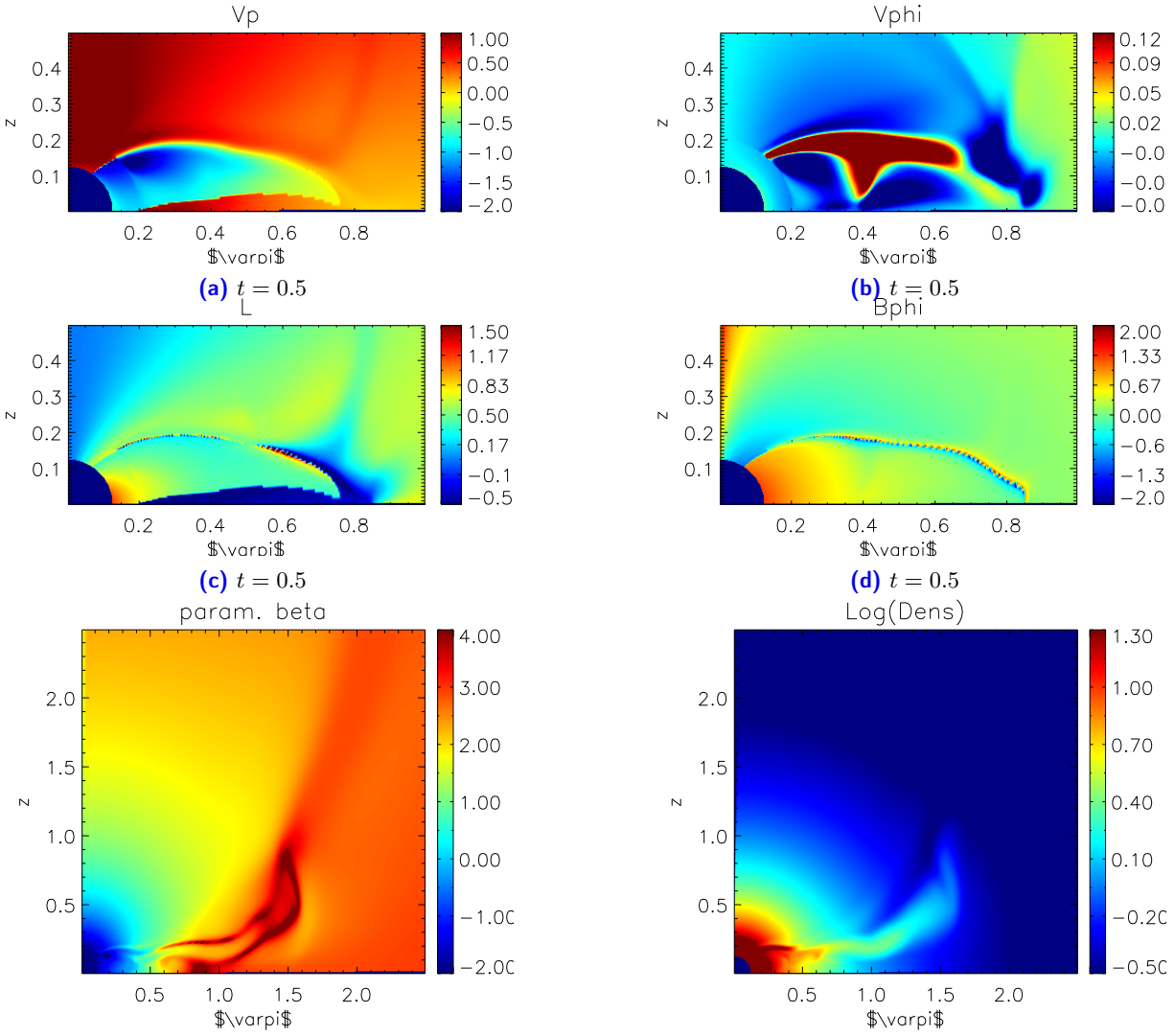

(a) $t = 0.5$ **(b)** $t = 0.5$

(c) $t = 0.5$ **(d)** $t = 0.5$

(e) $t = 5.0$ **(f)** $t = 5.0$

Figure 5.17: Plots of velocities V_p, V_ϕ, Ω and ϕ-component of the magnetic field B_ϕ for the $t = 0.5$ and β-parameter and density ρ at $t = 5.0$ for Test009_06. The x-axis corresponds to the radial distance ϖ, while the y-axis corresponds to height z.

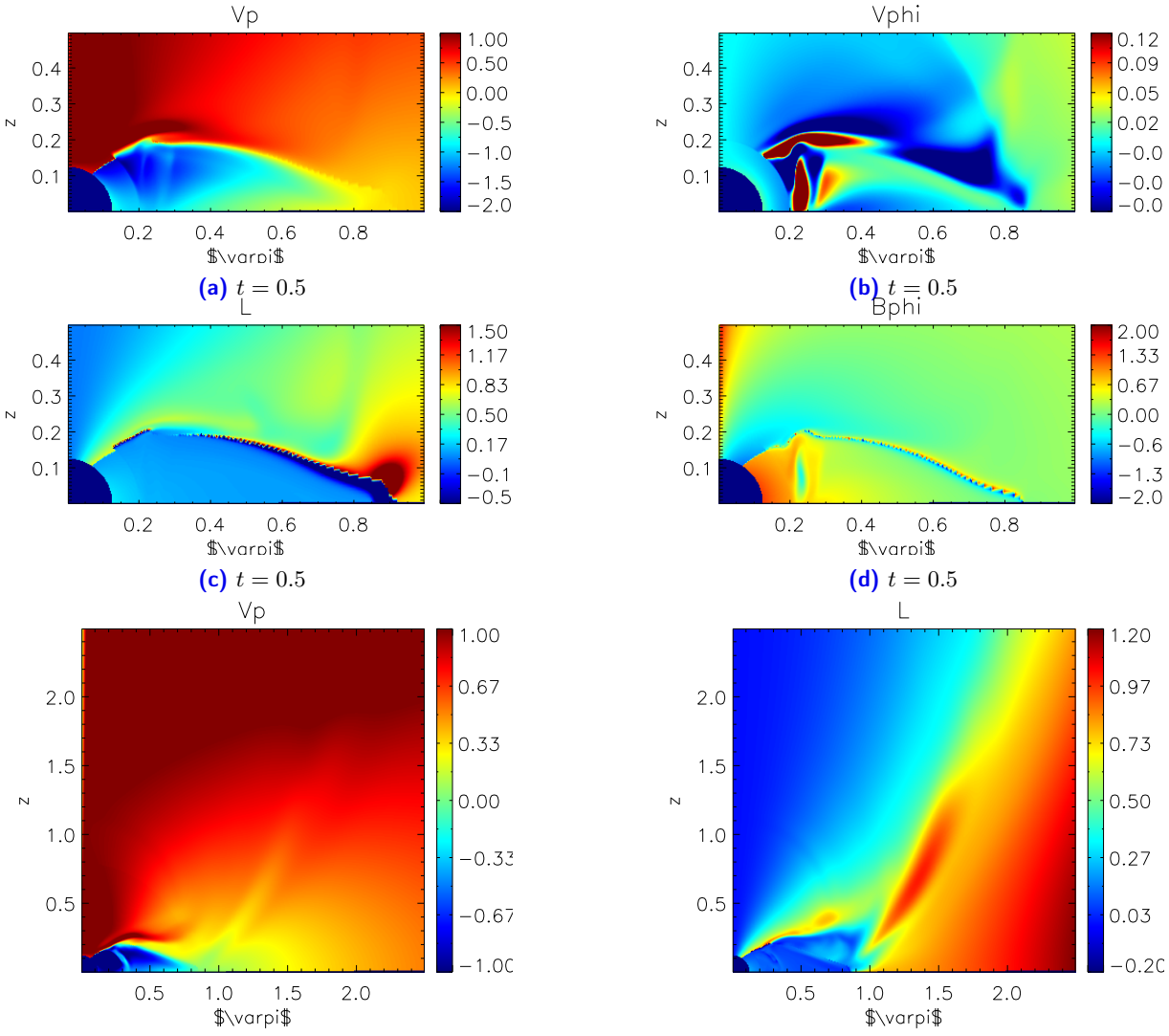

(a) $t = 0.5$ **(b)** $t = 0.5$

(c) $t = 0.5$ **(d)** $t = 0.5$

(e) $t = 5.0$ **(f)** $t = 5.0$

Figure 5.18: Plots of velocities V_p, V_ϕ, Ω and ϕ-component of the magnetic field B_ϕ for the $t = 0.5$ and total angular momentum L and V_p at $t = 5.0$ for Test009_07. The x-axis corresponds to the radial distance ϖ, while the y-axis corresponds to height z.

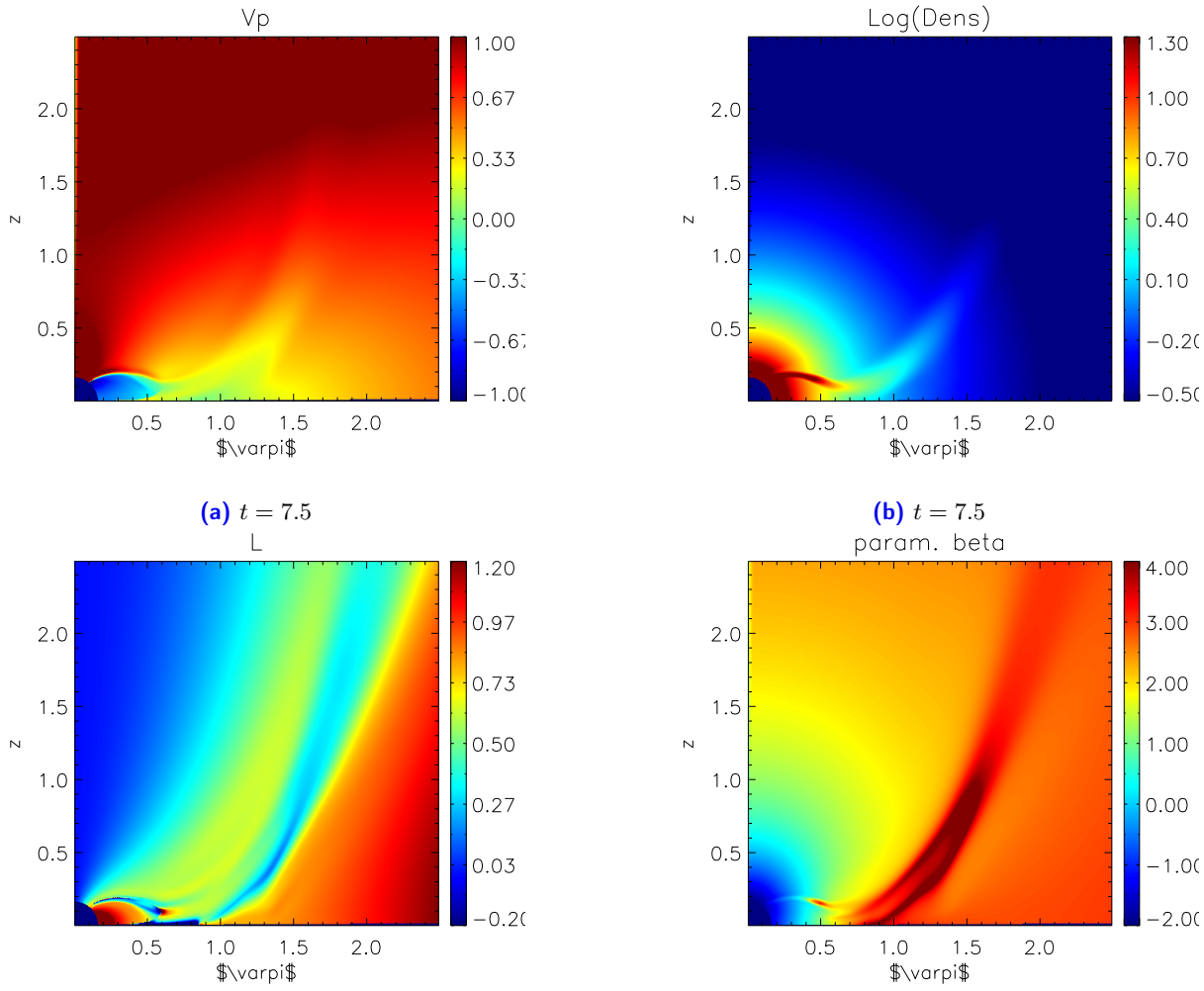

(a) $t = 7.5$ **(b)** $t = 7.5$

(c) $t = 7.5$ **(d)** $t = 7.5$

Figure 5.19: Plots of density $\log \rho$, total angular momentum L, poloidal velocity V_p and β-parameter for $t = 7.5$ for Test010. The x-axis corresponds to the radial distance ϖ, while the y-axis corresponds to height z.

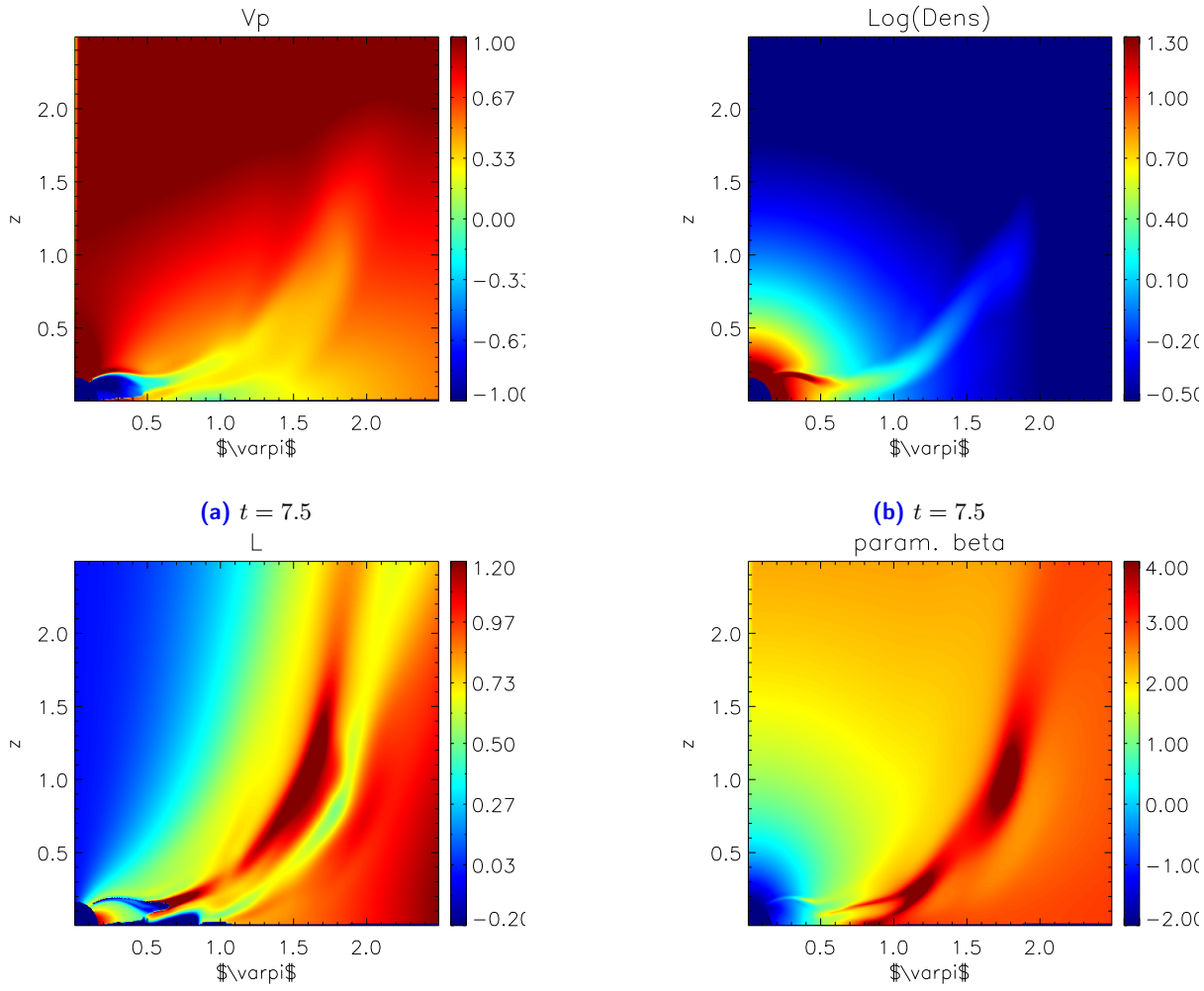

(a) $t = 7.5$

(b) $t = 7.5$

(c) $t = 7.5$

(d) $t = 7.5$

Figure 5.20: Plots of densitity $\log \rho$, total angular momentum L, poloidal velocity V_p and β-parameter for $t = 7.5$ for Test011. The x-axis corresponds to the radial distance ϖ, while the y-axis corresponds to height z.

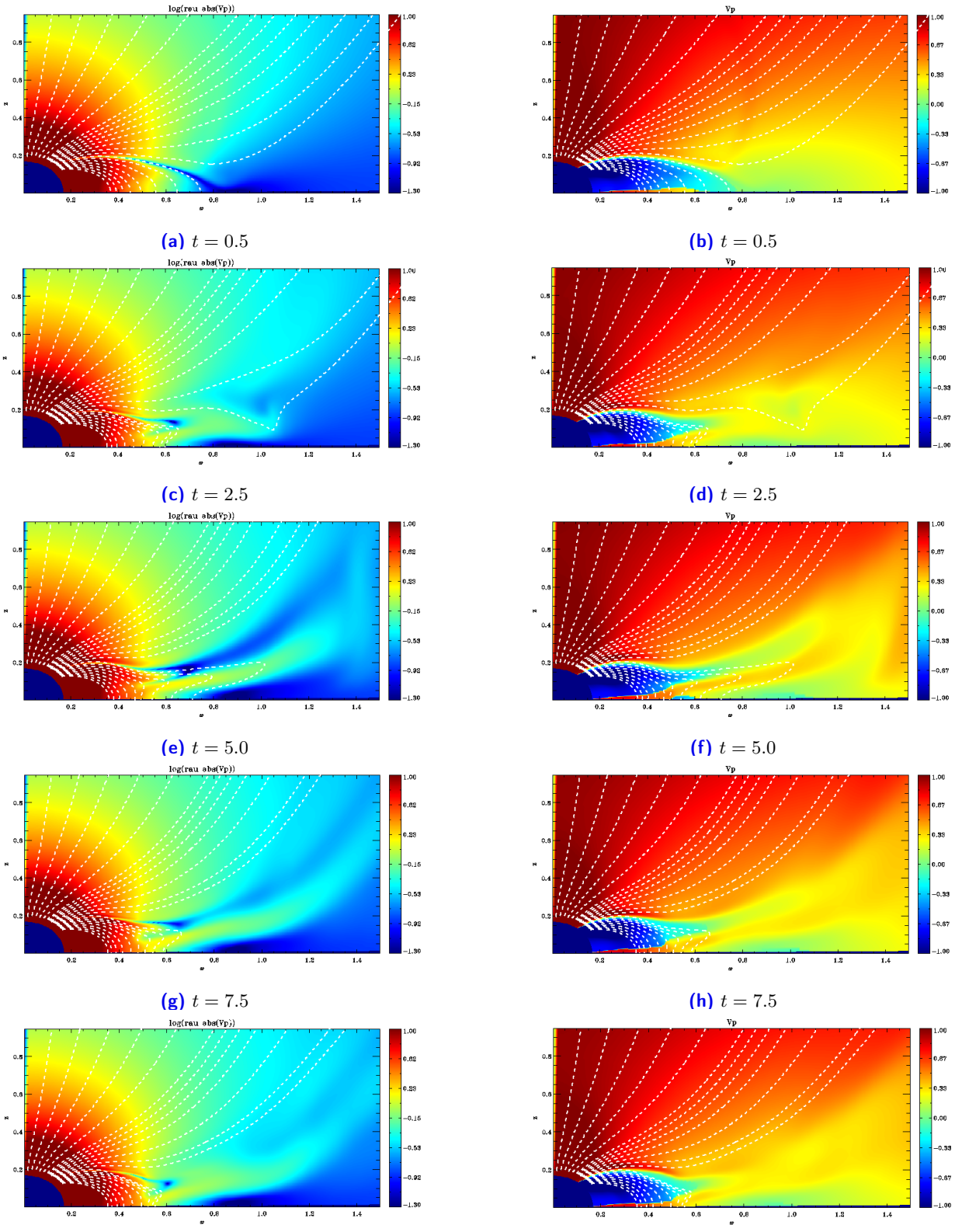

(a) $t = 0.5$ **(b)** $t = 0.5$

(c) $t = 2.5$ **(d)** $t = 2.5$

(e) $t = 5.0$ **(f)** $t = 5.0$

(g) $t = 7.5$ **(h)** $t = 7.5$

(i) $t = 20.0$ **(j)** $t = 20.0$

Figure 5.21: Mass flux $\log(\rho|V_p|)$ (first column) and poloidal velocity V_p (second column) plots for Test011. The white dashed lines represent the poloidal magnetic field lines.The x-axis corresponds to the radial distance ϖ, while the y-axis corresponds to height z.

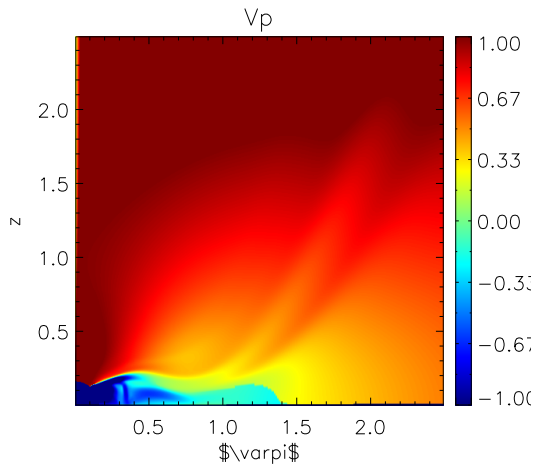

(a) $t = 7.5$

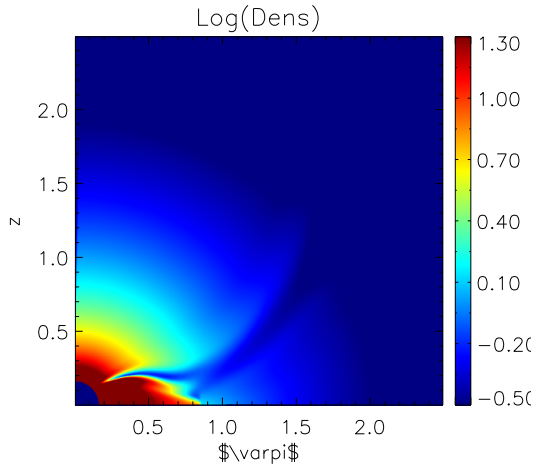

(b) $t = 7.5$

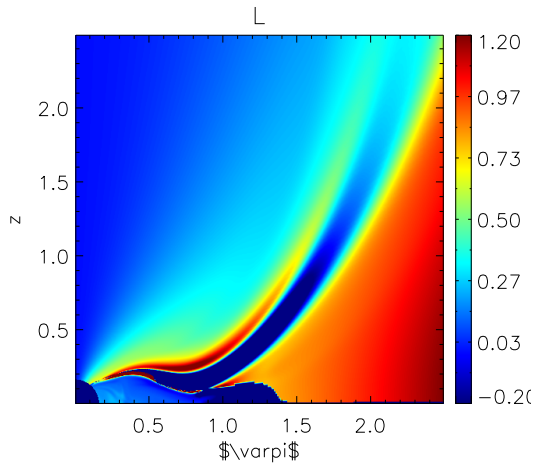

(c) $t = 7.5$

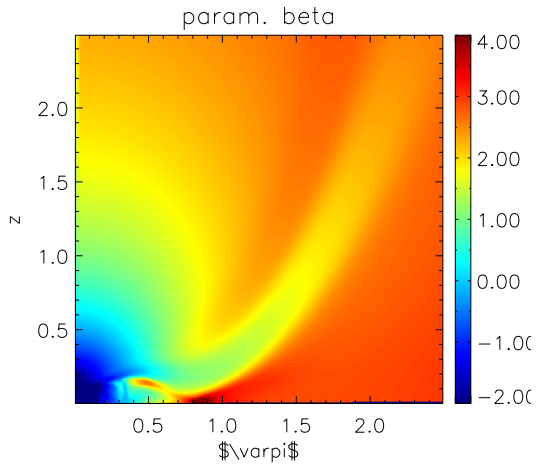

(d) $t = 7.5$

Figure 5.22: Plots of density $\log \rho$, total angular momentum L, poloidal velocity V_p and β-parameter for $t = 7.5$ for Test012. The x-axis corresponds to the radial distance ϖ, while the y-axis corresponds to height z.

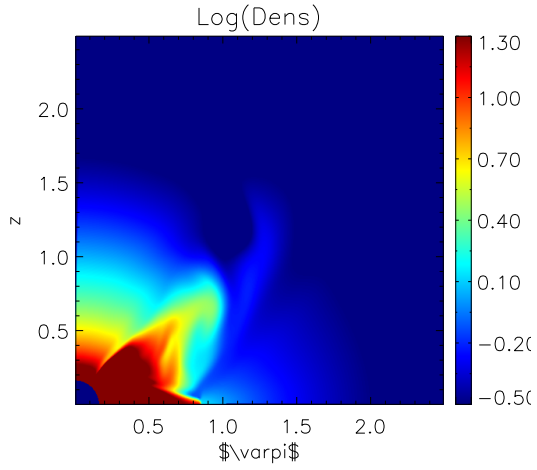

(a) $t = 2.5$

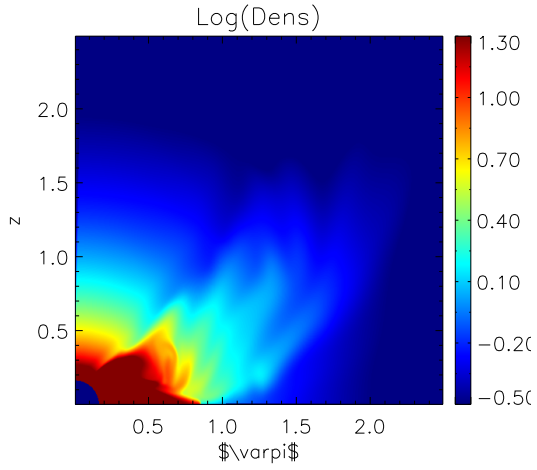

(b) $t = 10.0$

Figure 5.23: Plots of densitity $\log \rho$ for Test013. The x-axis corresponds to the radial distance ϖ, while the y-axis corresponds to height z.

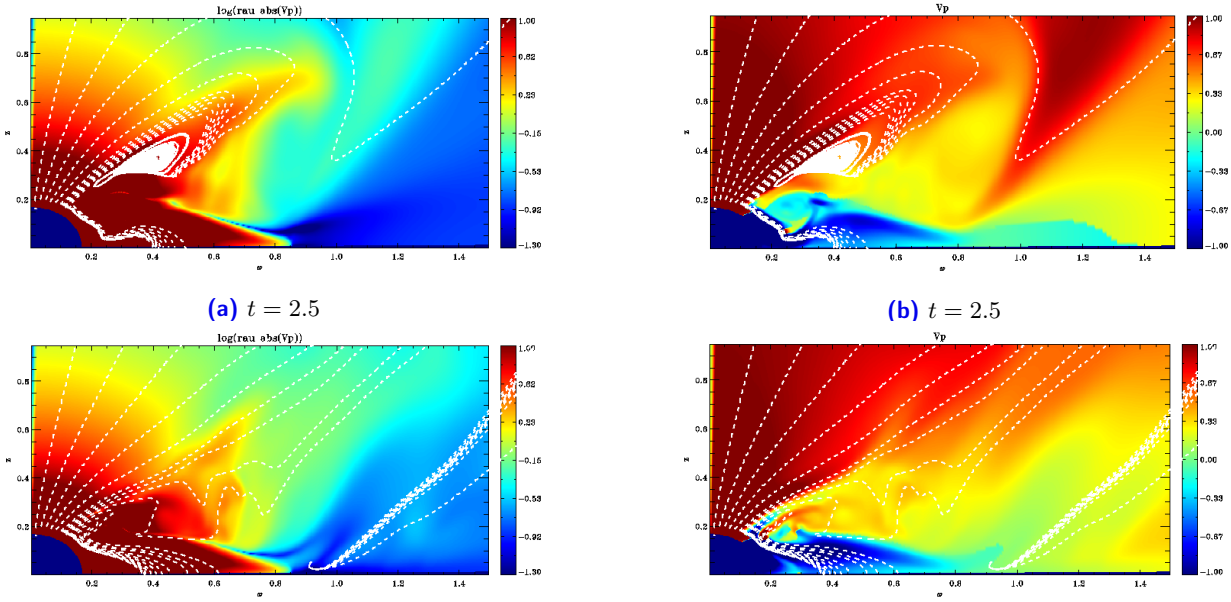

(a) $t = 2.5$ **(b)** $t = 2.5$

(c) $t = 10.0$ **(d)** $t = 10.0$

Figure 5.24: Mass flux $\log(\rho|V_p|)$ (first column) and poloidal velocity V_p (second column) plots for Test013. The white dashed lines represent the poloidal magnetic field lines. The x-axis corresponds to the radial distance ϖ, while the y-axis corresponds to height z.

Chapter 6

Linking observations and theory

6.1 PLUTO UNITS VS PHYSICAL UNITS

The performed PLUTO code simulations gave results in PLUTO units. In order to obtain the physical units, so it is possible to compare with observations made so far, we first need to get the conversion factors from a set of four parameters which control the model according to Sauty and Tsinganos (1994).

The δ parameter governs the non spherically symmetric distribution of the density with colatitude. For instance, when δ is positive the density increases by moving away from the polar axis. The reverse scenario takes place when δ assumes a negative value.

The κ parameter is responsible for controlling the non spherically symmetric distribution of the pressure. Assuming a positive value for this parameter implies that the gas pressure increases by moving away from the polar axis, contrary to the case in which κ would be negative.

The parameter responsible for controlling the rotation of the poloidal streamlines at the Alfvén surface is λ. Finally, ν is characterized by the gravitational field with acceleration given by

$$\mathbf{g} = -\frac{GM}{r^2}\hat{r} = -\frac{1}{2}\frac{V_*^2}{r_*}\frac{\nu^2}{R^2}\hat{r}, \tag{6.1}$$

where G is the gravitational constant and M the mass of the central object. The parameter ν represents the strength of the gravitational potential, from which the wind escapes. In other words, it gives the ratio between the escape velocity at the Alfvén surface to the polar speed there:

$$\nu^2 = \frac{2GM}{r_* V_*^2}. \tag{6.2}$$

The values for the parameters mentioned previously will be the ones determined by Sauty et al. (2011), within an analytical solution proposed for a model of low mass accreting T Tauri jets: $\delta = 0.0778$, $\kappa = 0.021$, $\nu = 1.5$ and $\lambda = 0.775$. Therefore, by assuming positive values for δ and κ, we are assuming that density and gas pressure increases by moving along the polar axis.

Also, considering R the ratio between the Alfvén radius r_* and the stellar radius r_0 and for which the Alfvén number is zero at the base of the jet, it is assumed

$$M(R) = 0 \Rightarrow r_* = 9.29 r_0. \tag{6.3}$$

In addition, the dimensionless magnetic flux considered for the last open streamline connected to the star α_{out} is equal to the minimum of the function R^2/G^2

$$\alpha_{\text{out}} = \min\left(\frac{R^2}{G^2}\right) = 0.989. \tag{6.4}$$

The mass loss rate, stellar mass and radius are given respectively by: $\dot{M} = 3.1 \times 10^{-9} M_\odot/yr$, $r_0 = 2.4 R_\odot$ and $M = 1.5 M_\odot$. These values are the same used in Sauty et al. (2011), typical of CTTS and close to the ones of RY Tau. Gathering all the parameters, is now possible to determine the conversion factors, namely for velocity, time and mass flux.

From equation (5.43), the poloidal velocity at the Alfvén radius on the polar axis can be rewritten as a function of the stellar mass and radius

$$V_* = \frac{V_{\text{esc}}}{\nu} = \sqrt{\frac{2GM}{9.29\nu^2 r_0}} \approx 106.8\ km/s. \tag{6.5}$$

PLUTO time $t = 1.0$ corresponds to the Alfvén time, given by $t = r_*/V_*$. By knowing r_* and V_* through equations (6.3) and (6.5), respectively, the conversion factor for time is given by:

$$t_{\text{phys}} = \frac{9.29 r_0}{\left(\frac{2GM}{9.29 r_0 \nu^2}\right)^{1/2}} \approx 1.45 \times 10^5 s \approx 1.68\ days. \tag{6.6}$$

From the mass loss rate per hemisphere given by equation (5.33), the density at the Alfvén radius can be determined through

$$\rho_* = \frac{3\delta\nu}{2\pi\left[(1+\delta\alpha_{\text{out}})^{3/2} - 1\sqrt{1603.53\ GMr_0^3}\right]}\dot{M}. \tag{6.7}$$

Finally, the conversion factor for the mass flux is given by the following expression

$$\pi\rho_* r_*^2 V_* = \frac{3\delta\dot{M}}{2\left[(1+\delta\alpha_{\text{out}})^{3/2} - 1\right]} \approx 3.08 \times 10^{-9}\ M_\odot/yr. \tag{6.8}$$

6.2 MASS FLUX RESULTS

From the data given by PLUTO simulations, mass flux estimations could be determined through and IDL script made by Véronique Cayatte. First, it is necessary to define two magnetic fieldlines (white dashed lines) in order to delimit a region for the stellar jet (blue lines) and another one for the magnetospheric region (yellow lines), as illustraded in figure 6.1 for the analytical solution. In the latest, the two magnetic

fieldlines are superimposed: the last open fieldline that delineates the jet region and a closed fieldline which defines the magnetospheric region. In this case, they are both connected to the X point at the extremity of the magnetosphere on the equatorial plane. Then, by integrating ρV_p along the coloured lines, it is possible to calculate the mass fluxes for the defined regions. MF1 refers to the region near the stellar surface, while MF2 is associated with a more distant region from the central object.

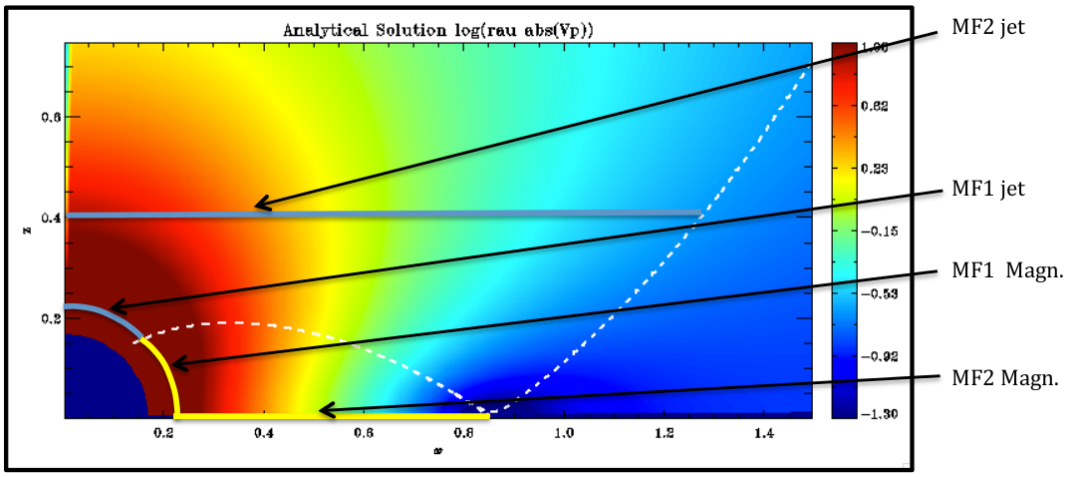

Figure 6.1: Representation of mass flux ($\log(\rho|V_p|)$) for the analytical solution proposed by Sauty et al. (2011). The white dashed lines represents the magnetic fieldlines. Picture courtesy: Véronique Cayatte.

In table 6.1 are shown the results for logarithmic mass fluxes in $M_\odot/yr$ for the ten best simulations computed and plotted in figure 6.2. In the latest figure, the pair of delimiting magnetic field lines (white dashed lines) were adjusted for each simulation according to the colatitude θ. The obtained values in PLUTO units were multiplied by the conversion factor given in equation (6.8) and then the logarithmic values were determined.

The results correspondent to accretion rates in the magnetosphere are between $10^{-8.35}$ and $10^{-7.25}$ $M_\odot/yr$, which are in agreement with the literature and the determined values through observations (see figure 4.5), where mass accretion rates are more frequent between 10^{-9} and 10^{-7} $M_\odot/yr$.

Although outflow rates were not determined through the spectra, the values obtained with the numerical simulations between $10^{-8.63}$ and $10^{-8.33}$ $M_\odot/yr$ are in conformity with the typical values found in the literature, 10^{-9} to 10^{-7} $M_\odot/yr$ according to Frank et al. (2014).

In the last column of table 6.1, are listed the outflow/inflow ratios for the MF1 region (closer to the stellar surface). As expected, the ratios are lower for the simulations with higher multiplying factors for density and velocity. This means that the increase in these last quantities is reflected in higher accretion rates as expected. In general, the mass flux for the jet region is about 4 to 79% the accretion flux (for Test013 and Test010, respectively). Matt and Pudritz (2008) suggested that the outflow/inflow ratio should be approximately $\leqslant 60\%$. Therefore, the simulations are quite reasonable and since the ratios are always less than the unity, it proves once again that accretion processes are dominant relatively to outflow mechanisms, but also the viability of these numerical simulations.

Test001_04 and Test001_05 differ only in the sign inversion of the toroidal magnetic field B_ϕ. As a

result of this single alteration, the latest simulation presents slightly higher values for accretion as well for ejection. Additionally, the sign inversion enabled the time computing extension of the remake of Test009_04 (Test009_07) from $t = 2.5$ to $t = 5.0$.

When the absolute values for the multiplying factors of the radial velocity component were increased from 1.0 to 1.5 in Test010 and Test011 respectively, the mass fluxes increased. As expected, when the multiplying factor for density is increased, accretion values increase and consequently the same is verified for ejection values not only in table 6.1, but also in figure 6.2. Therefore, numerical simulations are once again in agreement with the literature, suggesting that accretion feeds outflow mechanisms.

Another interesting aspect to mention concerns the time conversion factor from PLUTO to physical units, given by equation 6.6. If one a temporal PLUTO unit corresponds to 1.68 days, it means that, for the longest simulations, a stability configuration is reached (approximately) in one month. This time scale seems to be quite short, and should be discussed and rectified in a future work.

Table 6.1: Mass fluxes determined from the numerical simulations. The 1^{st} column identifies the simulation, while the 2^{nd} one refers to the last computed time. From the 3^{rd} to the 5^{th} column are mentioned the multiplying factors for the radial and polar components of the velocity and density ρ, respectively. The 6^{th} column indicates if the sign of toroidal magnetic field B_ϕ was reversed or not. From the 7^{th} to the 10^{th} columns are the logarithmic mass flux results in physical units ($M_\odot/yr$) for the correspondent times, determined in the jet and magnetospheric regions. In the 11^{th} column are listed the outflow/inflow ratios in the region close to the stellar surface (MF1).

		Multiplying factors				Jet		Magnetosphere		
Simulation ID	Time	V_r	V_θ	ρ	B_ϕ reversed?	log(MF1)	log(MF2)	log(MF1)	log(MF2)	$MF1_{Jet}/MF1_{Magn.}$
Test001_04	10.0	-1.0	-0.5	1	No	-8.47	-8.46	-8.34	-8.35	0.75
Test001_05	10.0	-1.0	-0.5	1	Yes	-8.47	-8.42	-8.14	-8.35	0.47
Test009_02	5.0	-2.0	-0.5	1	No	-8.51	-8.57	-8.01	-8.04	0.32
Test009_04	2.5	-2.0	-0.5	5	No	-8.47	-8.46	-7.44	-7.45	0.09
Test009_06	5.0	-2.0	-0.5	1	Yes	-8.49	-8.49	-8.04	-8.07	0.35
Test009_07	5.0	-2.0	-0.5	5	Yes	-8.47	-8.52	-7.42	-7.43	0.09
Test010	20.0	-1.0	-0.5	1	Yes	-8.45	-8.40	-8.34	-8.34	0.79
Test011	20.0	-1.5	-0.5	1	Yes	-8.49	-8.50	-8.15	-8.16	0.46
Test012	19.5	-1.5	-0.5	5	Yes	-8.42	-8.44	-7.60	-7.62	0.15
Test013	20.0	-2.0	-0.5	10	Yes	-8.63	-8.33	-7.25	-7.34	0.04

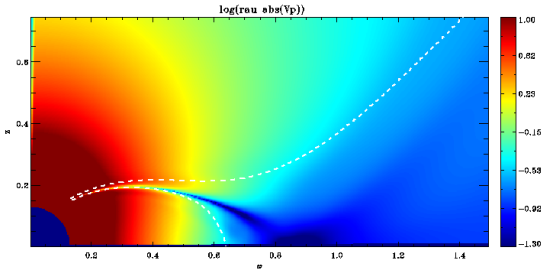

(a) Test001_04 at $t = 10.0$

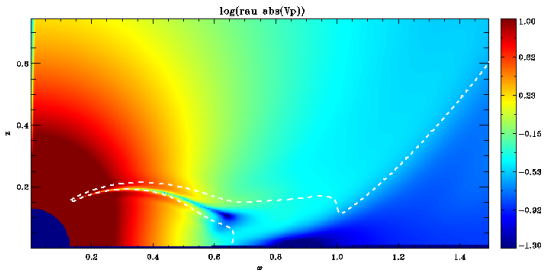

(b) Test001_05 at $t = 10.0$

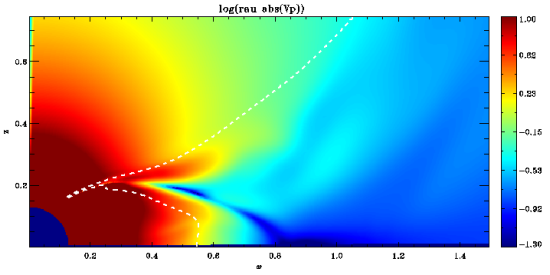

(c) Test009_02 at $t = 5.0$

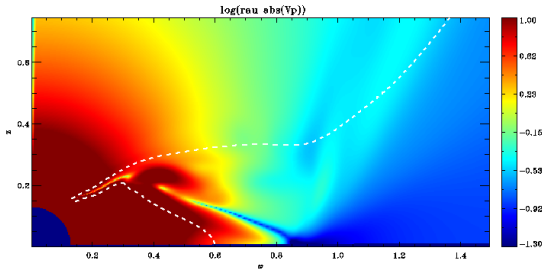

(d) Test009_04 at $t = 2.5$

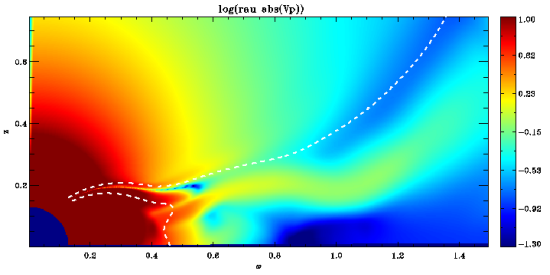

(e) Test009_06 at $t = 5.0$

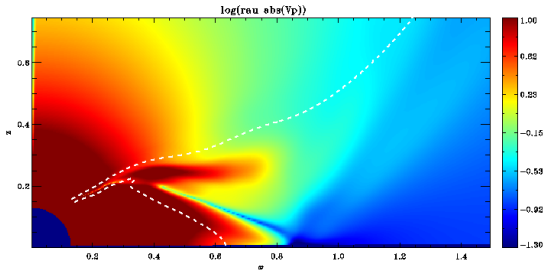

(f) Test009_07 at $t = 5.0$

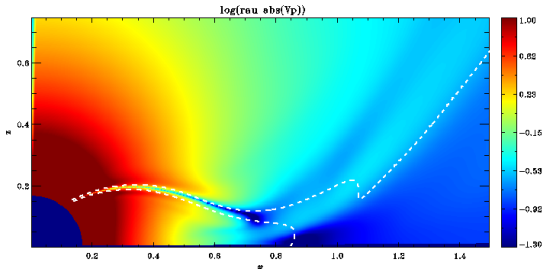

(g) Test010 at $t = 20.0$

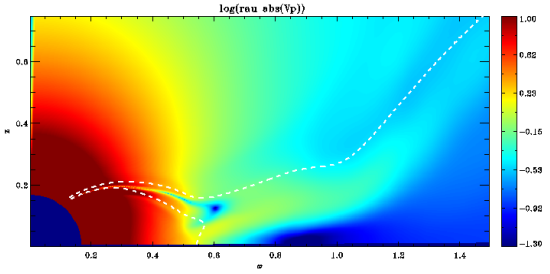

(h) Test011 at $t = 20.0$

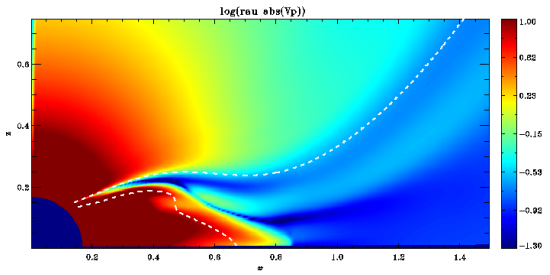

(i) Test012 at $t = 19.5$

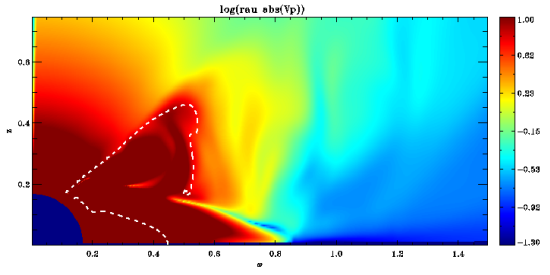

(j) Test013 at $t = 20.0$

Figure 6.2: Mass flux $\log(\rho|V_p|)$ plots for the final stage of Test001_04, Test001_05, Test009_02, Test009_04, Test009_06, Test009_07, Test010, Test011, Test012 and Test013. The white dashed lines represent the poloidal magnetic field lines used to determine the mass fluxes.

6.3 SIMULATIONS OVERALL

Taking all simulations into account, there are some main interesting results to mention. By increasing V_p with higher factors we also increase the system instabilities instead of just the mass flux, specially when considering factors higher than 2.0. On the other hand, if the poloidal velocity is multiplied by a factor smaller than -1.0, L and Ω values in the magnetosphere will be different from the analytical solution. Furthermore, this could lead to sharp gradients near the initial last connected fieldline, and be more pronounced for L if the density is increased by a factor higher than 1.0. The volumetric rate of thermal energy q along the field in the cooling function was adapted (2^{nd} new cooling) and applied inside and outside the magnetospheric region. By doing this, PLUTO is now able to deal with the differences between the analytical solution and the simulated ones.

Interestingly, there seems to be a certain specific combination of multiplying factors among the physical quantities, such that the simulations evolve with less instabilities and the outflow features are not destroyed along time. In other words, accretion processes seem to be steady (as stellar jets), unlike other simulations. Furthermore, in order to achieve more stable simulations, it seems that it is needed to increase density and velocity simultaneously. Otherwise, instabilities will be more pronounced.

Among the simulations were observed different outflow features namely: loops, streamers associated to sporadic X-winds, possible magnetospheric ejections and some helmet streamer perturbations. It was also possible to identify well defined accretion columns in the magnetosphere, in which the matter flows from the disk to the star. This was only possible due to the sign reverse of the poloidal velocity in the analytical solution.

The sporadic X-winds observed in the last four simulations seem to be time-dependent, contrasting with Zanni and Ferreira (2013) averaged simulations, which can lead to the incorrect idea that X-winds are a steady phenomenon. This features are also more pronounced when density is increased in Test012 and Test013 by a factor of 5 and 10, respectively.

Regarding instability features in sporadic X-winds, in figure 5.11 are shown good examples for Kelvin Helmoltz instabilities, similar to the waves observed in Saturn atmosphere (see figure 6.3). The latest occur when two fluids of different densities or different speeds flow by each other (Fox, 2011). In addition, instabilities seen in figure 5.17f could be associated with Rayleigh-Taylor instabilities. In the latest, light fluid pushes on a heavy fluid resulting in mushroom-like structures (Sharp, 1984).

It should be mentioned that the reverse of B_ϕ sign improved the solutions for Test001_05, Test009_06 and returned interesting results in the following simulations because it coincides with the change of sign of the poloidal electric current density. Ferreira and collaborators suggested that, although stellar winds are not able to carry themselves a large fraction of the ejected mass, it allows to carry the returning electric current needed to confine the outer disk wind. In other words, the electric circuit flows towards the star, enters in the disk at its inner edge and leaves it at the disk surface. According to Ferreira et al.

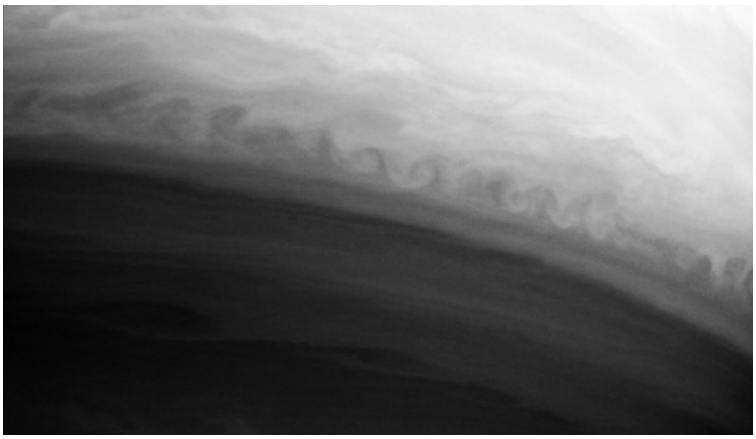

Figure 6.3: Kelvin Helmoltz instabilities in Saturn atmosphere. Image credit: NASA/Cassini.

(2006), this scenario leads to variable processes resulting from star-disk interaction if the X-winds have approximately the same mass loss flux as stellar jets.

To conclude, from Test001 to Test013 there is a clear evolution of the simulations in order to obtain an approximate replica of the observations made so far for YSOs. The presence of accretion/outflow features, jointly with acceptable mass flux rates and stable results, reinforce even further the credibility of the numerical simulations made.

Chapter 7

Conclusion

To begin with, through the empirical relation of Natta et al. (2004), it is possible to infer that, for the selected sample of CTTS, the computed mass accretion rates are more frequent between 10^{-9} to 10^{-8} $M_{\odot}/yr$. Despite some differences between the determined values with the literature, it should be taken into account several interfering and/or variable factors such as methods used (veiling, accretion luminosities, radiative transfer models, etc.), number of accretion columns unevenly spaced and inclined magnetospheres, for instance.

The majority of the profiles in the Hα line are asymmetric, double peaked and the line wings often extend near to ± 400 km/s, indicative of large-scale gas flows. The He I emission line analysis showed that free falling velocities for accreting material ranges between 300 and 500 km/s for both He I at $\lambda 5876$ and $\lambda 6678$. While for Hα $\lambda 6563$ the velocity peaks are mainly blueshifted, for He I $\lambda 5678$ and $\lambda 6678$ the highest frequency of velocity peaks is redshifted.

Through [OI] at $\lambda 6300$ and [SII] at $\lambda 6731$ forbidden emission lines, it was possible to identify a high-velocity component (HVC) and a low-velocity component (LVC). HVC is thought to have its origin in a fast, collimated jet characterized by low densities and high temperatures. On the other hand, LVC is thought to form in a cooler and denser region of smaller extent close to the star. From the spectral analysis, it was seen that the HVC of [OI] and [SII] have velocities ranging between $\sim [-344, -123]$ km/s and $\sim [-338, -116]$ km/s, respectively, where [OI] velocities are slightly higher relatively to [SII] line profiles. Concerning the LVC, velocities vary between $\sim [-50, -20]$ km/s for [OI] and $\sim [-60, -30]$ km/s for [SII].

Regarding the triple gaussing fitting (3GF) routine, fitted reasonably gaussian-like as well as asymmetric profiles. Emission profiles with more complex asymmetries, obliged the introduction of more constrains in order to make a proper fit. Nevertheless, the routine should be polished so it can fit more accurately narrow and broad components of emission profiles, as seen for He I, for instance.

The fitted central velocities are mainly blueshifted for Hα, within the range of $[-100, 0]$ km/s. In contrast, for He I $\lambda 5876$ and $\lambda 6678$, the adjusted velocities are redshifted between $[0, 50]$ km/s and seem

to be correlated, suggesting its origin in a post-shock region on the stellar surface.

As expected, Hα presents the highest intensities, followed by He I $\lambda5876$ and $\lambda6678$. Regarding the standard deviations, for Hα and He I $\lambda5876$ the highest dispersions are always for the gaussian responsible for adjusting the wings of the emission line. For He I $\lambda6678$, because the emission component is narrower than the absorption feature, the σ values are higher for the negative gaussian. As expected, Hα has the highest standard deviations due to its broad line emission. Clearly, He I $\lambda5876$ has a stronger emission than $\lambda6678$, and the latest seems to have broader absorption dips.

For the Hα line emission, typically intense for YSOs, both outflow and accretion processes can be detected in the spectra. Outflow is associated with intense blueshifted absorptions, while accretion is typically linked with asymmetric profiles, occasional redshifted absorptions, but also broad emission lines arising from the rapid infall of the gas. For He I, redshifted peaks and absorptions within IPC profiles and the presence of both broad and narrow components, evidence the typical signatures of magnetospheric infall.

Regarding the simulations made, besides the axisymmetric geometry assumption, time dependency and meridional self-similarity are useful strategies to achieve MHD numerical solutions for accretion and outflow mechanisms in YSOs through the Sauty and Tsinganos (1994) model.

Among the simulations were observed different outflow features such as loops, streamers associated to sporadic X-winds, possible magnetospheric ejections and helmet streamer perturbations. It was also possible to identify well defined accretion columns in the magnetosphere, in which the matter flows from the disk to the star.

Additionally, through the simulations made, X-winds evidence time dependent characteristics, as seen previously by other authors. The new achievement is that both stellar jet and accretion mechanisms seem to be steady unlike other simulations.

It was possible to achieve stable simulations with stable stellar winds and acceptable mass loss rates, as well as accretion rates. Although accretion was not expected for all simulations, the determined MF1 and MF2 results are in good agreement with observations. It was observed that to increase mass accretion rates, besides density, velocity needs also to be increased.

The accretion rates determined for the ten best simulations are between $10^{-8.4}$ and $10^{-7.2}$ $M_{\odot}/yr$, which are in agreement with the literature and the determined values through observations in chapter 4, where mass accretion rates are more recurrent between 10^{-9} and 10^{-7} $M_{\odot}/yr$. Regarding the outflow rates, the numerical simulations returned values between $10^{-8.6}$ and $10^{-8.3}$ $M_{\odot}/yr$, which are in conformity with the the literature: 10^{-9} to 10^{-7} $M_{\odot}/yr$ according to Frank et al. (2014).

The computed outflow/inflow ratios for the region closer to the stellar surface showed that the mass flux for the jet region is about 4 to 79% the accretion flux, among the then best simulations made. In general, accretion rates in the magnetosphere are always higher than the outflow rates determined in the jet regions, confirming the dominance of accretion over ejection processes, as seen previously in the

literature. The results prove that the performed numerical simulations are quite acceptable and able to match the observations.

7.1 FUTURE WORK

Taking all into account and due to the lack of time, there are several things that need to be done.

In order to simulations become gradually in agreement with observations, it could be tested more combinations of multiplying factors for more physical quantities and/or refine even better the cooling function used. Also, the parameters used in PLUTO simulations could be taken from the studied sample. More specifically, numerical simulations could be computed according to stellar radius and mass, so it could be possible to observe the main differences.

Additionally, it would be interesting to compare the made diagnostic line profiles with the ones obtained through radiative transfer models applied in MHD simulations. Furthermore, the intricate nature of the observed instabilities could be also studied in detail, as well as including a circumstellar dead zone in the simulations, so it could be even more close to the observations.

Regarding the observations, this part could be redirected for an individual analysis of the sampled stars and complemented with the study of forbidden line luminosities. To do so, photometry would be applied so that emission line fluxes and luminosities could be studied. Additionally, the determined mass accretion rates with Natta et al. (2004) empirical relationship could and should be compared with the ones obtained through veiling or other methods for the same sample.

Interestingly, in some cases where accretion is relevant, OI $\lambda 7772$ appears in absorption or even with an IPC profile. Although it was not seen a clear correlation between OI absorptions and accretion rates, a proper future analysis should take into account the star inclination as well as the corresponding fluxes/-luminosities.

Edwards et al. (1987) confirmed that the absorption features correspond to outflowing material due to the velocity coincidence between the blueshifted minimum at Hα and the blueshifted emission peaks in [OI] $\lambda 6300$ line. It would be interesting to determine the outflow velocity through simulations and then compare the values with the observed Hα and forbidden lines. For the latest, spectra must be corrected with a template of the same spectral class in order to correct properly the effects of rotation velocity and veiling.

Bibliography

Adams, F. C., Lada, C. J., and Shu, F. H. Spectral evolution of young stellar objects. *Astrophys. J.*, 312: 788–806, Jan. 1987. doi: 10.1086/164924.

Akeson, R. L., Boden, A. F., Monnier, J. D., Millan-Gabet, R., Beichman, C., Beletic, J., Calvet, N., Hartmann, L., Hillenbrand, L., Koresko, C., Sargent, A., and Tannirkulam, A. Keck Interferometer Observations of Classical and Weak-line T Tauri Stars. *Astrophys. J.*, 635:1173–1181, Dec. 2005. doi: 10.1086/497436.

Ambartsumian, V. A. *Stellar Evolution and Astrophysics*. Erevan, U.S.S.R., 1947.

Artemenko, S. A., Grankin, K. N., and Petrov, P. P. Rotation effects in classical T Tauri stars. *Astronomy Letters*, 38:783–792, Dec. 2012. doi: 10.1134/S1063773712110011.

Aschwanden, M. J. *Physics of the Solar Corona. An Introduction with Problems and Solutions (2nd edition)*. Dec. 2005.

Audard, M., Skinner, S. L., Smith, K. W., Güdel, M., and Pallavicini, R. High energy processes in young stars: Chandra X-Ray spectroscopy of HDE 283572, RY Tau, and LkCa 21. In Favata, F., Hussain, G. A. J., and Battrick, B., editors, *13th Cambridge Workshop on Cool Stars, Stellar Systems and the Sun*, volume 560 of *ESA Special Publication*, page 411, Mar. 2005.

Azevedo, R., Calvet, N., Hartmann, L., Folha, D. F. M., Gameiro, F., and Muzerolle, J. Calcium II infrared triplet line models in classical T Tauri stars. *Astron. Astrophys.*, 456:225–234, Sept. 2006. doi: 10.1051/0004-6361:20054315.

Basri, G. and Bertout, C. Accretion disks around T Tauri stars. II - Balmer emission. *Astrophys. J.*, 341: 340–358, June 1989. doi: 10.1086/167498.

Batalha, C. C., Stout-Batalha, N. M., Basri, G., and Terra, M. A. O. The Narrow Emission Lines of T Tauri Stars. *Astrophys. J. Suppl. Series*, 103:211, Mar. 1996. doi: 10.1086/192275.

Belenkaya, E., Khodachenko, M., and Alexeev, I. Alfvén radius: A key parameter for astrophysical magnetospheres. In Lammer, H. and Khodachenko, M., editors, *Characterizing Stellar and Exoplanetary*

Environments, volume 411 of *Astrophysics and Space Science Library*, pages 239–249. Springer International Publishing, 2015. ISBN 978-3-319-09748-0. doi: 10.1007/978-3-319-09749-7_12. URL http://dx.doi.org/10.1007/978-3-319-09749-7_12.

Bertout, C., Basri, G., and Bouvier, J. Accretion disks around T Tauri stars. *Astrophys. J.*, 330:350–373, July 1988. doi: 10.1086/166476.

Blandford, R. D. and Payne, D. G. Hydromagnetic flows from accretion discs and the production of radio jets. *Mon. Not. Roy. Astron. Soc.*, 199:883–903, June 1982.

Bouvier, J. and Bertout, C. Spots on T Tauri stars. *Astron. Astrophys.*, 211:99–114, Feb. 1989.

Bouvier, J., Covino, E., Kovo, O., Martin, E. L., Matthews, J. M., Terranegra, L., and Beck, S. C. COYOTES II: SPOT properties and the origin of photometric period variations in T Tauri stars. *Astron. Astrophys.*, 299:89, July 1995.

Bouvier, J., Grankin, K. N., Alencar, S. H. P., Dougados, C., Fernández, M., Basri, G., Batalha, C., Guenther, E., Ibrahimov, M. A., Magakian, T. Y., Melnikov, S. Y., Petrov, P. P., Rud, M. V., and Zapatero Osorio, M. R. Eclipses by circumstellar material in the T Tauri star AA Tau. II. Evidence for non-stationary magnetospheric accretion. *Astron. Astrophys.*, 409:169–192, Oct. 2003. doi: 10.1051/0004-6361:20030938.

Bouvier, J., Alencar, S. H. P., Harries, T. J., Johns-Krull, C. M., and Romanova, M. M. Magnetospheric Accretion in Classical T Tauri Stars. *Protostars and Planets V*, pages 479–494, 2007.

Bouvier, J., Matt, S. P., Mohanty, S., Scholz, A., Stassun, K. G., and Zanni, C. Angular Momentum Evolution of Young Low-Mass Stars and Brown Dwarfs: Observations and Theory. *Protostars and Planets VI*, pages 433–450, 2014. doi: 10.2458/azu_uapress_9780816531240-ch019.

Brown, J. M., Blake, G. A., Qi, C., Dullemond, C. P., and Wilner, D. J. LkHα 330: Evidence for Dust Clearing through Resolved Submillimeter Imaging. *Astrophys. J. Lett.*, 675:L109–L112, Mar. 2008. doi: 10.1086/533464.

Cabrit, S. The accretion-ejection connexion in T Tauri stars: jet models vs. observations. In Bouvier, J. and Appenzeller, I., editors, *IAU Symposium*, volume 243 of *IAU Symposium*, pages 203–214, May 2007. doi: 10.1017/S1743921307009568.

Cabrit, S., Edwards, S., Strom, S. E., and Strom, K. M. Forbidden-line emission and infrared excesses in T Tauri stars - Evidence for accretion-driven mass loss? *Astrophys. J.*, 354:687–700, May 1990. doi: 10.1086/168725.

Cai, M. J., Shang, H., Lin, H.-H., and Shu, F. H. X-Winds in Action. *Astrophys. J.*, 672:489–503, Jan. 2008. doi: 10.1086/523788.

Calvet, N., Muzerolle, J., Briceño, C., Hernández, J., Hartmann, L., Saucedo, J. L., and Gordon, K. D. The Mass Accretion Rates of Intermediate-Mass T Tauri Stars. *Astronom. J.*, 128:1294–1318, Sept. 2004. doi: 10.1086/422733.

Carmona, A., van den Ancker, M. E., Henning, T., Goto, M., Fedele, D., and Stecklum, B. A search for near-infrared molecular hydrogen emission in the CTTS LkHα 264 and the debris disk 49 Ceti. *Astron. Astrophys.*, 478:795–795, Feb. 2008. doi: 10.1051/0004-6361:20078536e.

Chubak, C. and Marcy, G. Accurate Radial Velocities of 2284 FGKM Stars and 127 Standards. In *American Astronomical Society Meeting Abstracts #217*, volume 43 of *Bulletin of the American Astronomical Society*, page 434.12, Jan. 2011.

Close, L. M., Dutrey, A., Roddier, F., Guilloteau, S., Roddier, C., Northcott, M., Ménard, F., Duvert, G., Graves, J. E., and Potter, D. Adaptive Optics Imaging of the Circumbinary Disk around the T Tauri Binary UY Aurigae: Estimates of the Binary Mass and Circumbinary Dust Grain Size Distribution. *Astrophys. J.*, 499:883–888, May 1998.

Cody, A. M. and Hillenbrand, L. A. Precision Photometric Monitoring of Very Low Mass σ Orionis Cluster Members: Variability and Rotation at a Few Myr. *Astrophys. J. Suppl. Series*, 191:389–422, Dec. 2010. doi: 10.1088/0067-0049/191/2/389.

Coffey, D., Bacciotti, F., and Podio, L. T Tauri Jet Physics Resolved Near the Launching Region with the Hubble Space Telescope. *Astrophys. J.*, 689:1112–1126, Dec. 2008. doi: 10.1086/592343.

Cohen, M. and Kuhi, L. V. Observational studies of pre-main-sequence evolution. *Astrophys. J. Suppl. Series*, 41:743–843, Dec. 1979. doi: 10.1086/190641.

Costigan, G., Scholz, A., Stelzer, B., Ray, T., Vink, J. S., and Mohanty, S. LAMP: the long-term accretion monitoring programme of T Tauri stars in Chamaeleon I. *Mon. Not. Roy. Astron. Soc.*, 427:1344–1362, Dec. 2012. doi: 10.1111/j.1365-2966.2012.22008.x.

Dougados, C., Cabrit, S., Lavalley, C., and Ménard, F. T Tauri stars microjets resolved by adaptive optics. *Astron. Astrophys.*, 357:L61–L64, May 2000.

Dougados, C., Cabrit, S., Ferreira, J., Pesenti, N., Garcia, P., and O'Brien, D. The Origin of Jets from Young Stars: MHD Disk Wind Models Confronted to Observations. *Astrophys. Spa. Sci.*, 292:643–650, Aug. 2004. doi: 10.1023/B:ASTR.0000045070.22924.8b.

Edwards, S., Cabrit, S., Strom, S. E., Heyer, I., Strom, K. M., and Anderson, E. Forbidden line and H-alpha profiles in T Tauri star spectra - A probe of anisotropic mass outflows and circumstellar disks. *Astrophys. J.*, 321:473–495, Oct. 1987. doi: 10.1086/165646.

Edwards, S., Hartigan, P., Ghandour, L., and Andrulis, C. Spectroscopic evidence for magnetospheric accretion in classical T Tauri stars. *Astronom. J.*, 108:1056–1070, Sept. 1994. doi: 10.1086/117134.

Fang, M., van Boekel, R., Wang, W., Carmona, A., Sicilia-Aguilar, A., and Henning, T. Star and protoplanetary disk properties in Orion's suburbs. *Astron. Astrophys.*, 504:461–489, Sept. 2009. doi: 10.1051/0004-6361/200912468.

Feigelson, E., Townsley, L., Güdel, M., and Stassun, K. X-Ray Properties of Young Stars and Stellar Clusters. *Protostars and Planets V*, pages 313–328, 2007.

Fernandez, M., Ortiz, E., Eiroa, C., and Miranda, L. F. Hα emission from pre-main sequence stars. *Astron. Astrophys. Suppl.*, 114:439, Dec. 1995.

Ferreira, J. Magnetically-driven jets from Keplerian accretion discs. *Astron. Astrophys.*, 319:340–359, Mar. 1997.

Ferreira, J. Braking down an accreting protostar: disc-locking, disc winds, stellar winds, X-winds and Magnetospheric Ejecta. In Hennebelle, P. and Charbonnel, C., editors, *EAS Publications Series*, volume 62 of *EAS Publications Series*, pages 169–225, Sept. 2013. doi: 10.1051/eas/1362006.

Ferreira, J. and Casse, F. Stationary Accretion Disks Launching Super-fast-magnetosonic Magnetohydrodynamic Jets. *Astrophys. J. Lett.*, 601:L139–L142, Feb. 2004. doi: 10.1086/381804.

Ferreira, J. and Pelletier, G. Magnetized accretion-ejection structures. 1. General statements. *Astron. Astrophys.*, 276:625, Sept. 1993.

Ferreira, J., Dougados, C., and Cabrit, S. Which jet launching mechanism(s) in T Tauri stars? *Astron. Astrophys.*, 453:785–796, July 2006. doi: 10.1051/0004-6361:20054231.

Finkenzeller, U. and Mundt, R. The Herbig Ae/Be stars associated with nebulosity. *Astron. Astrophys. Suppl.*, 55:109–141, Jan. 1984.

Fox, K. C. Nasa's solar dynamics observatory catches "surfer" waves on the sun. NASA-The Sun-Earth Connection: Heliophysics, June 2011. URL http://www.nasa.gov/mission_pages/sunearth/news/sun-surfing.html#.VfV2urNVK1F.

Frank, A., Ray, T. P., Cabrit, S., Hartigan, P., Arce, H. G., Bacciotti, F., Bally, J., Benisty, M., Eislöffel, J., Güdel, M., Lebedev, S., Nisini, B., and Raga, A. Jets and Outflows from Star to Cloud: Observations Confront Theory. *Protostars and Planets VI*, pages 451–474, 2014. doi: 10.2458/azu_uapress_9780816531240-ch020.

Gahm, G. F., Petrov, P. P., and Stempels, H. C. Close binarity in CTTS. In Favata, F., Hussain, G. A. J., and Battrick, B., editors, *13th Cambridge Workshop on Cool Stars, Stellar Systems and the Sun*, volume 560 of *ESA Special Publication*, page 563, Mar. 2005.

Gallet, F. and Bouvier, J. Improved angular momentum evolution model for solar-like stars. *Astron. Astrophys.*, 556:A36, Aug. 2013. doi: 10.1051/0004-6361/201321302.

Ghosh, P. and Lamb, F. K. Accretion by rotating magnetic neutron stars. II - Radial and vertical structure of the transition zone in disk accretion. *Astrophys. J.*, 232:259–276, Aug. 1979. doi: 10.1086/157285.

Gontcharov, G. A. Pulkovo Compilation of Radial Velocities for 35 495 Hipparcos stars in a common system. *Astronomy Letters*, 32:759–771, Nov. 2006. doi: 10.1134/S1063773706110065.

Gramajo, L. V., Rodón, J. A., and Gómez, M. Spectral Energy Distribution Analysis of Class I and Class II FU Orionis Stars. *Astronom. J.*, 147:140, June 2014. doi: 10.1088/0004-6256/147/6/140.

Grankin, K. N., Melnikov, S. Y., Bouvier, J., Herbst, W., and Shevchenko, V. S. Results of the ROTOR-program. I. The long-term photometric variability of classical T Tauri stars. *Astron. Astrophys.*, 461: 183–195, Jan. 2007. doi: 10.1051/0004-6361:20065489.

Gregory, S. G., Donati, J.-F., Morin, J., Hussain, G. A. J., Mayne, N. J., Hillenbrand, L. A., and Jardine, M. Can We Predict the Global Magnetic Topology of a Pre-main-sequence Star from Its Position in the Hertzsprung-Russell Diagram? *Astrophys. J.*, 755:97, Aug. 2012. doi: 10.1088/0004-637X/755/2/97.

Gullbring, E., Hartmann, L., Briceño, C., and Calvet, N. Disk Accretion Rates for T Tauri Stars. *Astrophys. J.*, 492:323–341, Jan. 1998. doi: 10.1086/305032.

Hamann, F. and Persson, S. E. Emission-line studies of young stars. I - The T Tauri stars. II - The Herbig Ae/Be stars. *Astrophys. J. Suppl. Series*, 82:247–283, Sept. 1992. doi: 10.1086/191715.

Hartigan, P., Edwards, S., and Ghandour, L. Disk Accretion and Mass Loss from Young Stars. *Astrophys. J.*, 452:736, Oct. 1995. doi: 10.1086/176344.

Hartigan, P., Edwards, S., and Pierson, R. Going Slitless: Images of Forbidden-Line Emission Regions of Classical T Tauri Stars Observed with the Hubble Space Telescope. *Astrophys. J.*, 609:261–276, July 2004. doi: 10.1086/386317.

Hartmann, L. *Accretion Processes in Star Formation: Second Edition*. Cambridge University Press, 2009.

Hartmann, L. and Stauffer, J. R. Additional measurements of pre-main-sequence stellar rotation. *Astronom. J.*, 97:873–880, Mar. 1989. doi: 10.1086/115033.

Hartmann, L., Hewett, R., Stahler, S., and Mathieu, R. D. Rotational and radial velocities of T Tauri stars. *Astrophys. J.*, 309:275–293, Oct. 1986. doi: 10.1086/164599.

Hartmann, L., Hewett, R., and Calvet, N. Magnetospheric accretion models for T Tauri stars. 1: Balmer line profiles without rotation. *Astrophys. J.*, 426:669–687, May 1994. doi: 10.1086/174104.

Herbig, G. H. The properties and problems of T Tauri stars and related objects. *Advances in Astronomy and Astrophysics*, 1:47–103, 1962.

Herbig, G. H. Introductory Remarks. *Memoires of the Societe Royale des Sciences de Liege*, 19:13, 1970.

Herbig, G. H. Radial velocities and spectral types of T Tauri stars. *Astrophys. J.*, 214:747–758, June 1977. doi: 10.1086/155304.

Herbig, G. H. and Bell, K. R. *Third Catalog of Emission-Line Stars of the Orion Population : 3 : 1988*. 1988.

Herbst, W. and Shevchenko, V. S. A Photometric Catalog of Herbig AE/BE Stars and Discussion of the Nature and Cause of the Variations of UX Orionis Stars. *Astronom. J.*, 118:1043–1060, Aug. 1999. doi: 10.1086/300966.

Herbst, W., Herbst, D. K., Grossman, E. J., and Weinstein, D. Catalogue of UBVRI photometry of T Tauri stars and analysis of the causes of their variability. *Astronom. J.*, 108:1906–1923, Nov. 1994. doi: 10.1086/117204.

Herbst, W., Bailer-Jones, C. A. L., and Mundt, R. The Mass Dependence of Stellar Rotation in the Orion Nebula Cluster. *Astrophys. J. Lett.*, 554:L197–L200, June 2001. doi: 10.1086/321706.

Herczeg, G. J. and Hillenbrand, L. A. UV Excess Measures of Accretion onto Young Very Low Mass Stars and Brown Dwarfs. *Astrophys. J.*, 681:594–625, July 2008. doi: 10.1086/586728.

Herczeg, G. J. and Hillenbrand, L. A. An Optical Spectroscopic Study of T Tauri Stars. I. Photospheric Properties. *Astrophys. J.*, 786:97, May 2014. doi: 10.1088/0004-637X/786/2/97.

Hirth, G. A., Mundt, R., and Solf, J. Jet flows and disk winds from T Tauri stars: the case of CW Tau. *Astron. Astrophys.*, 285:929–942, May 1994a.

Hirth, G. A., Mundt, R., Solf, J., and Ray, T. P. Asymmetries in bipolar jets from young stars. *Astrophys. J. Lett.*, 427:L99–L102, June 1994b. doi: 10.1086/187374.

Hirth, G. A., Mundt, R., and Solf, J. A Long-Slit Spectroscopic Survey of Forbidden Emission Lines in T Tauri Stars. In Beckwith, S., Staude, J., Quetz, A., and Natta, A., editors, *Disks and Outflows Around Young Stars*, volume 465 of *Lecture Notes in Physics, Berlin Springer Verlag*, page 609, 1996.

Isella, A., Carpenter, J. M., and Sargent, A. I. Investigating Planet Formation in Circumstellar Disks: CARMA Observations of Ry Tau and Dg Tau. *Astrophys. J.*, 714:1746–1761, May 2010. doi: 10.1088/0004-637X/714/2/1746.

Johns, C. M. and Basri, G. The Line Profile Variability of SU Aurigae. *Astrophys. J.*, 449:341, Aug. 1995. doi: 10.1086/176059.

Johns-Krull, C. M., Valenti, J. A., Hatzes, A. P., and Kanaan, A. Spectropolarimetry of Magnetospheric Accretion on the Classical T Tauri Star BP Tauri. *Astrophys. J. Lett.*, 510:L41–L44, Jan. 1999. doi: 10.1086/311802.

Joy, A. H. Spectral Criteria in the Classification of Variable Stars. *Pub. Astron. Soc. Pac.*, 54:15, Feb. 1942. doi: 10.1086/125386.

Joy, A. H. T Tauri Variable Stars. *Astrophys. J.*, 102:168, Sept. 1945. doi: 10.1086/144749.

Joy, A. H. Bright-Line Stars among the Taurus Dark Clouds. *Astrophys. J.*, 110:424, Nov. 1949. doi: 10.1086/145217.

Koenigl, A. Disk accretion onto magnetic T Tauri stars. *Astrophys. J. Lett.*, 370:L39–L43, Mar. 1991. doi: 10.1086/185972.

Kwan, J. and Tademaru, E. Jets from T Tauri stars - Spectroscopic evidence and collimation mechanism. *Astrophys. J. Lett.*, 332:L41–L44, Sept. 1988. doi: 10.1086/185262.

Lada, C. J. and Wilking, B. A. The nature of the embedded population in the Rho Ophiuchi dark cloud - Mid-infrared observations. *Astrophys. J.*, 287:610–621, Dec. 1984. doi: 10.1086/162719.

Levreault, R. M. Molecular outflows and mass loss in the pre-main-sequence stars. *Astrophys. J.*, 330: 897–910, July 1988. doi: 10.1086/166520.

Lin, D. N. C., Bodenheimer, P., and Richardson, D. C. Orbital migration of the planetary companion of 51 Pegasi to its present location. *Nature*, 380:606–607, Apr. 1996. doi: 10.1038/380606a0.

Low, B. C. and Tsinganos, K. Steady hydromagnetic flows in open magnetic fields. I - A class of analytic solutions. *Astrophys. J.*, 302:163–187, Mar. 1986. doi: 10.1086/163980.

Lynden-Bell, D. and Pringle, J. E. The evolution of viscous discs and the origin of the nebular variables. *Mon. Not. Roy. Astron. Soc.*, 168:603–637, Sept. 1974.

Martín, E. L., Magazzù, A., Delfosse, X., and Mathieu, R. D. The pre-main sequence spectroscopic binary UZ Tau East: Improved orbital parameters and accretion phase dependence. *Astron. Astrophys.*, 429: 939–943, Jan. 2005. doi: 10.1051/0004-6361:20041724.

Mathieu, R. D., Stassun, K., Basri, G., Jensen, E. L. N., Johns-Krull, C. M., Valenti, J. A., and Hartmann, L. W. The Classical T Tauri Spectroscopic Binary DQ Tau.I.Orbital Elements and Light Curves. *Astronom. J.*, 113:1841, May 1997. doi: 10.1086/118395.

Matt, S. and Pudritz, R. E. Accretion-powered Stellar Winds as a Solution to the Stellar Angular Momentum Problem. *Astrophys. J. Lett.*, 632:L135–L138, Oct. 2005a. doi: 10.1086/498066.

Matt, S. and Pudritz, R. E. The spin of accreting stars: dependence on magnetic coupling to the disc. *Mon. Not. Roy. Astron. Soc.*, 356:167–182, Jan. 2005b. doi: 10.1111/j.1365-2966.2004.08431.x.

Matt, S. and Pudritz, R. E. Accretion-powered Stellar Winds. II. Numerical Solutions for Stellar Wind Torques. *Astrophys. J.*, 678:1109–1118, May 2008. doi: 10.1086/533428.

Melnikov, S. Y., Eislöffel, J., Bacciotti, F., Woitas, J., and Ray, T. P. HST/STIS observations of the RW Aurigae bipolar jet: mapping the physical parameters close to the source. *Astron. Astrophys.*, 506: 763–777, Nov. 2009. doi: 10.1051/0004-6361/200811567.

Michel, F. C. Relativistic Stellar-Wind Torques. *Astrophys. J.*, 158:727, Nov. 1969. doi: 10.1086/150233.

Mignone, A., Bodo, G., Massaglia, S., Matsakos, T., Tesileanu, O., Zanni, C., and Ferrari, A. PLUTO: A Numerical Code for Computational Astrophysics. *Astrophys. J. Suppl. Series*, 170:228–242, May 2007. doi: 10.1086/513316.

Mihalas, D. and Conti, P. S. Some speculations concerning the significance of Beals's Type III P Cygni line profiles. *Astrophys. J.*, 235:515–518, Jan. 1980. doi: 10.1086/157654.

Mundt, R. Flows and Jets from Young Stars. In Dupree, A. K. and Lago, M. T. V. T., editors, *NATO Advanced Science Institutes (ASI) Series C*, volume 241 of *NATO Advanced Science Institutes (ASI) Series C*, page 257, 1988.

Muzerolle, J., Hartmann, L., and Calvet, N. A Brgamma Probe of Disk Accretion in T Tauri Stars and Embedded Young Stellar Objects. *Astronom. J.*, 116:2965–2974, Dec. 1998a. doi: 10.1086/300636.

Muzerolle, J., Hartmann, L., and Calvet, N. Emission-Line Diagnostics of T Tauri Magnetospheric Accretion. I. Line Profile Observations. *Astronom. J.*, 116:455–468, July 1998b. doi: 10.1086/300428.

Muzerolle, J., Calvet, N., and Hartmann, L. Emission-Line Diagnostics of T Tauri Magnetospheric Accretion. II. Improved Model Tests and Insights into Accretion Physics. *Astrophys. J.*, 550:944–961, Apr. 2001. doi: 10.1086/319779.

Muzerolle, J., Hillenbrand, L., Calvet, N., Briceño, C., and Hartmann, L. Accretion in Young Stellar/Substellar Objects. *Astrophys. J.*, 592:266–281, July 2003. doi: 10.1086/375704.

Natta, A., Testi, L., Muzerolle, J., Randich, S., Comerón, F., and Persi, P. Accretion in brown dwarfs: An infrared view. *Astron. Astrophys.*, 424:603–612, Sept. 2004. doi: 10.1051/0004-6361:20040356.

Nerney, S. F. and Suess, S. T. Restricted three-dimensional stellar wind modeling. I - Polytropic case. *Astrophys. J.*, 196:837–847, Mar. 1975. doi: 10.1086/153474.

Ostriker, E. C. and Shu, F. H. Magnetocentrifugally Driven Flows from Young Stars and Disks. IV. The Accretion Funnel and Dead Zone. *Astrophys. J.*, 447:813, July 1995. doi: 10.1086/175920.

Parker, E. N. *Interplanetary dynamical processes.* 1963.

Petrov, P. T tauri stars. *Astrophysics*, 46(4):506–529, 2003. ISSN 0571-7256. doi: 10.1023/B:ASYS.0000003267.35552.f7. URL http://dx.doi.org/10.1023/B%3AASYS.0000003267.35552.f7.

Petrov, P., Shcherbakov, A., and -Scherbakov, A. Observational data indicating existence of magnetic field in T Tau-type stars. In Kharadze, E. K., editor, *Stars and Galaxies from Observational Points of View*, pages 163–165, 1976.

Petrov, P. P., Gahm, G. F., Gameiro, J. F., Duemmler, R., Ilyin, I. V., Laakkonen, T., Lago, M. T. V. T., and Tuominen, I. Non-axisymmetric accretion on the classical TTS RW Aur A. *Astron. Astrophys.*, 369:993–1008, Apr. 2001. doi: 10.1051/0004-6361:20010203.

Petrov, P. P., Kurosawa, R., Romanova, M. M., Gameiro, J. F., Fernandez, M., Babina, E. V., and Artemenko, S. A. Facing the wind of the pre-FUor V1331 Cyg. *Mon. Not. Roy. Astron. Soc.*, 442:3643–3652, Aug. 2014. doi: 10.1093/mnras/stu1131.

Podio, L., Eislöffel, J., Melnikov, S., Hodapp, K. W., and Bacciotti, F. Tracing kinematical and physical asymmetries in the jet from DG Tauri B. *Astron. Astrophys.*, 527:A13, Mar. 2011. doi: 10.1051/0004-6361/201016049.

Priest, E. *Solar Magnetohydrodynamics*. Geophysics and Astrophysics Monographs. Springer Netherlands, 1984. ISBN 9789027718334. URL https://books.google.pt/books?id=sZylLdvm7lMC.

Ratzka, T. High spatial resolution observations of the T Tau system: II. Interferometry in the mid-infrared. *Journal of Physics Conference Series*, 131(1):012029, Oct. 2008. doi: 10.1088/1742-6596/131/1/012029.

Reipurth, B., Pedrosa, A., and Lago, M. T. V. T. Hα emission in pre-main sequence stars. I. an atlas of line profiles. *Astron. Astrophys. Suppl.*, 120:229–256, Dec. 1996.

Rice, E. L., Prato, L., and McLean, I. S. An Association in the Aquila Star-forming Region: High-Resolution Infrared Spectroscopy of T Tauri Stars. *Astrophys. J.*, 647:432–443, Aug. 2006. doi: 10.1086/505326.

Romanova, M. M., Ustyugova, G. V., Koldoba, A. V., and Lovelace, R. V. E. Launching of conical winds and axial jets from the disc-magnetosphere boundary: axisymmetric and 3D simulations. *Mon. Not. Roy. Astron. Soc.*, 399:1802–1828, Nov. 2009. doi: 10.1111/j.1365-2966.2009.15413.x.

Sakurai, T. Magnetic stellar winds - A 2-D generalization of the Weber-Davis model. *Astron. Astrophys.*, 152:121–129, Nov. 1985.

Sauty, C. and Tsinganos, K. Nonradial and nonpolytropic astrophysical outflows III. A criterion for the transition from jets to winds. *Astron. Astrophys.*, 287:893–926, July 1994.

Sauty, C., Tsinganos, K., and Trussoni, E. M.H.D. Models for Stellar Winds. *Astrophys. Spa. Sci.*, 261: 151–160, 1998. doi: 10.1023/A:1002051122157.

Sauty, C., Trussoni, E., and Tsinganos, K. Nonradial and nonpolytropic astrophysical outflows. VI. Overpressured winds and jets. *Astron. Astrophys.*, 421:797–809, July 2004. doi: 10.1051/0004-6361:20035790.

Sauty, C., Meliani, Z., Lima, J. J. G., Tsinganos, K., Cayatte, V., and Globus, N. Nonradial and non-polytropic astrophysical outflows. IX. Modeling T Tauri jets with a low mass-accretion rate. *Astron. Astrophys.*, 533:A46, Sept. 2011. doi: 10.1051/0004-6361/201116519.

Schwartz, R. D. Herbig-Haro objects. *Annual Rev. Astronom. Astrophys.*, 21:209–237, 1983. doi: 10.1146/annurev.aa.21.090183.001233.

Sharp, D. H. An overview of Rayleigh-Taylor instability. *Physica D Nonlinear Phenomena*, 12:3, July 1984. doi: 10.1016/0167-2789(84)90510-4.

Shu, F., Najita, J., Ostriker, E., Wilkin, F., Ruden, S., and Lizano, S. Magnetocentrifugally driven flows from young stars and disks. 1: A generalized model. *Astrophys. J.*, 429:781–796, July 1994. doi: 10.1086/174363.

Shu, F. H., Lizano, S., Ruden, S. P., and Najita, J. Mass loss from rapidly rotating magnetic protostars. *Astrophys. J. Lett.*, 328:L19–L23, May 1988. doi: 10.1086/185152.

Shu, F. H., Najita, J., Ostriker, E. C., and Shang, H. Magnetocentrifugally Driven Flows from Young Stars and Disks. V. Asymptotic Collimation into Jets. *Astrophys. J. Lett.*, 455:L155, Dec. 1995. doi: 10.1086/309838.

Stahler, S. W. and Palla, F. *The Formation of Stars*. 2005.

Suess, S. T. Three-dimensional solar wind. *J. Geophys. Res.*, 77:567, 1972. doi: 10.1029/JA077i004p00567.

Tobin, J. J., Hartmann, L., Furesz, G., Mateo, M., and Megeath, S. T. Kinematics of the Orion Nebula Cluster: Velocity Substructure and Spectroscopic Binaries. *Astrophys. J.*, 697:1103, June 2009. doi: 10.1088/0004-637X/697/2/1103.

Torres, C. A. O., Quast, G. R., da Silva, L., de La Reza, R., Melo, C. H. F., and Sterzik, M. Search for associations containing young stars (SACY). I. Sample and searching method. *Astron. Astrophys.*, 460:695–708, Dec. 2006. doi: 10.1051/0004-6361:20065602.

Tsinganos, K. Theory of MHD Jets and Outflows. In Ferreira, J., Dougados, C., and Whelan, E., editors, *Lecture Notes in Physics, Berlin Springer Verlag*, volume 723 of *Lecture Notes in Physics, Berlin Springer Verlag*, page 117, 2007.

Tsinganos, K. and Low, B. C. Steady hydromagnetic flows in open magnetic fields. II - Global flows with static zones. *Astrophys. J.*, 342:1028–1048, July 1989. doi: 10.1086/167660.

Tsinganos, K. and Trussoni, E. Analytical studies of collimated winds. II - Topologies of 2-D helicoidal MHD solutions. *Astron. Astrophys.*, 249:156–172, Sept. 1991.

Tsinganos, K. C. Magnetohydrodynamic equilibrium. II - General integrals of the equations with one ignorable coordinate. *Astrophys. J.*, 252:775–790, Jan. 1982. doi: 10.1086/159600.

Uchida, Y. and Shibata, K. Magnetodynamical acceleration of CO and optical bipolar flows from the region of star formation. *Pub. Astron. Soc. Japan*, 37:515–535, 1985.

Valenti, J. A., Basri, G., and Johns, C. M. T Tauri stars in blue. *Astronom. J.*, 106:2024–2050, Nov. 1993. doi: 10.1086/116783.

Vlahakis, N. and Tsinganos, K. Systematic construction of exact magnetohydrodynamic models for astrophysical winds and jets. *Mon. Not. Roy. Astron. Soc.*, 298:777–789, Aug. 1998. doi: 10.1046/j.1365-8711.1998.01660.x.

Weber, E. J. and Davis, Jr., L. The Angular Momentum of the Solar Wind. *Astrophys. J.*, 148:217–227, Apr. 1967. doi: 10.1086/149138.

White, R. J. and Basri, G. Very Low Mass Stars and Brown Dwarfs in Taurus-Auriga. *Astrophys. J.*, 582:1109–1122, Jan. 2003. doi: 10.1086/344673.

Woitas, J., Ray, T. P., Bacciotti, F., Davis, C. J., and Eislöffel, J. Hubble Space Telescope Space Telescope Imaging Spectrograph Observations of the Bipolar Jet from RW Aurigae: Tracing Outflow Asymmetries Close to the Source. *Astrophys. J.*, 580:336–342, Nov. 2002. doi: 10.1086/343124.

Zanni, C. and Ferreira, J. Observational Limits on the Spin-down Torque of Accretion Powered Stellar Winds. *Astrophys. J. Lett.*, 727:L22, Jan. 2011. doi: 10.1088/2041-8205/727/1/L22.

Zanni, C. and Ferreira, J. MHD simulations of accretion onto a dipolar magnetosphere. II. Magnetospheric ejections and stellar spin-down. *Astron. Astrophys.*, 550:A99, Feb. 2013. doi: 10.1051/0004-6361/201220168.

Appendix A

Triple gaussian fitting figures for Hα 6563, He I $\lambda\lambda$5876 and 6678

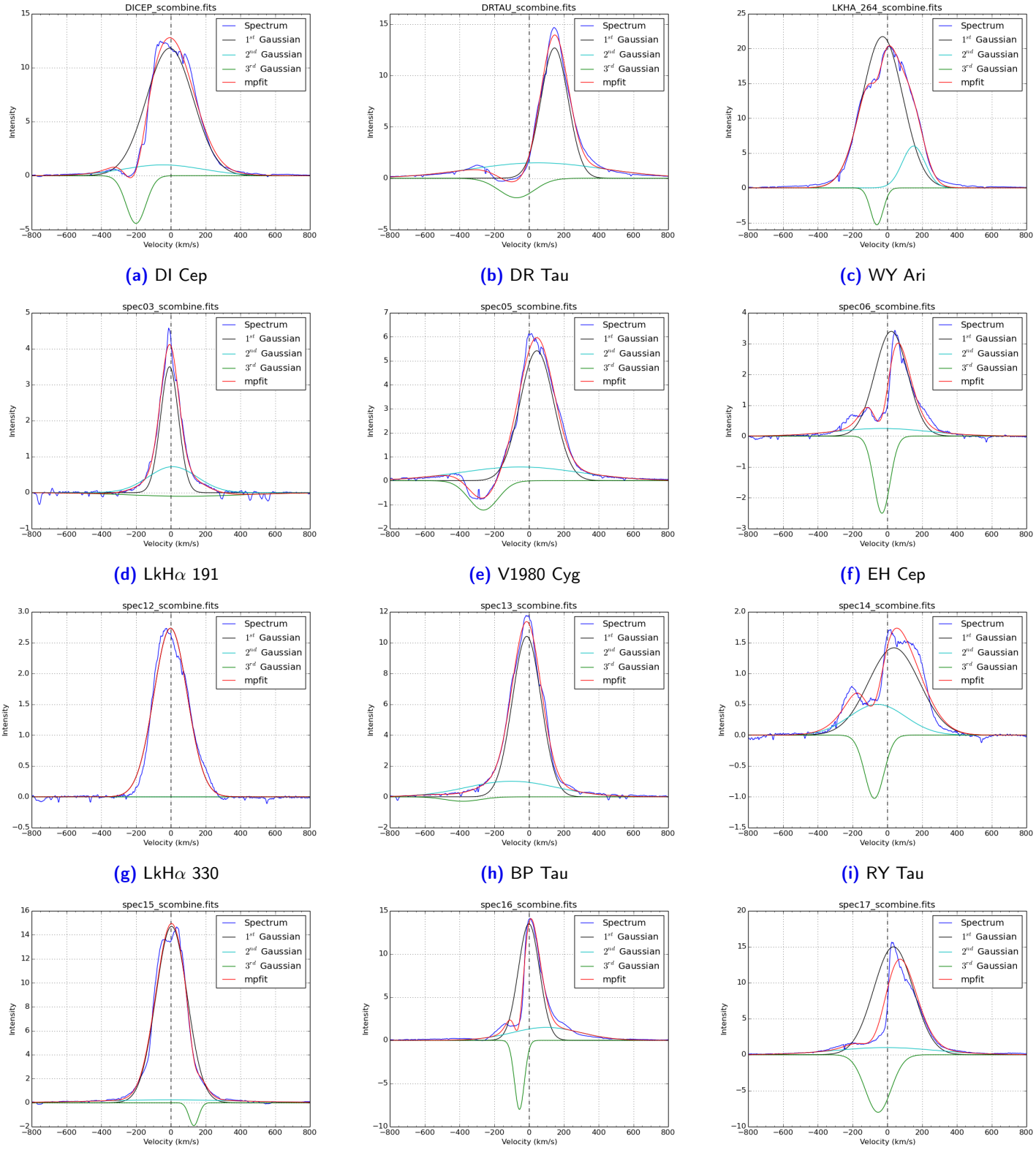

(a) DI Cep **(b)** DR Tau **(c)** WY Ari

(d) LkHα 191 **(e)** V1980 Cyg **(f)** EH Cep

(g) LkHα 330 **(h)** BP Tau **(i)** RY Tau

(j) T Tau **(k)** DF Tau **(l)** DG Tau

Figure A.1: Triple gaussian fitting for Hα emission line. In each plot are represented the reduced spectra (blue line), fit made with `mpfit` routine (red line), for Hα at 6563 Å, from three gaussians: the first is ajusted according with the peak intensity of the line (black line), the second adjusts the wings of the line (cyan line) and the third one fits the absorption present in the line. All the plots were corrected from the radial velocity.

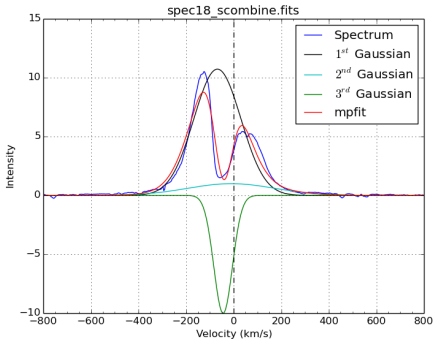

(m) DK Tau

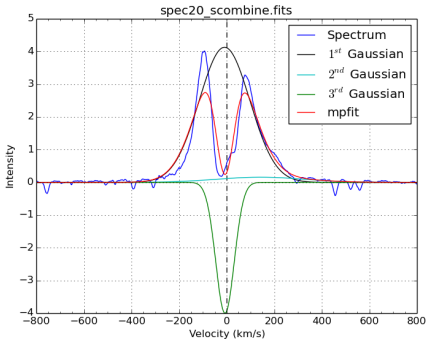

(n) AA Tau

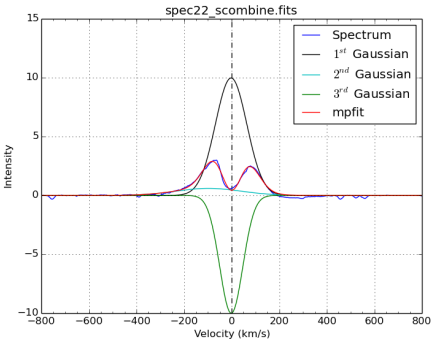

(o) V1079 Tau

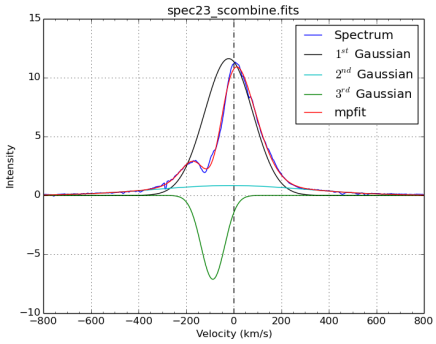

(p) DS Tau

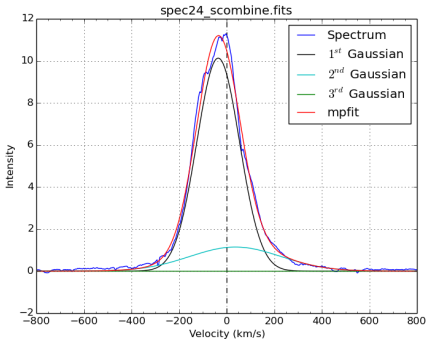

(q) UY Aur

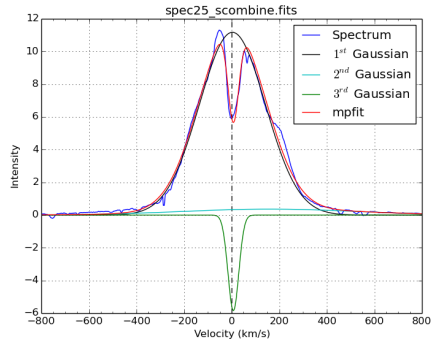

(r) GM Aur

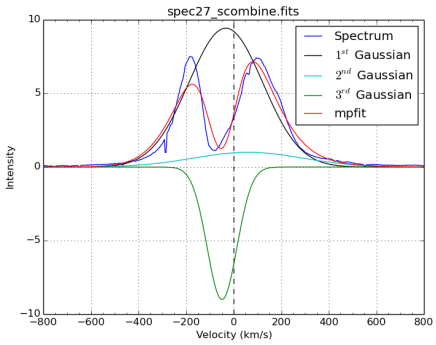

(s) RW Aur

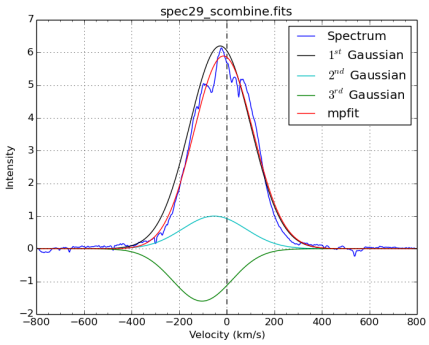

(t) V1305 Ori

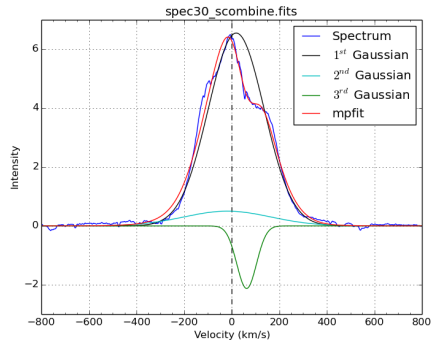

(u) V649 Ori

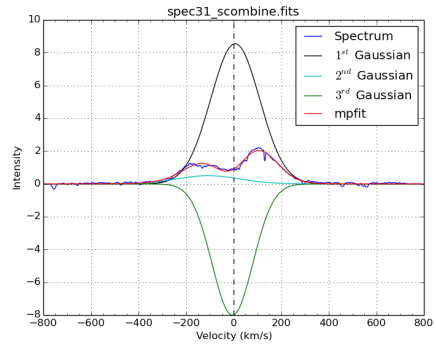

(v) AA Ori

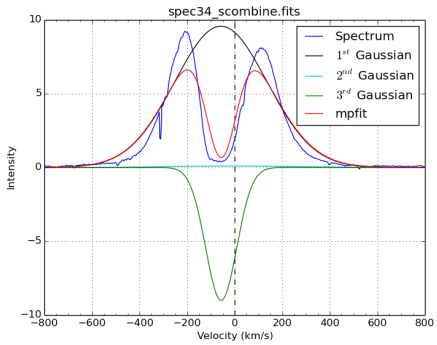

(w) BZ Sgr

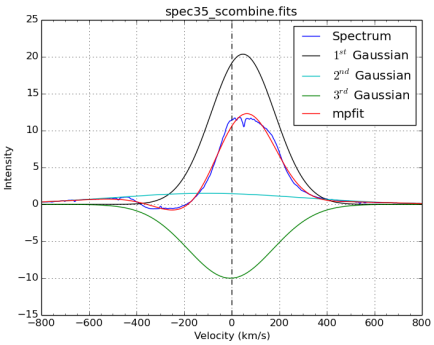

(x) AS 353A

Figure A.1: (continued)

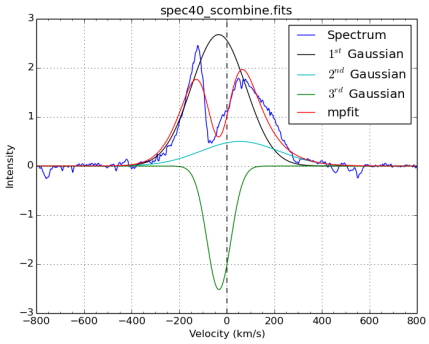

(y) V828 Cas

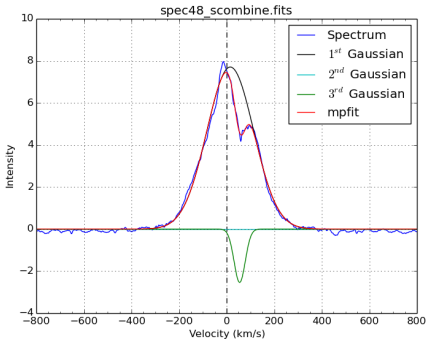

(z) UZ Tau E

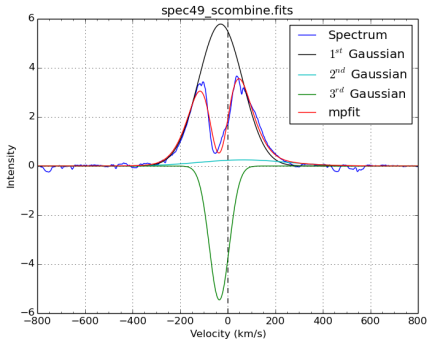

(aa) GK Tau

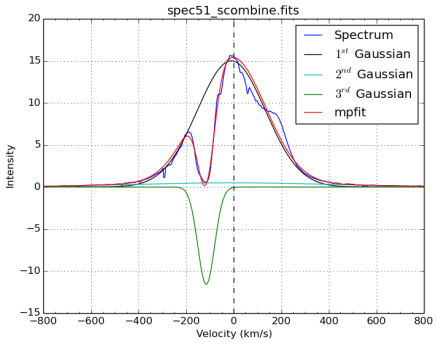

(ab) DL Tau

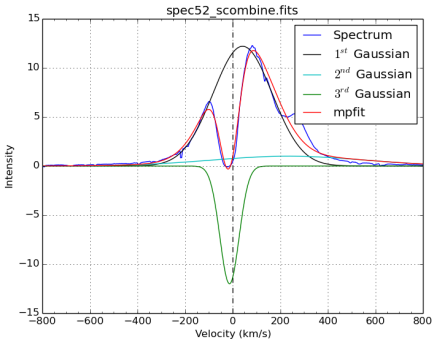

(ac) CI Tau

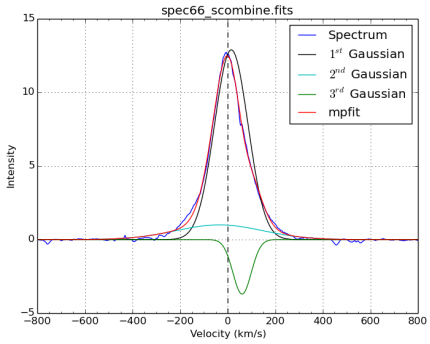

(ad) DQ Tau

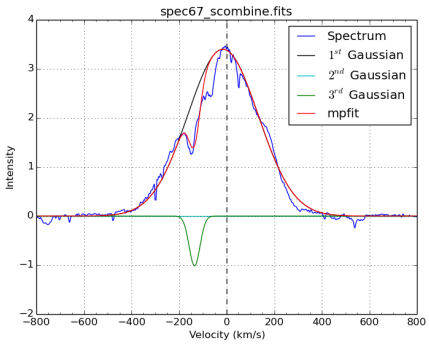

(ae) V466 Ori

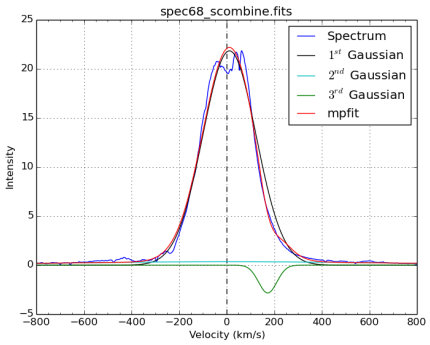

(af) DL Ori

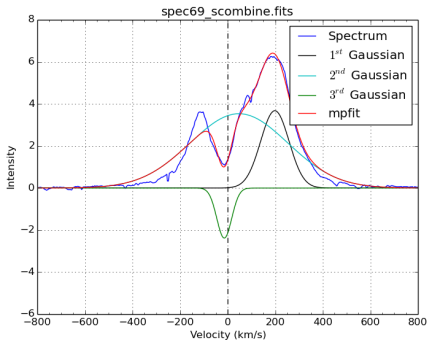

(ag) V625 Ori

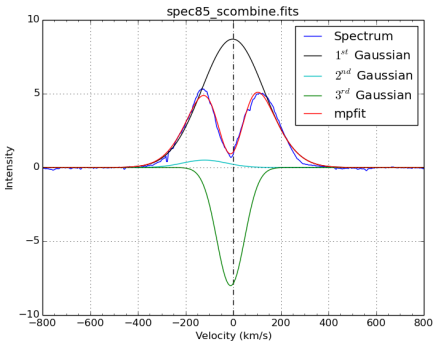

(ah) BM And

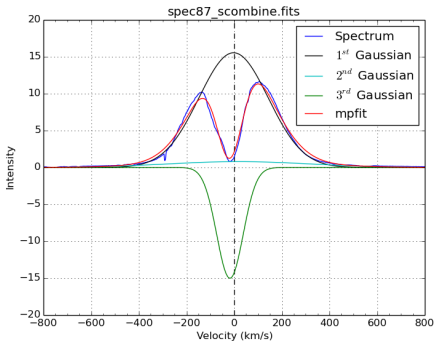

(ai) CW Tau

Figure A.1: (continued)

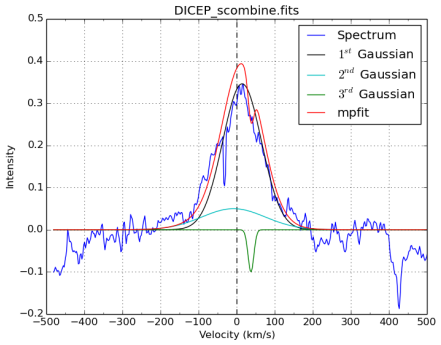

(a) DI Cep

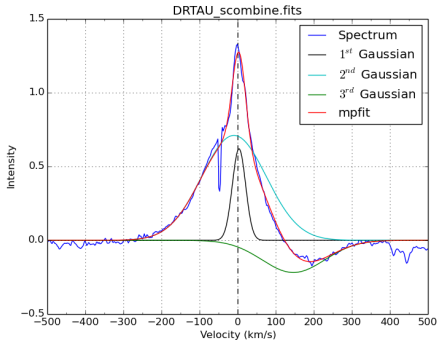

(b) DR Tau

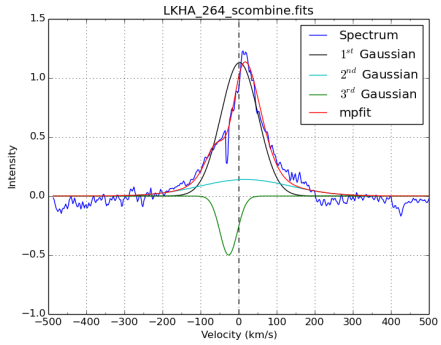

(c) WY Ari

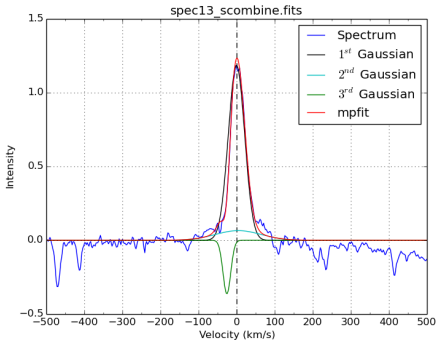

(d) BP Tau

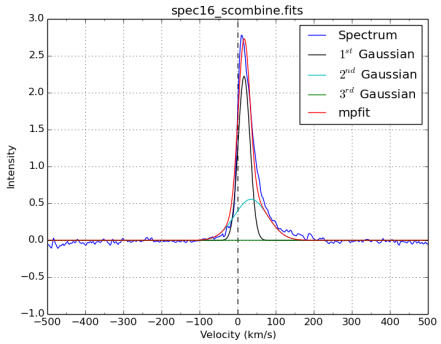

(e) DF Tau

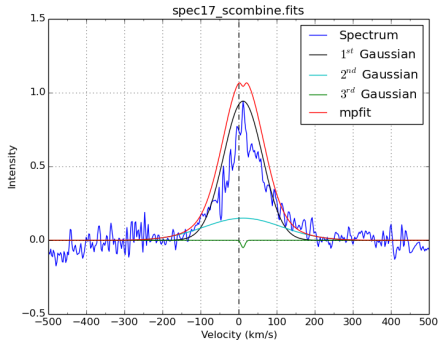

(f) DG Tau

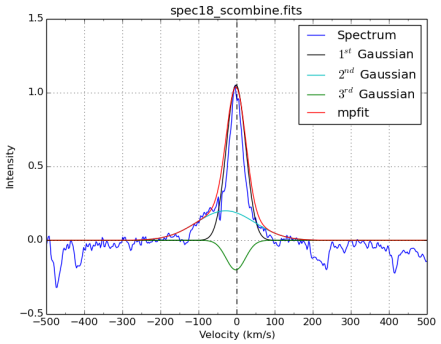

(g) DK Tau

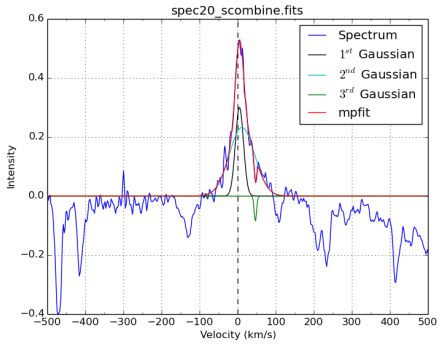

(h) AA Tau

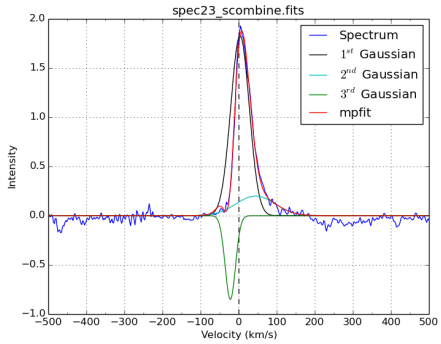

(i) DS Tau

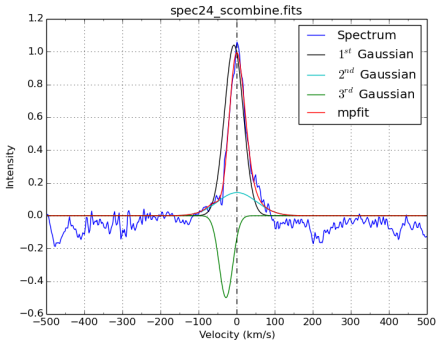

(j) UY Aur

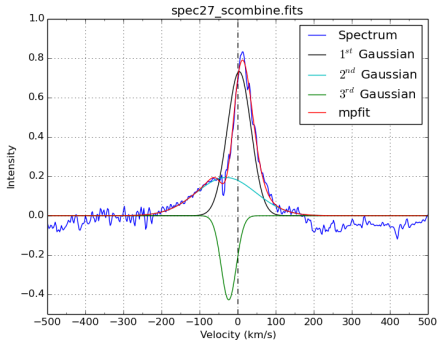

(k) RW Aur

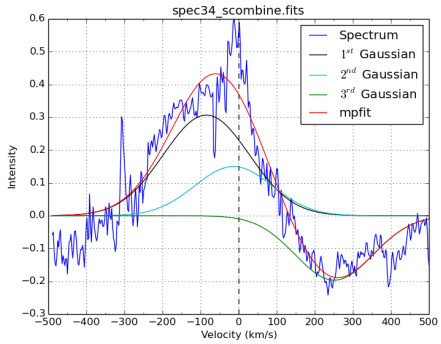

(l) BZ Sgr

Figure A.2: Triple gaussian fitting for He I $\lambda 5876$ emission line. In each plot are represented the reduced spectra (blue line), fit made with `mpfit` routine (red line), for He I at 5876Å, from three gaussians: the first is ajusted according with the peak intensity of the line (black line), the second adjusts the wings of the line (cyan line) and the third one fits the absorption present in the line. All the plots were corrected from the radial velocity.

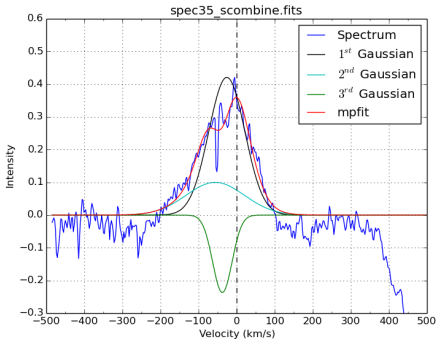

(m) AS 353A

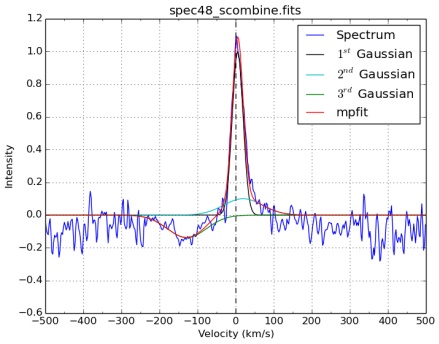

(n) UZ Tau E

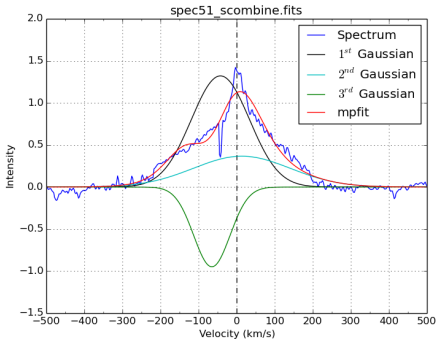

(o) DL Tau

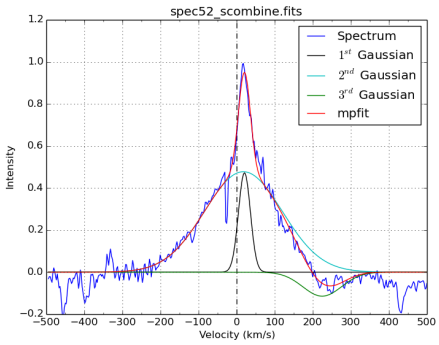

(p) CI Tau

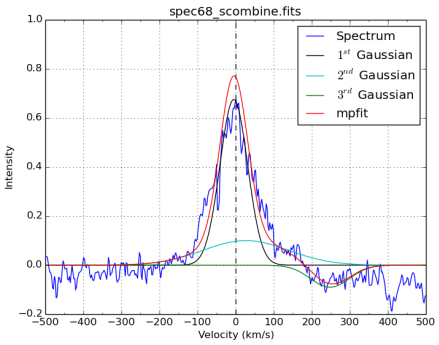

(q) DL Ori

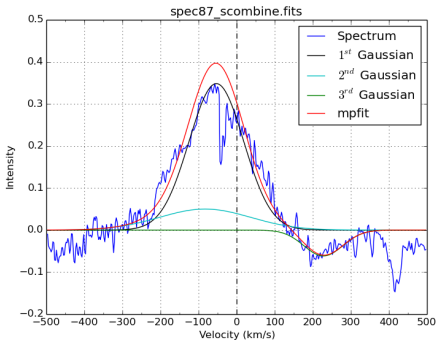

(r) CW Tau

Figure A.2: (continued)

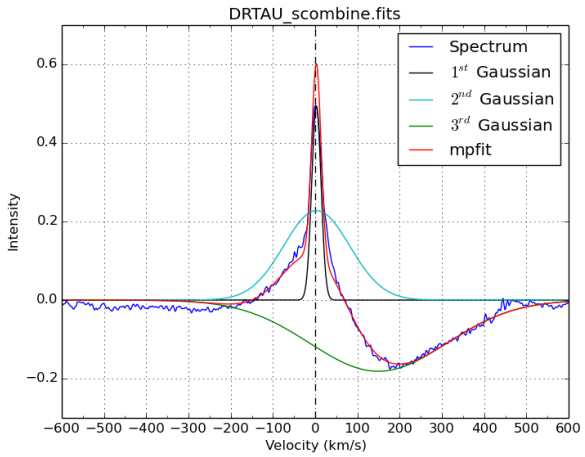

(a) DR Tau

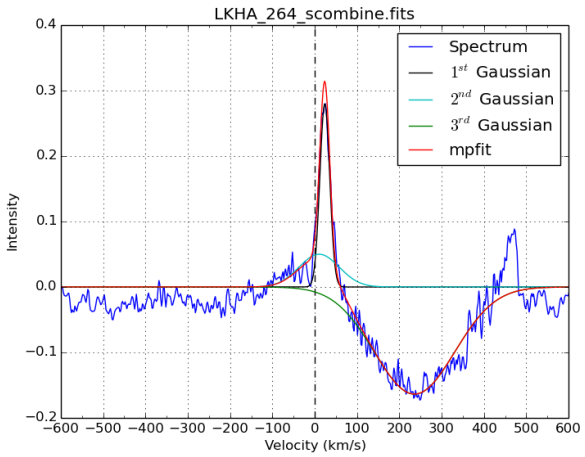

(b) WY Ari

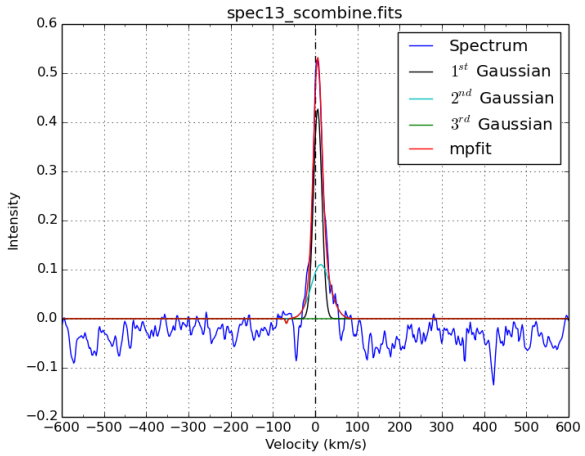

(c) BP Tau

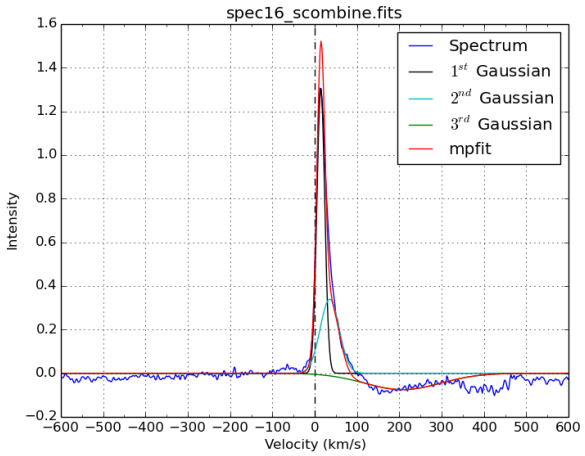

(d) DF Tau

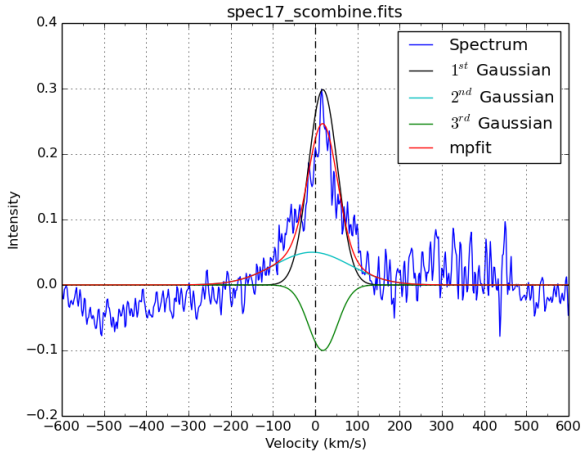

(e) DG Tau

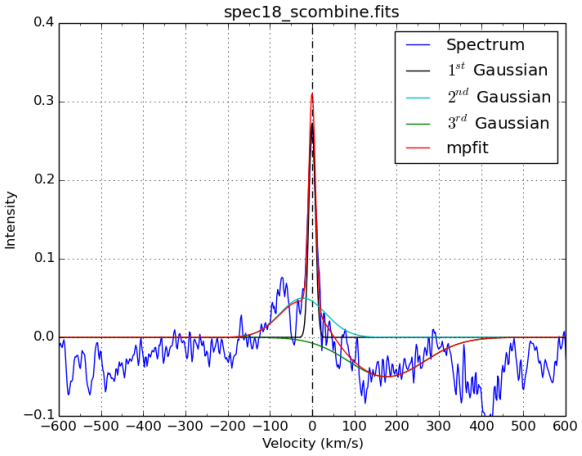

(f) DK Tau

Figure A.3: Triple gaussian fitting for He I $\lambda 6678$ emission line. In each plot are represented the reduced spectra (blue line), fit made with `mpfit` routine (red line), for He I at 6678Å, from three gaussians: the first is ajusted according with the peak intensity of the line (black line), the second adjusts the wings of the line (cyan line) and the third one fits the absorption present in the line. All the plots were corrected from the radial velocity.

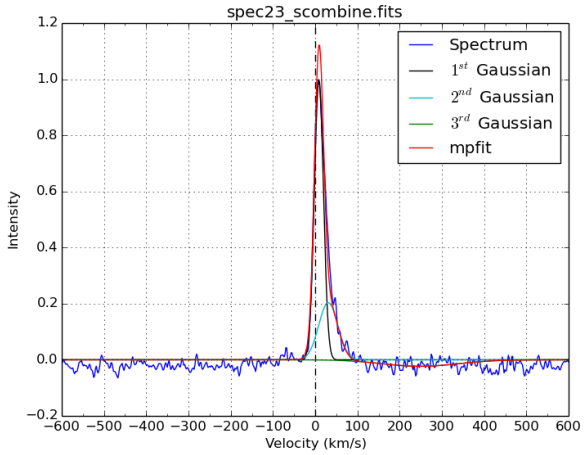

(g) DS Tau

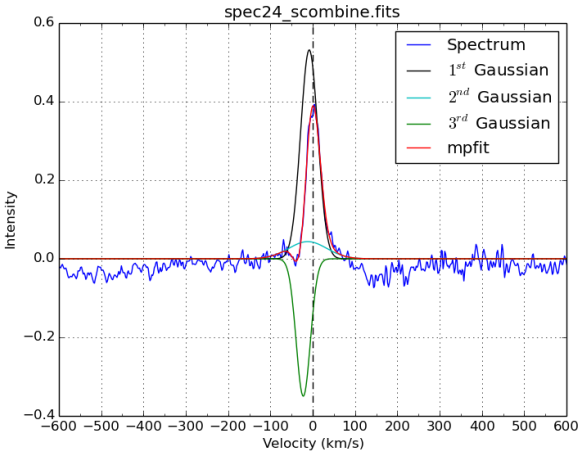

(h) UY Aur

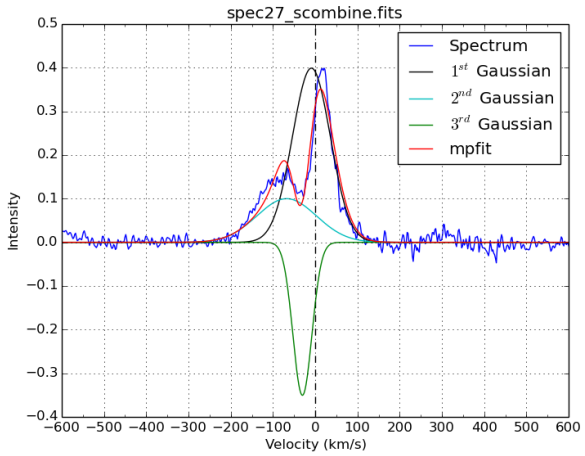

(i) RW Aur

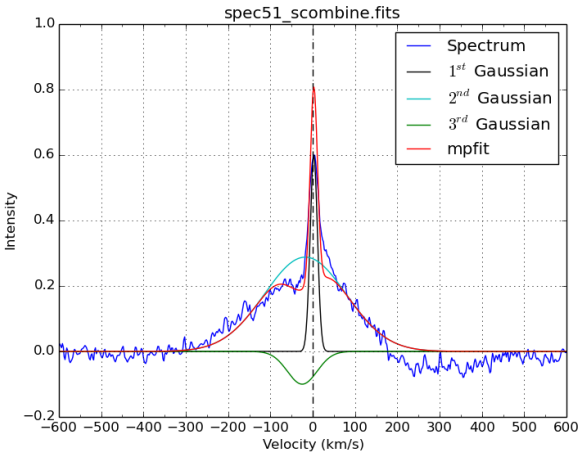

(j) DL Tau

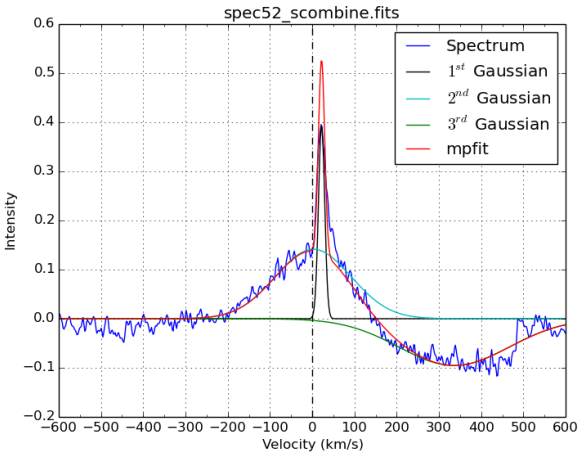

(k) CI Tau

Figure A.3: (continued)

Appendix B

Short guide for PLUTO code simulations

Due to the multiple steps needed to run each simulation, I found the need to write a short guide so I would not forget any step to compile and run PLUTO code simulations on Supernova server. This is the guide that I wished to have access when I began to work with PLUTO and CAUP server. I hope it will be useful for many students, investigators and whoever wants to learn how to begin with the same MHD simulations as I did.

1. Make the necessary alterations in the following files:
   - init.c - Rbeg, VX1, VX2 (inversion of the poloidal velocity);
   - pluto.ini - if necessary, change resolution in the 3^{rd} row, 4^{th} column.
2. Compress folder with the command line:
   `$ tar -cvf zipfolder.tar foldername/`
3. Send folder with changed files to Supernova server with:
   ```
   $ ls
   $ sftp user@Supernova
   $ put zipfolder.tar
   $ quit
   ```
4. Getting in Supernova, moving and uncompressing folder:
   ```
   $ ssh -Y user@Supernova
   $ mv zipfolder.tar /home/user/...
   $ tar -xvf zipfolder.tar
   ```
5. In the simulation folder in Supernova server, make sure there are `makefile` and `pluto` executable files. Otherwise make a copy of them from PLUTO folder with the command line:
   `$ cp makefile pluto /home/user/...`

6. In the simulation directory compile and run the simulation with the commands:

   ```
   $ make
   $ nohup ./pluto &
   ```

7. To see for how long the simulation is running type:

   ```
   $ ps -auxr
   ```

8. To check the evolution of the simulation, read `pluto.log` file:

   ```
   $ m pluto.log
   ```

9. To interrupt the simulation:

   ```
   $ ps aux | grep ‘‘pluto’’
   > Number ID (...)  ./pluto
   $ kill -9 ID
   ```

10. To remove folders:

    ```
    $ rm -rf foldername/
    ```

11. To get folders from Supernova server use:

    ```
    $ sftp user@Supernova
    $ get user/.../folder/
    $ quit
    ```